

AN ABSTRACT OF THE THESIS OF

_____ Corey Thompson Miller _____ for the _____ Master of Science _____
Degree in _____ Physical Sciences _____ presented on _____ November 12, 2019 _____

Title: Fault Trace Analysis Using Dipole-Dipole Resistivity and Downhole Geophysics in an LNAPL Contaminated Fractured Aquifer

Abstract approved: _____

A series of significant hydrocarbon releases occurred at a former Ingersoll Rand facility in Phillipsburg, New Jersey between the 1940's and 1960's causing an extensive light non-aqueous phase liquid (LNAPL) contamination presence in an aquifer which supplies water for human use. LNAPL migration is difficult to monitor, as its non-aqueous behavior causes migration to occur in the direction of groundwater flow or along less-confining features such as fractures or faults. Non-invasive geophysical techniques hold promise for LNAPL characterization at fractured bedrock sites such as this one, given their ability to provide information on a variety of physical earth properties. The primary objective of this research is to test the hypothesis that a thrust fault has influenced LNAPL migration at the site. Geophysical field models were generated from dipole-dipole Electrical Resistivity Imaging (ERI) data which displayed a roughly linear, significantly low-resistivity zone that has been interpreted as a shallow, near vertical expression of a thrust fault which had an apparent influence on LNAPL migration. To complement the ERI survey, optical televiewer, caliper, formation resistivity, temperature, gamma, fluid resistivity, and heat pulse flow meter data were collected in two bedrock wells which

provided insight as to the general strike and dip of fractures and bedding features, minor variations in lithology, and vertical flow conditions as they relate to LNAPL migration. This research also tests the hypothesis that direct detection of LNAPL contamination through the use of ERI measurements is not likely based on predictive forward models constructed prior to the field study. A forward model was generated in the lab using predetermined parameters of known and anticipated geologic conditions. Both the forward model prediction and actual field models revealed that direct detection was not possible as a function of loss of resolution of ERI measurements with increasing depth and the lack of contrast between the measured ERI responses of the LNAPL plume and surrounding geologic material. The geophysical techniques applied in this research show a promising outcome for use at other sites because structural features contributing to contaminant transport were readily identified in the modeled ERI data sets, and the forward model and field models both suggest the direct detection of LNAPL contamination would not be possible under similar conditions.

FAULT TRACE ANALYSIS USING DIPOLE-DIPOLE RESISTIVITY
AND DOWNHOLE GEOPHYSICS IN AN
LNAPL CONTAMINATED FRACTURED AQUIFER

A Thesis
Presented to
The Department of Physical Sciences
EMPORIA STATE UNIVERSITY

In Partial Fulfillment
of the Requirements for the Degree
Master of Science

By
Corey Thompson Miller
October 2019

Thesis approved by:

Dr. Marcia Schulmeister, Committee Chair

Dr. Alivia Allison, Committee Member

Dr. Christopher Pettit, Committee Member

Dr. Richard Sleezer, Department Chair

Dr. Jerald Spotswood, Dean of the Graduate
School and Distance Education

ACKNOWLEDGEMENTS

This thesis has become a reality through the kindness and support of many; I would like to thank them all.

I would first like to thank my thesis chair Dr. Marcia Schulmeister for her constant support, patience, and words of wisdom throughout this process. I would specifically like to thank you for allowing this work to be my own, while at the same time providing much needed guidance, feedback, and technical knowledge when I needed it the most. I would like to extend my most sincere gratitude for affording me the opportunity to pursue the challenging and rewarding task of earning an advanced degree – it would not have been possible without your support and encouragement.

I would next like to extend special gratitude to my committee members Dr. Alivia Allison and Dr. Christopher Pettit for their willingness to vet this research. Thank you for guidance, insight, and for accepting the role as both committee members and mentors. Throughout the process of completing a thesis, I have come to learn how much is expected of a Professor; I would like to thank you both for your commitment to your students, for the numerous roles you are required to fill, and for your dedication to academia.

I would like to next thank my wife, Jesse, who has been by my side for 13 years. Thank you for keeping me focused on my goals and encouraging me to reach them. Thank you for your never-ending support, love, and genuine kindness throughout my effort to earn this degree – I sure know it hasn't been easy! Thank you to my family: Dr. Dad, Mamadukes, Amy, Lowie, Leila, Rian, Rhys-man, Jenna, Paul, and Penny. Thank you to Joel and Jody of SET, Mike Welsh of Welsh Environmental, and Geosyntec for site access and permission to carry out this research. Growing up the idea of pursuing a college degree in any form was not something I thought was in the cards for me – I just struggled too much and too often. Now I have learned from that struggle and know the push it takes to earn not one, but two; thank you all for everything. Go Hornets!

TABLE OF CONTENTS

ACKNOWLEDGEMENTS	i
TABLE OF CONTENTS.....	ii-iii
LIST OF TABLES	iii
LIST OF FIGURES	iv-v
CHAPTER 1 Introduction.....	1
1.0 Research Hypotheses and Objectives	3
CHAPTER 2 The Study Area	5
2.0 Geographic Setting.....	5
2.1 Overburden	8
2.2 Bedrock Geology	9
2.3 Hydrogeology	12
2.4 Site Contamination and Previous Monitoring Activities	14
2.5 Previous Surface Geophysical Investigations at the Site	16
2.6 Previous Downhole Investigations at the Site	16
CHAPTER 3 Background: Geophysical Methods and Their Applications.....	19
3.0 Electrical Resistivity Imaging Method	19
3.1 Resistivity of Common Geologic Materials	20
3.2 A Brief Comparison of Commonly Used Electrode Geometry in ERI Surveys.....	21
3.3 Applications of the Electrical Resistivity Method	23
3.4 Borehole Geophysical Methods.....	25
3.5 Borehole Geophysical Instruments	26
3.5.1 Optical Televiewer.....	26
3.5.2 Three-arm Caliper Probe.....	29
3.5.3 Multi-parameter Resistivity Tool.....	32
3.5.4 Heat Pulse Flow Meter.....	33
3.6 Applications of Borehole Geophysical Methods	34
CHAPTER 4 Methods: Survey Design, Data Quality, and Data Processing	36
4.0 Electrical Resistivity Imaging Survey Design	36
4.1 Procedures Prior to Field Setup	39
4.2 Electrical Resistivity Imaging Survey Procedures.....	40
4.3 Contact Resistance Test (CRT).....	40
4.4 Electrical Resistivity Imaging Data Processing.....	45

4.5 A Qualitative Explanation of Geophysical Inversion	45
4.6 Data Quality Outputs and Poorly Fit Data Removal	46
4.7 Borehole Geophysical Survey Design	72
4.8 Borehole Geophysical Survey Setup	72
4.9 Borehole Geophysical Data Processing Considerations	74
CHAPTER 5 Anticipated Results	79
5.0 Forward Modeling of Electrical Resistivity Imaging Data.....	79
5.1 Anticipated Structural Responses Based on Previous OPTV Data	87
CHAPTER 6 Results.....	88
6.0 General Comparison of Forward Models to Modeled Resistivity Sections	88
6.1 Electrical Resistivity Survey Results	90
6.2 Borehole Geophysical Survey.....	103
6.3 A General Comparison of Newly Obtained OPTV Data to Previous Logs.....	103
6.4 Borehole Geophysical Survey Results for MW-17	104
6.5 Borehole Geophysical Survey Results for MW-19	126
CHAPTER 7 Discussion.....	146
7.0 General Discussion of ERI Interpretations	146
7.1 Borehole Geophysical Data Interpretations	150
CHAPTER 8 Conclusions.....	152
8.0 Summary of Work.....	152
8.1 Future Work	154
REFERENCES	156-159

LIST OF TABLES

Table 1	Resistivity of Common Earth Materials	21
Table 2	Tectonic, Sedimentary, and Diagenetic Features.....	27
Table 3	MW-17 Bedrock Structures	121-125
Table 4	MW-19 Bedrock Structures	143-145

LIST OF FIGURES

Figure 2.0	Physiographic Provinces Map.....	6
Figure 2.1	Site Proximity to Urban Phillipsburg and Study Area	7

Figure 2.2	Study Area and Local Bedrock Units.....	10
Figure 2.3	Stratigraphic Column of Eastern PA and NJ.....	11
Figure 2.4	Aquifer and Confining Units Map	13
Figure 2.5	LNAPL Plume, Monitoring Wells, and Thrust Fault.....	15
Figure 2.6	Rose Diagram Showing Dominate Strike of Bedding Planes	18
Figure 2.7	Rose Diagram Showing Dominate Strike of Borehole Fractures	18
Figure 3.0	The 2D Configurations of Dipole-Dipole Array	20
Figure 3.1	Electrode Array Configurations for Resistivity Measurements	22
Figure 3.2	Strike/Dip from OPTV Logs	28
Figure 3.3	Example Output of OPTV Data	28
Figure 3.4	Conceptual Drawing of Caliper Probe and Data Output.....	31
Figure 3.5	Caliper Data Output Adjacent to OPTV Log	32
Figure 4.0	ERI Line Placement, LNAPL Plume, Source, and USGS Fault	38
Figure 4.1	Command File Created in AGI Administrator	39
Figure 4.2	Line 1 – Contact Resistance Chart	42
Figure 4.2.1	Line 2 – Contact Resistance Chart	42
Figure 4.2.2	Line 3 – Contact Resistance Chart	43
Figure 4.2.3	Line 4 – Contact Resistance Chart	43
Figure 4.2.4	Line 5 – Contact Resistance Chart	44
Figure 4.2.5	Line 6 – Contact Resistance Chart	44
Figure 4.3	Line 1 – Cross Plot of Measured vs. Predicted Resistivity Data.....	48
Figure 4.3.1	Line 1 – Scatterplot of Repeat Measurement Errors (%)	49
Figure 4.3.2	Line 1 – Data Misfit Histogram for Removal of Poorly Fit Data	50
Figure 4.3.3	Line 1 – Measured and Calculated Sections.	51
Figure 4.4	Line 2 – Cross Plot of Measured vs. Predicted Resistivity Data.....	52
Figure 4.4.1	Line 2 – Scatterplot of Repeat Measurement Errors (%)	53
Figure 4.4.2	Line 2 – Data Misfit Histogram for Removal of Poorly Fit Data	54
Figure 4.4.3	Line 2 – Measured and Calculated Sections	55
Figure 4.5	Line 3 – Cross Plot of Measured vs. Predicted Resistivity Data.....	56
Figure 4.5.1	Line 3 – Scatterplot of Repeat Measurement Errors (%).....	57
Figure 4.5.2	Line 3 – Data Misfit Histogram for Removal of Poorly Fit Data	58
Figure 4.5.3	Line 3 – Measured and Calculated Sections and	59
Figure 4.6	Line 4 – Cross Plot of Measured vs. Predicted Resistivity Data.....	60

Figure 4.6.1	Line 4 – Scatterplot of Repeat Measurement Errors (%)	61
Figure 4.6.2	Line 4– Data Misfit Histogram for Removal of Poorly Fit Data	62
Figure 4.6.3	Line 4 – Measured and Calculated Sections	63
Figure 4.7	Line 5 – Cross Plot of Measured vs. Predicted Resistivity Data.....	64
Figure 4.7.1	Line 5 – Scatterplot of Repeat Measurement Errors (%)	65
Figure 4.7.2	Line 5 – Data Misfit Histogram for Removal of Poorly Fit Data	66
Figure 4.7.3	Line 5 – Measured and Calculated Sections	67
Figure 4.8	Line 6 – Cross Plot of Measured vs. Predicted Resistivity Data.....	68
Figure 4.8.1	Line 6 – Scatterplot of Repeat Measurement Errors (%)	69
Figure 4.8.2	Line 6 – Data Misfit Histogram for Removal of Poorly Fit Data	70
Figure 4.8.3	Line 6 – Measured and Calculated Sections.....	71
Figure 4.9	Site Photo Showing OPTV Probe.....	73
Figure 4.9.1	Planar Fracture Sinusoidal Trace.....	75
Figure 4.9.2	Pick Time of Upward Flow Within MW-17	78
Figure 4.9.3	Pick Time of Upward Flow Within MW-19	78
Figure 5.0	Forward Model One.....	82
Figure 5.1	Forward Model Two	84
Figure 5.2	Forward Model Three	86
Figure 6.0	Line One Unannotated and Annotated Res Section.....	92
Figure 6.1	Line Two Unannotated and Annotated Res Section.....	94
Figure 6.2	Line Three Unannotated and Annotated Res Section	96
Figure 6.3	Line Four Unannotated and Annotated Res Section.....	98
Figure 6.4	Line Five Unannotated and Annotated Res Section	100
Figure 6.5	Line Six Unannotated and Annotated Res Section.....	102
Figure 6.6	MW-17 Well Log Results.....	110-120
Figure 6.7	MW-19 Well Log Results	133-142
Figure 7.0	Projection of Interpreted Thrust Faults Relative to LNAPL Plume	149

CHAPTER 1

INTRODUCTION

A series of major hydrocarbon releases occurred at a former Ingersoll Rand manufacturing facility in northwestern New Jersey between the 1940's and the 1960's, causing an extensive light non-aqueous phase liquid (LNAPL) contamination presence throughout an aquifer in which water is extracted for human use (U.S. EPA, 2018). LNAPL is a light non-aqueous phase liquid that exists as a separate, immiscible liquid phase when in contact with water and/or air (Acree et al., 1995). The lower density of LNAPLs causes migration to occur in the direction of groundwater flow gradient or along less confining features such as fractures or faults. Because of this, LNAPLs can spread out laterally over great distances, making it difficult to detect and to remediate, especially at fractured rock sites. LNAPL delineation has traditionally been conducted using conventional drilling methods that require the installation and sampling of groundwater wells. Although direct measurements of LNAPL contamination are still necessary for delineation, indirect evidence of LNAPL migration based on geophysical imaging holds potential as a less-expensive complement to conventional well-based sampling methods. This research examines two main scientific inquiries. One of which compares the links between a documented LNAPL plume and a thrust fault that exists below the source of contamination as a means for subsurface transport, and the other tests the ability of electrical resistivity imaging (ERI) measurements to directly detect LNAPL contamination where it is known to exist within the targeted aquifer.

The detection of organic contaminants through the use of surface geophysics has been evaluated by numerous researchers, yet few have produced repetitive results or consistently reliable methods for direct detection of LNAPLs (U.S. EPA, 1991). Although direct detection of LNAPLs is generally not possible with geophysical methods alone, determination of its migration by means of identifying and mapping subsurface preferential pathways such as faults, fractures, voids, or solution cavities that may impact fluid movement holds great promise. Because LNAPL migration within the subsurface is limited or enhanced by respective geologic conditions, identification of these contributing factors at contaminated sites are crucial from both environmental remediation and engineering perspectives.

Geophysical imaging can be conducted in both surface and downhole modes. Near-surface geophysical methods are generally used to investigate the upper few to hundreds of meters of the Earth's crust. They are also considered a non-invasive form of investigating subsurface conditions in the Earth through measuring, analyzing and interpreting physical fields from the ground surface. Downhole geophysics is the science of recording and analyzing measurements of physical properties made in wells or test holes. It is typically completed by means of lowering a probe into a well or test hole and measuring, recording, and analyzing physical properties of the surrounding formation.

1.0 Research Hypotheses and Objectives

The primary goal of this research is to test the hypothesis that a thrust fault has influenced LNAPL migration at the Ingersoll Rand Site. This research also tests the hypothesis that direct detection of LNAPL contamination through the use of ERI measurements alone is not likely, based on forward model predictions. To address these hypotheses, surface (dipole-dipole ERI) and downhole (optical televiewer (OPTV), formation resistivity (FRES), fluid resistivity (FLRES), resistance (R), temperature, three-arm caliper (CAL), and heat pulse flowmeter (HPFM)) geophysical methods were used to measure different physical properties within the Earth. The distribution of these measurements throughout the subsurface were then used to generate geophysical models and logs which, in turn, were used to interpret variations in subsurface geologic conditions. The interpreted variations in subsurface geologic conditions were then directly compared to known LNAPL plume extents. The following project objectives were completed to satisfy the hypotheses for this research:

- 1) Dipole-dipole resistivity profiles were compared to previously mapped thrust faults located within the site boundaries.

- 2) Optical televiewer, formation resistivity, fluid resistivity, temperature, three-arm caliper, and heat pulse flowmeter logs were obtained and examined for their ability to identify geologic features that may control preferential contaminant migration.

- 3) ERI values obtained above and below the water table were compared to known LNAPL distributions to determine the ability of ERI to detect LNAPL.
- 4) Determined which geophysical instrumentation provided the most useful data to meet the research objectives.

CHAPTER 2

THE STUDY AREA

The Ingersoll Rand Site is a former industrial facility located in northwestern New Jersey (Figure 2.0 and 2.1). It was constructed in 1903 and was built for the purpose of developing pumps, turbo-equipment, air and gas compressors, rock drills, and mining equipment. In addition, an iron and steel foundry was constructed to process raw materials for on-site manufacturing operations. The Ingersoll Rand Site has been extensively studied and is well-instrumented. Since the 1970's, extensive mapping of an LNAPL plume has been completed by installing a network of monitoring and extraction wells which were then sampled for LNAPL contamination by consulting scientists and engineers (U.S. EPA, 2018). Since 1973, facility operations declined and restructuring resulted in closing or moving of facility operations (U.S. EPA, 2018).

2.0 Geographic Setting

The research site is located in the Highlands physiographic province (NJDEP, 1996). The mountainous region of the Highlands Province is approximately 2,540 square kilometers (km) in area and has a rugged topography that consists of a series of discontinuous ridges and deep, narrow valleys (Dalton, 2003). The research area is located on a low, rolling ridge with a gentle, southeasterly slope; however, the topography in the study area is essentially flat. Little vegetation is present throughout the site, as most of which was removed prior to constructing the former industrial facility.

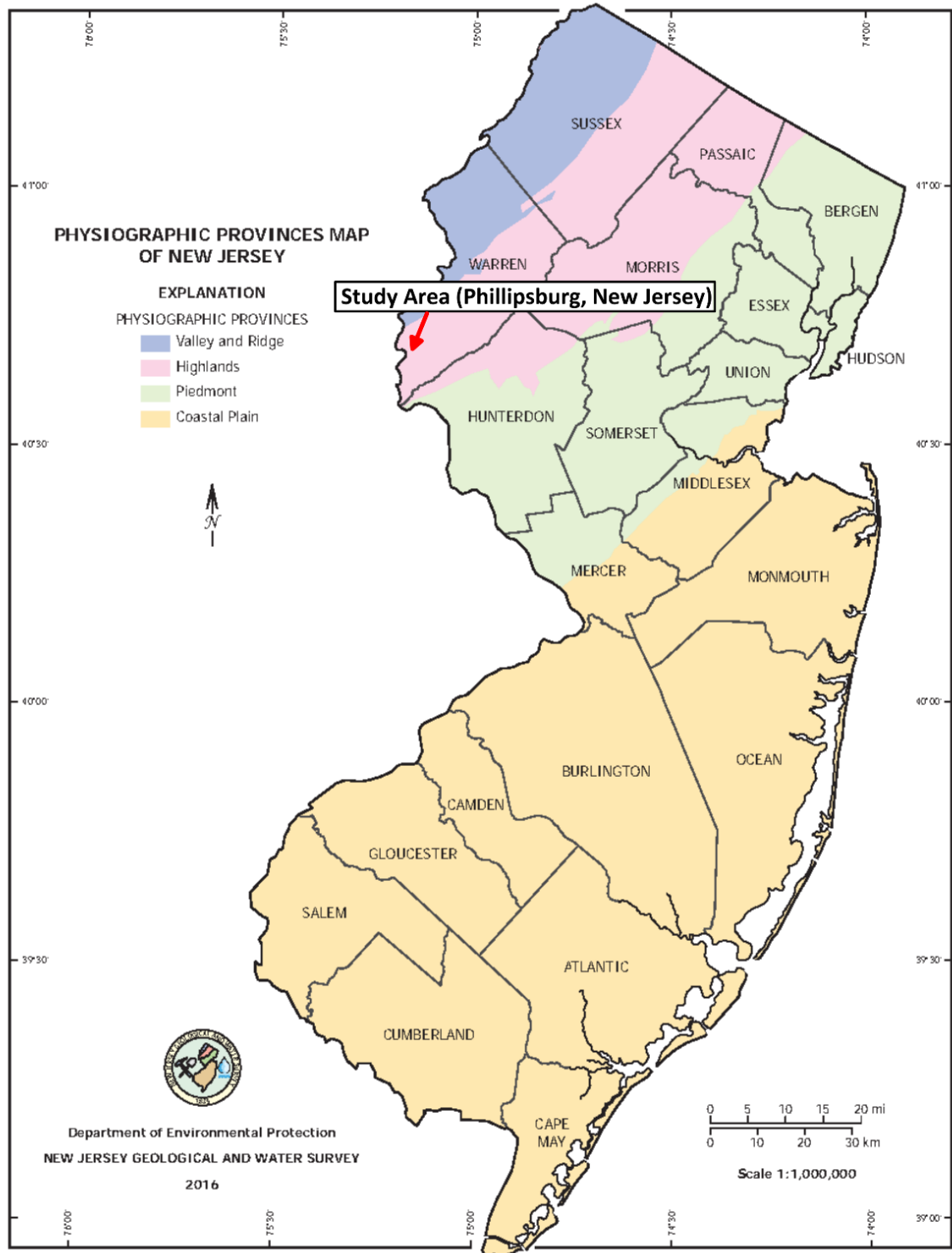


Figure 2.0 Physiographic provinces in New Jersey (modified after New Jersey Department of Environmental Protection, 2017).

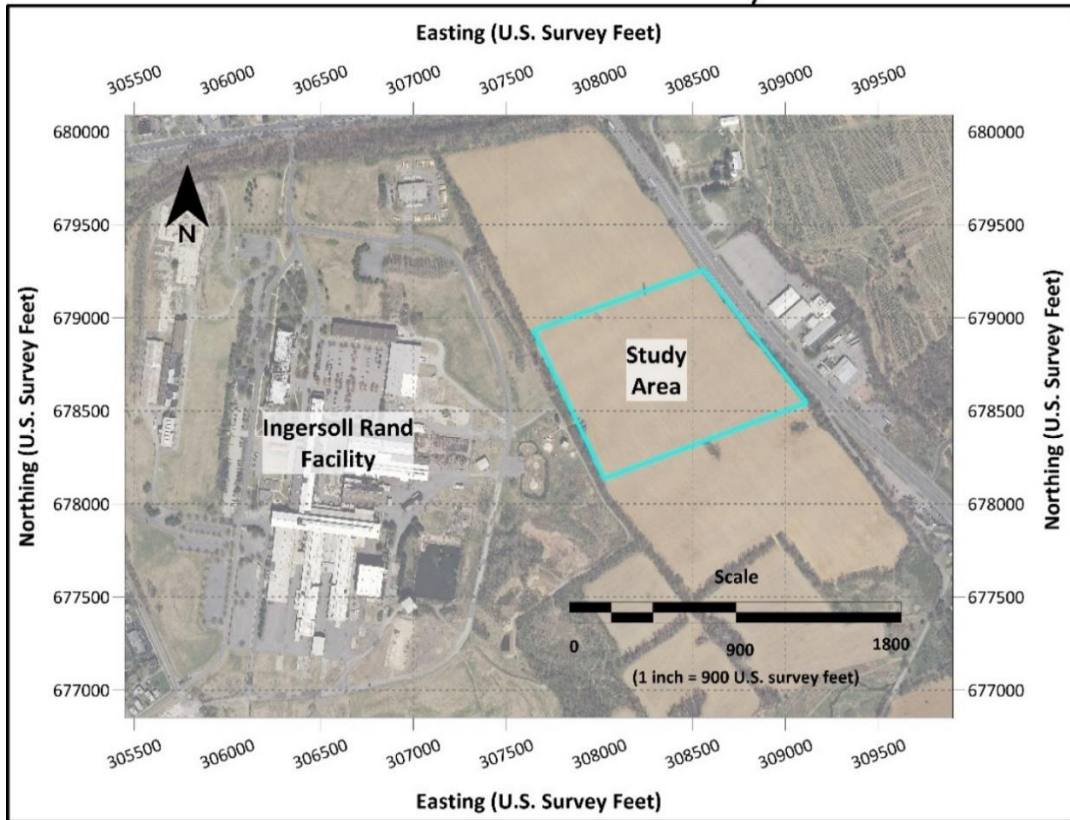
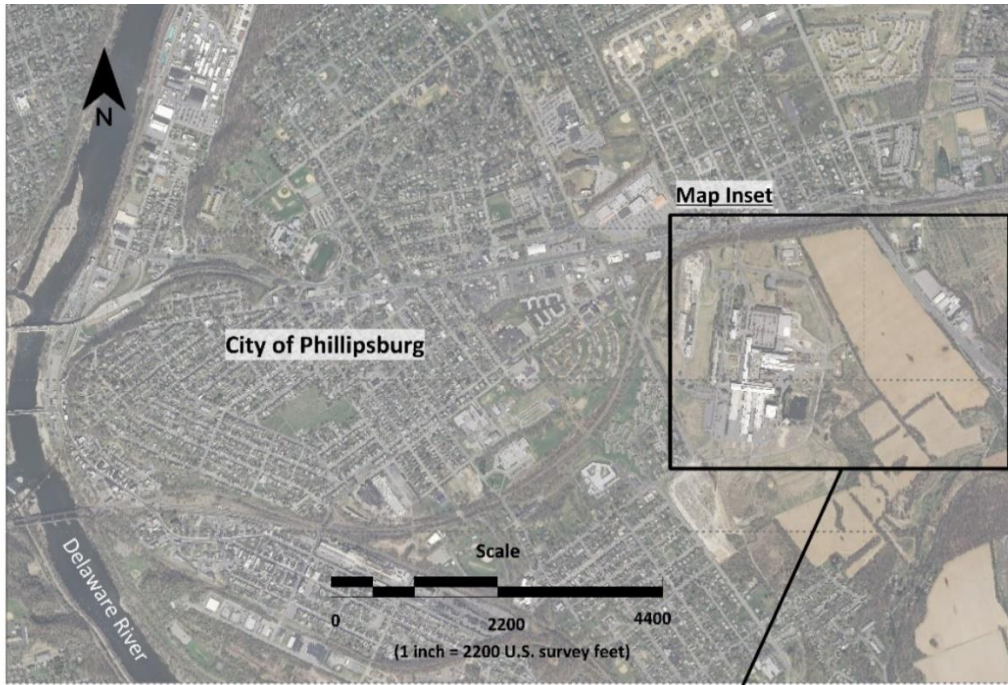


Figure 2.1 Site proximity to urban Phillipsburg and study area (modified after New Jersey Geographic Information Network, 2012).

2.1 Overburden

Overburden at the site primarily consists of clayey silty carbonate rock residuum as a direct result of in-situ chemical weathering of underlying carbonate rock (Stone et al., 2002). In the immediate area surrounding the main industrial complex, glacial till of the Port Murray Formation was documented and subsequently removed during construction of the facility (2002). Historic fill material is also pervasive throughout western half of the site and mainly consists of expended foundry sands (Geosyntec, 2015, p.37). The apparent fill thickness varies throughout the site from 0-meters (m) to 12-m below ground surface (Stone et al., 2002).

Overburden thickness varies greatly throughout the site, where it ranges from less than 0.5 m thick in some areas and up to 27 m in others (Stone et al., 2002). Overburden thickness is typically greatest at the southern portions of the site which has been identified as a former landfill associated with foundry activities. In addition to anthropogenic contributions to overburden thickness from foundry activities and construction, topographic variation has influenced it as well, where lower elevations tend to have greater thicknesses. A pervasive sandy clay layer overlies bedrock and ranges in thickness from approximately 1.5 m to approximately 12 m throughout the survey area, according to drillers logs for the site wells (ENSR, 2005, p. 58).

2.2 Bedrock Geology

Bedrock geology at the site consists of the Jacksonburg Limestone, the Kittatinny Supergroup, and the Hardyston Quartzite which range in age from Late Cambrian to the Early Ordovician; of those, the Kittatinny Supergroup is comprised of the Leithsville Formation, the Allentown Formation, and Beekmantown Group (Drake, 1967). The Late Cambrian Allentown Formation is pervasive throughout the southern portion of the study area and is comprised of very-fine to medium-grained, gray to dark gray dolomite. The bedrock surface dips from west to east and forms an unconformable contact with the overlying Rickenbach Formation of the Ordovician Beekmantown Group and Epler Groups.

The Beekmantown Group is present in the northern half of the study area and is a fine-to coarse-grained, light to dark gray dolomite with some breccia and apparent chert beds. The Epler Formation is present in the southeastern part of the site and is comprised of interbedded, very fine grained, light to medium gray limestone, and light to dark gray dolomite. Small-scale faulting is present throughout the site (most notably the southwest-to-northeast trending thrust fault within the study area), and regionally these formations have been complexly folded and faulted by past orogenic events. Specifically, the USGS has identified and mapped two suspected thrust faults with a rough orientation from southwest-to-northeast (Figure 2.2).

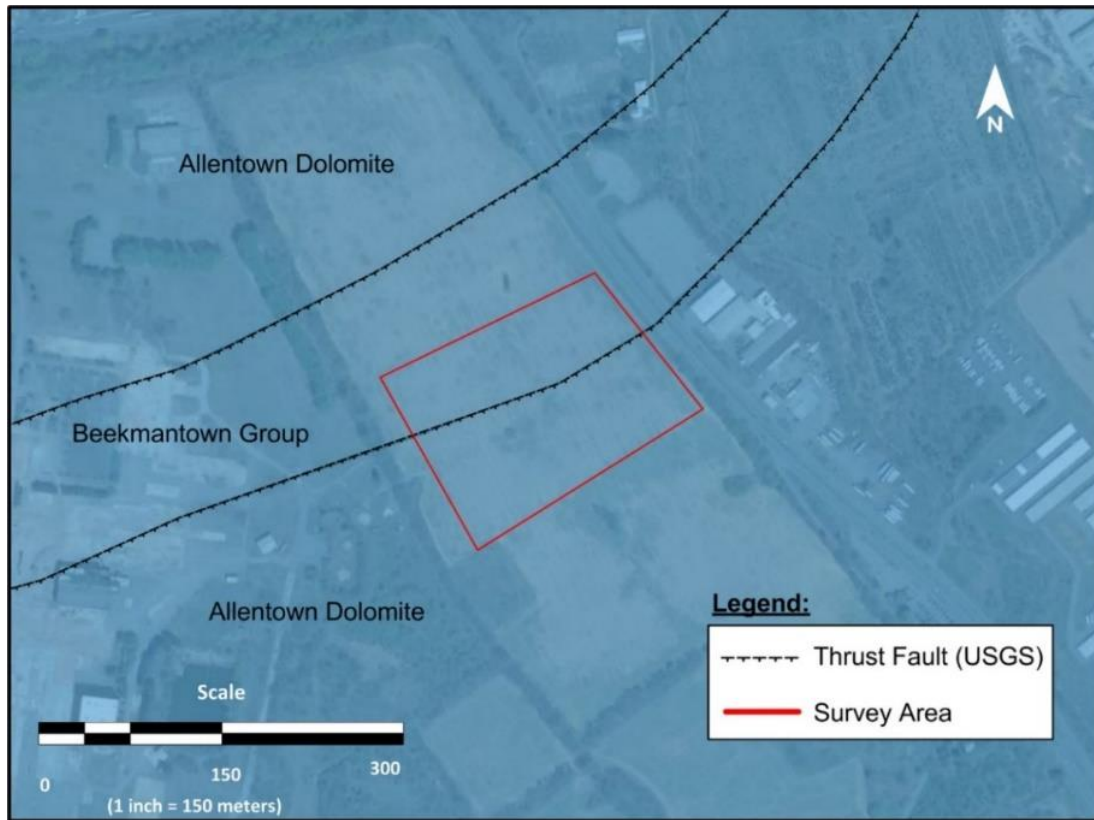


Figure 2.2 Study area and local bedrock units (modified after Google Maps, 2017; USGS, 2017).

In some areas surrounding the site, these formations are folded in a recumbent fashion. Drake (1967) measured dolomitic bedrock strikes in a northeasterly direction and dips to the southeast at approximately 25 degrees to 30 degrees. Formation thicknesses vary, as the Rickenbach is approximately 198 m and the Allentown Formation is approximately 579 m, where they are underlain by the Hardyston Quartzite. Bedrock at this site has characteristic features of an active karst aquifer, as sink holes have been known to develop, along with solution cavities and large open void spaces as observed in some of the provided drilling logs and data. A general stratigraphic column has been provided in figure 2.3.

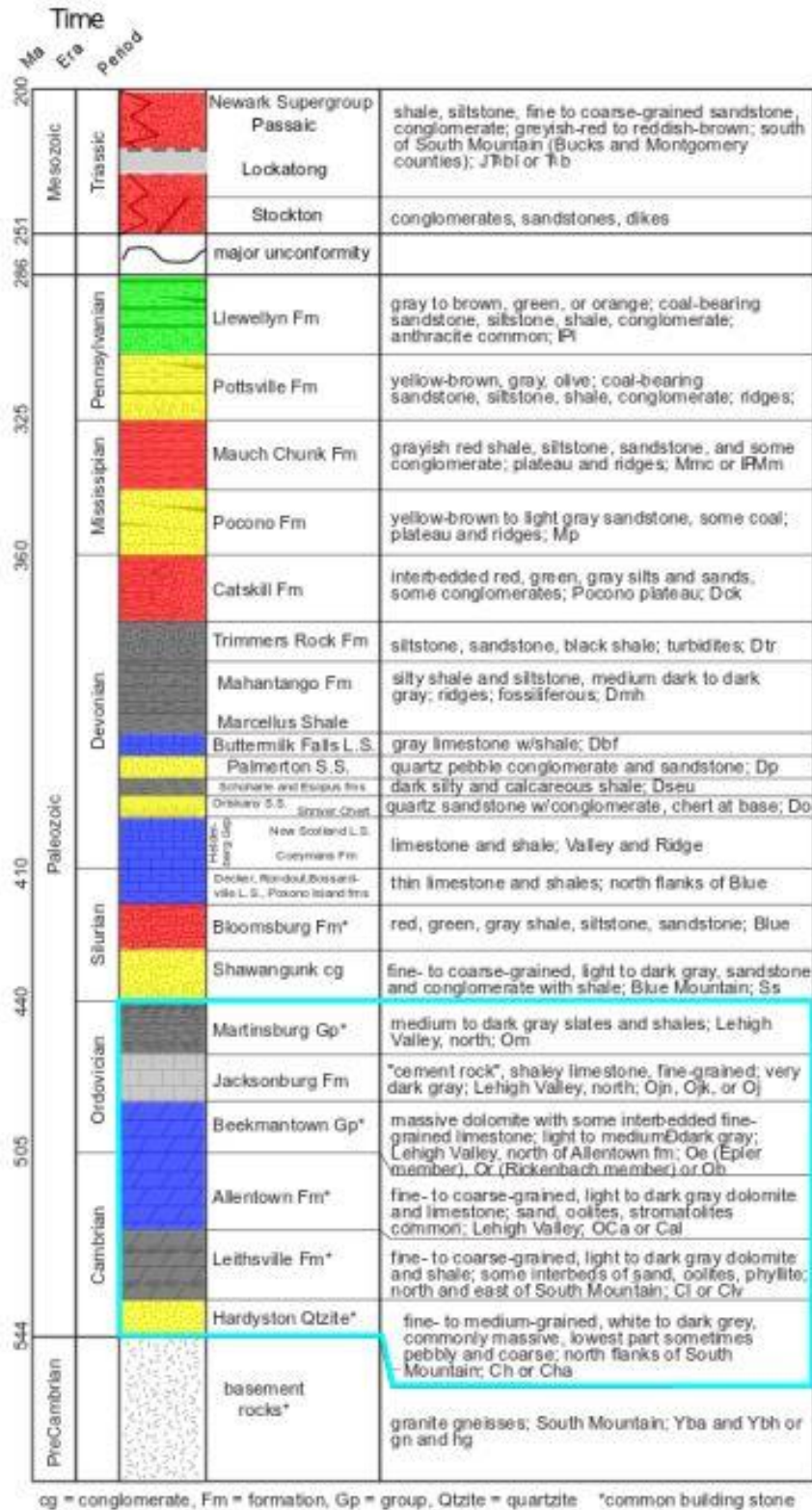


Figure 2.3 Stratigraphic column of eastern Pennsylvania and New Jersey (Modified after Lehigh University, 2012).

2.3 Hydrogeology

The primary aquifer of interest at this site (Figure 2.4 below) is the Jacksonburg and Kittatiny Limestone, and Hardyston Quartzite, or JKH (see cyan polygon on Figure 2.3). The JKH has been classified as a single aquifer system with well yields between 101-500 gallons per minute (gpm) (NJGS, 1998). Highly weathered and fractured rock contributes to high transmissivities, major fluctuations in groundwater levels (as much as 15 m), and large seasonal variation in potentiometric groundwater elevations (ENSR, 2004). Groundwater flow direction throughout this aquifer cannot be generalized and is primarily related to localized openings in bedrock such as faults, fractures, joints, or open beddings caused by tectonic events. Moreover, because this site is characterized as a karst geologic environment, bedrock is soluble, creating fractured rock networks which supports the development of solution cavities due to reactions of groundwater and bedrock compounds. Craig (1996) classifies groundwater flow as free or diffuse, where free flow is defined as rapid flow through well-integrated fracture systems, and diffuse flow displays laminate flow through rock fractures that have undergone minimal modification by solution. It is anticipated that these mechanisms of groundwater transport have influenced LNAPL plume migration at this site.

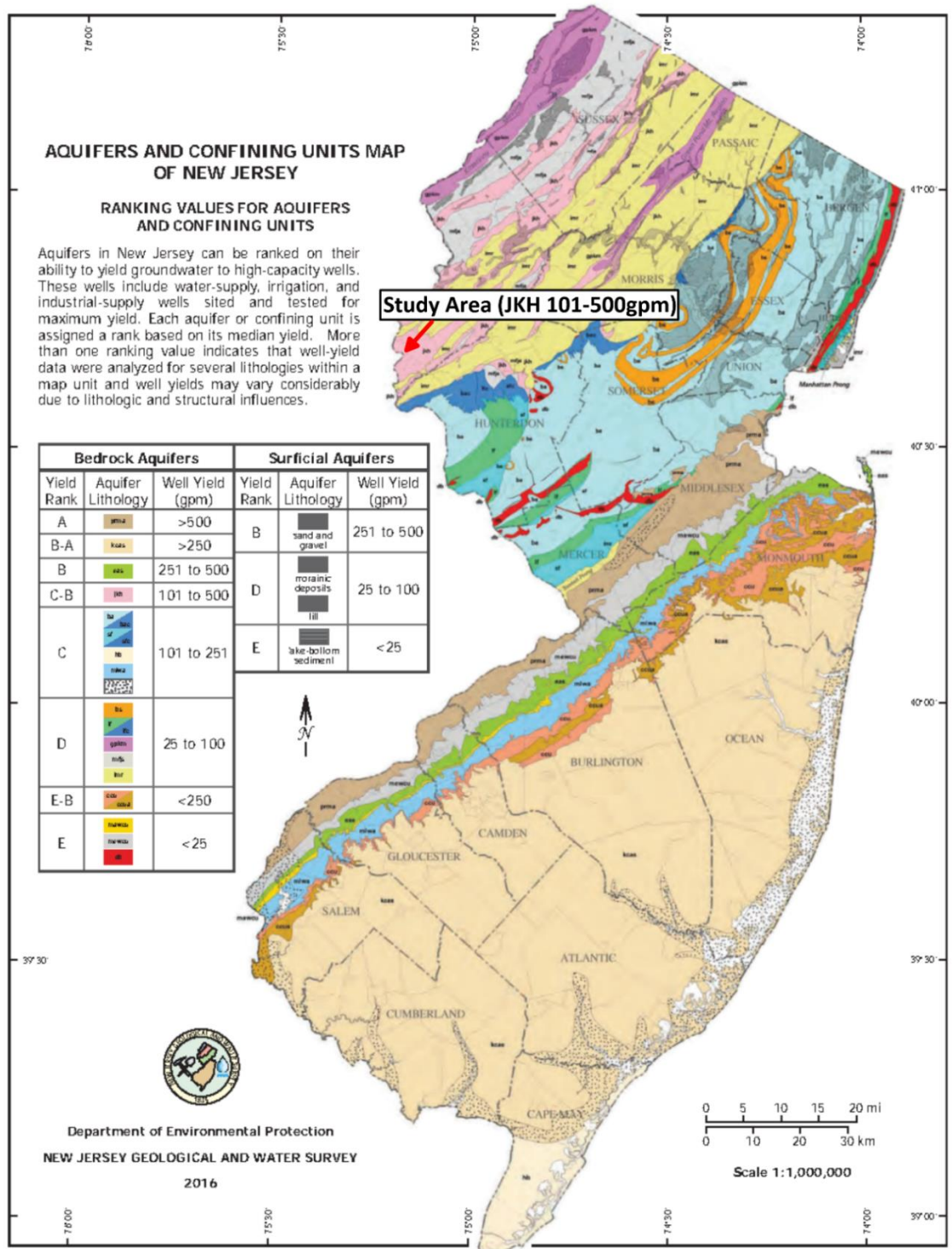


Figure 2.4 Aquifers and confining units in New Jersey (modified after NJDEP, 2017).

2.4 Site Contamination and Previous Monitoring Activities

The original hydrocarbon release in the early 1940's occurred due to a break in a buried transport pipeline associated with a holding tank, which was filled with No. 2 fuel oil, which is commonly used for heating buildings or in furnaces (INCHEM, 2004). Subsequently, ~20,000 gallons (gal) of No. 2 fuel oil was released into the surrounding subsurface (Geosyntec Consultants, Inc., 2015, p. 30). A second, much more significant release occurred in 1943, when a major discharge line from a second day tank was broken and an estimated 200,000 gal – 250,000 gal were released over the span of several days; additionally, a third major release occurred in the 1960's under similar circumstances as the prior two, resulting in a release of an additional 55,000 gal of No. 2 fuel oil (M. Welsh, Personal Communication, February 25, 2018). Number 2 fuel oil has a solubility limit of 0.0005 g/100 ml at 20 degrees C, making it relatively insoluble in water (INCHEM, 2004). These releases have had a major impact on local groundwater resources in the vicinity of the industrial complex, which is extracted for human use.

The discovery of LNAPL contamination occurred during the installation of a water supply well in 1974; subsequently, Ingersoll Rand installed a series of monitoring and recovery wells, then later added an LNAPL recovery remediation system in 1996 that was intended to remove the contaminant (ENSR, 2004). Between 2002 and 2004, a downhole geophysical investigation was completed to assess new and existing fracture orientation data. The goal of this investigation was to better understand aquifer characteristics and structural geologic conditions. A network of approximately 25 cm (or ten-inch) diameter

wells was installed across the site in both the Allentown and Beekmantown Formations, which range in depth from 40 to 45 m (ENSR, 2005, p. 58). The presence or absence of LNAPL contamination observed in these wells was used to delineate the margins of the LNAPL plume (Figure 2.5). The plume boundaries have not changed since 1986 (M. Welsh, Personal Communication, February 25, 2018). Two of the wells (MW-17 and MW-19) were used for geophysical measurements in this research.

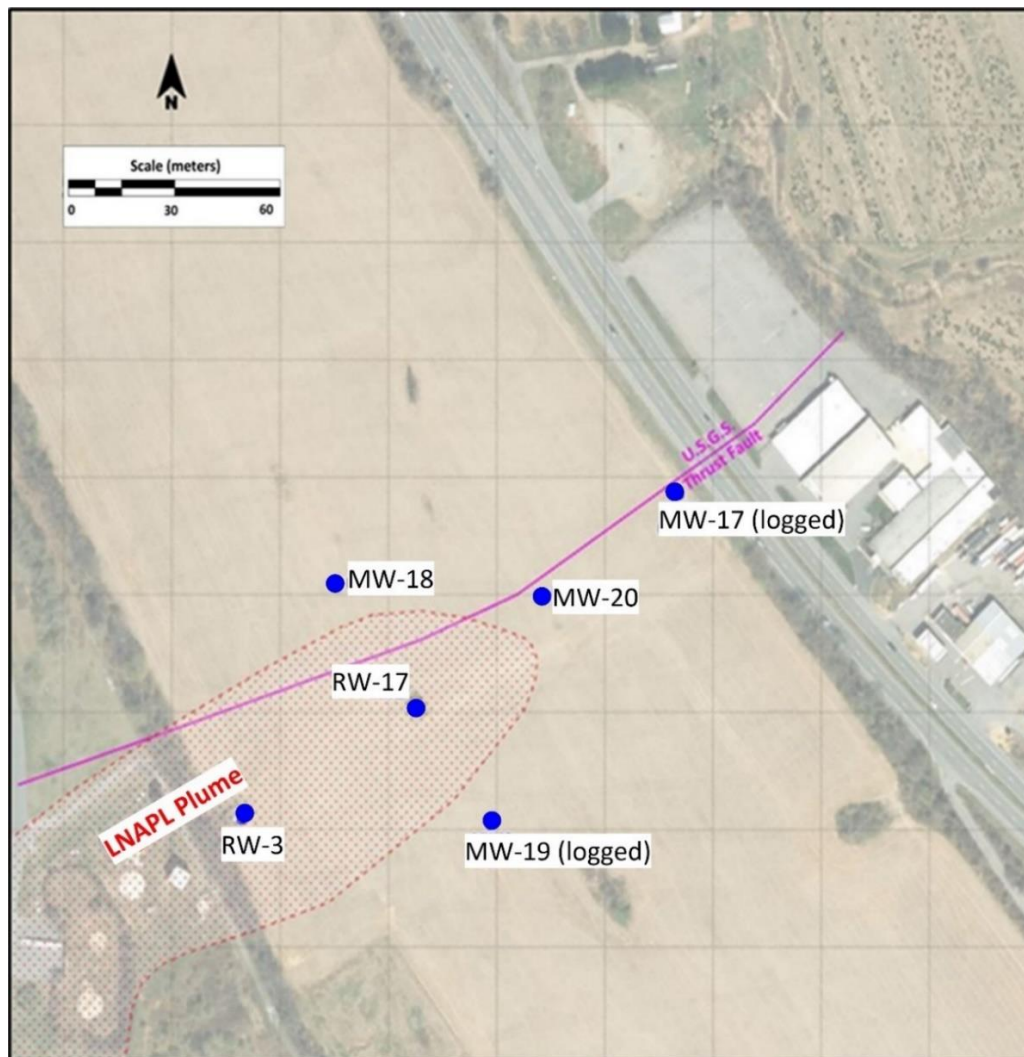


Figure 2.5 LNAPL plume, monitoring wells, and thrust fault. Logged wells were used in this study (Revised, NJGIN, 2012).

2.5 Previous Surface Geophysical Investigations at the Site

No previous surface geophysical methods have been applied at this research site since the commencement of remediation activities in 1993. The prior geophysics work completed at this site is limited to the use of downhole geophysical methods in numerous wells throughout the site. All surface geophysical data collected for this research is original and will provide the first surface geophysical datasets for this site. Because no prior electrical resistivity measurements have been completed at this site, this method will add a new perspective of the subsurface from both a qualitative and quantitative standpoint and will aid in further characterizing subsurface. ERI line placement, electrode geometry, and specific data processing methods have been used to best image the subsurface within the survey area.

2.6 Previous Downhole Geophysical Investigations at the Site

Optical televiewer data were collected in 46 bedrock monitoring wells by an environmental consultant, ENSR, between 2002 and 2004 (ENSR, 2005). The wells are sporadically situated throughout the industrial complex. Of the wells that were logged throughout the site, only six were located within the study area for this research, and only two of those six were accessible for the logging in this study (Figure 2.5). For this research, the remaining bedrock wells located within the study area were logged with the suite of borehole instruments described in Chapter 3.

The downhole geophysical data provided from ENSR identified 30 oriented bedding planes and 1,030 oriented fractures from the 46 wells. As ENSR (2005) determined, most of the bedding measurements from the borehole geophysical survey strike to the northeast, with a range of N10°E to N40°E. Additionally, it was determined that a small-scale trend in strike direction exists, with the orientations in an easterly direction between N75°E and N90°E. Based on the prior dataset, the dominant dip direction observed was to the southeast (27 of 30 observations), with varying range in dip angles from 11 degrees to 53 degrees (ENSR, 2005, p. 49).

The fracture analysis by ENSR (2005) identified 1,030 fracture planes which show a dominant fracture strike range from approximately N20°E to about N40°E. A subordinate easterly trend in fracture strike direction was observed and ranges from N75°E to N90°E. The dominant dip direction of the observed fractures was to the southeast, with dip angle range of 30 degrees to 60 degrees and an average of 44 degrees. Based on these observed geophysical responses, it was determined that bedrock fracturing at the site is generally parallel and near parallel to bedrock bedding orientation, fracture strike occurs primarily in a northeast-to-southwest orientation, and fracture planes dip generally to the southeast. The wells at the eastern side of the complex have a slightly different fracture trend, where fracture planes are generally parallel and near parallel to bedding orientation, trending roughly east-to-west, and fracture dip directions to the south. Data from the optical televiewer suggests some fractures were infilled (presumably with calcite) and were less likely to transmit groundwater than open fractures. Because of this, the fracture analysis was two-part, where open and in-filled fractures were plotted on two separate rose diagrams.

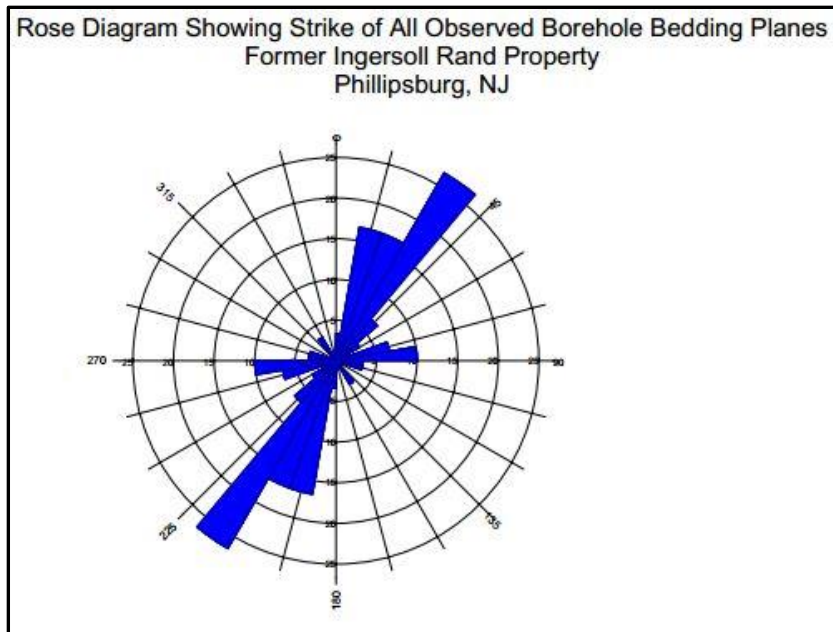


Figure 2.6 Rose diagram showing dominant strike of bedding planes (ENSR, 2005, p.50).

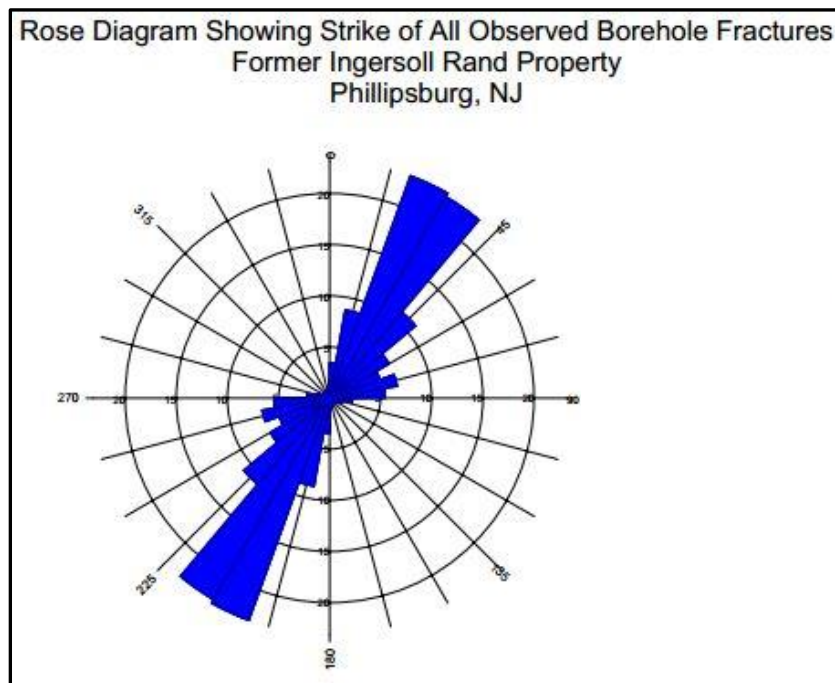


Figure 2.7 Rose diagram showing dominant strike of borehole fractures (ENSR, 2005, p.50).

CHAPTER 3

BACKGROUND: GEOPHYSICAL METHODS AND THEIR APPLICATIONS

This chapter describes the basic theory and application of the electrical resistivity imaging and downhole geophysical methods used in this research. Common uses and successful applications of these methods are then discussed in two previous studies sections shown in 3.3 and 3.6.

3.0 Electrical Resistivity Imaging Method

The electrical resistivity imaging method is used to measure the resistivity structure of subsurface materials using a direct current (DC) electrical source (typically a 12V marine battery). A DC signal is injected into the ground between two transmitting current (I) electrodes, and the resulting voltage (V) is then measured between a corresponding pair of two receiving (or potential) electrodes. The measured voltage difference is then expressed as resistance (R), or $R = \Delta V/I$. Measurements of R made through a cross sectional area (A) over some length (L) are defined as measurements of resistivity (ρ), or $\rho = R(L/A)$.

Resistivity measurements made within the Earth are a function of the geologic composition, porosity, permeability, water content, lithologic variation, and ionic makeup of the subsurface materials. Because the Earth's subsurface is not uniform in terms of its physical properties, resistivity data that are collected in ERI field surveys are considered apparent resistivity (ρ_a). The relationship of ρ_a is expressed as $\rho_a = RK$, where K is the

geometric factor determined by electrode array configuration. For this research, the dipole-dipole electrode array (K) was used and is expressed as $K = \pi n A (n+1) (n+2) (n+3)$. When the geometric properties of the dipole-dipole array are applied to ρ_a , it is then expressed as $\rho_a = \pi n (n+1) (n+2) aR$. Figure 3.0 shows the two-dimensional measurement of the dipole-dipole configuration as they are collected within the Earth. Partial data point locations are shown as red diamond shapes on the angular line stemming from the current electrode (I) and are intersected where potential (V) electrodes meet.

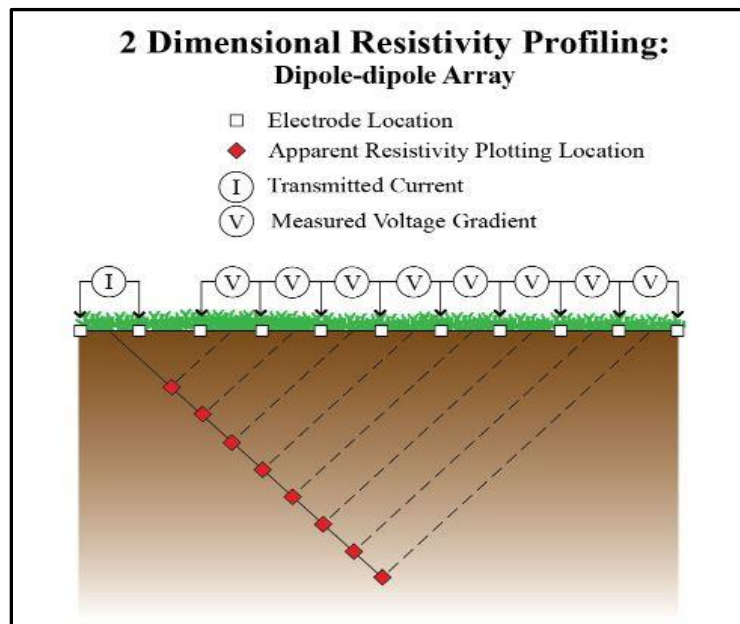


Figure 3.0 The 2D configuration of a dipole-dipole array (Wightman et.al, 2003)

3.1 Resistivity of Common Geologic Materials

Resistivity is a basic physical material property and is a measure of a given materials opposition to the flow of electrical current. Resistivity is expressed as a resistance through unit distance; thus, its SI units are in ohm–meters, or $\Omega \text{ m}$ (Monahan, 2013).

Resistivity values of geologic materials vary drastically based on both composition, susceptibility of physical and chemical weathering, and pore water content. For example, a good conductor such as copper is on the order of $10^{-8} \Omega \text{ m}$, an intermediate conductor such as wet topsoil is approximately $10 \Omega \text{ m}$, and the resistivity of a poor conductor such as sandstone is approximately $10^8 \Omega \text{ m}$. Below is a table showing resistivity of common earth materials. Note that the common resistivity values of clay, limestone, and dolomite in Table 1 applies to this research site.

Table 1. Resistivity of common Earth materials (adapted from Robinson 1988).

Earth Material	Resistivity ($\Omega \text{ m}$)	Earth Material	Resistivity ($\Omega \text{ m}$)
Granite	$10^2\text{-}10^6$	Sandstone	$1\text{-}10^8$
Diorite	$10^4\text{-}10^5$	Limestone/Dolomite	$50\text{-}10^7$
Andesite	$10^2\text{-}10^4$	Sand	$1\text{-}10^3$
Basalt	$10\text{-}10^7$	Clay	$1\text{-}10^2$
Peridotite	$10^2\text{-}10$	Brackish water	$0.3\text{-}1$
Air	∞	Seawater	0.2

3.2 A Brief Comparison of Commonly Used Electrode Geometry in Electrical Resistivity Surveys

Electrode geometry is commonly selected for a given survey to best image the subsurface in order to identify specific subsurface features in an assumed medium. The three most commonly used arrays are the Schlumberger, Wenner, and dipole-dipole configurations (Abdullah, et al., 2010). Visual aids are provided to best show the electrode

configurations. In the below figure, “A” and “B” are the current (active) electrodes, and “M” and “N” are the potential electrodes. The electrode geometries for respective configurations are listed below:

- Wenner array: $\rho_a = 2\pi aR$
- Schlumberger array: $\rho_a = \pi a^2/b (1-b^2/4a^2) R$
- Dipole-dipole array: $\rho_a = \pi n (n+1) (n+2) aR$

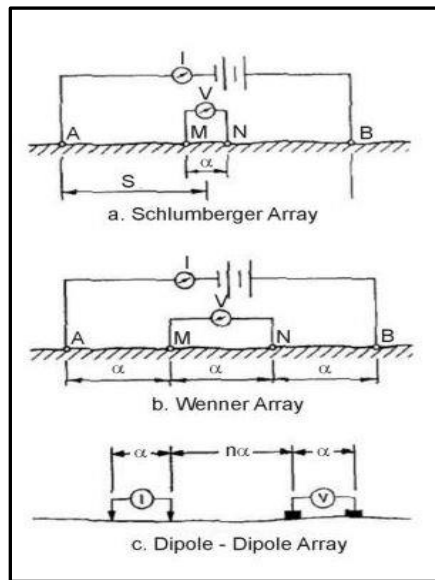


Figure 3.1 Electrode array configurations for resistivity measurements (Wightman et al., 2003.)

As Abdullah et al. (2010) observed, specific geometries such as the Wenner and dipole-dipole arrays can provide better resolution for respective targets. For example, an electrical resistivity survey using both dipole-dipole and Wenner geometries to image shallow underground cavities indicated that the Wenner configuration provided better resolution on vertical features (i.e. subsurface cavities), while the dipole-dipole configuration provided better resolution for sub-vertical features. It should be noted at this

point that the target depth and anticipated orientation of subsurface features must be considered during the array selection process. For this research, the dipole-dipole method was selected as it provides the best combination of lateral variations and sub-vertical features. The depth of investigation for this research was derived from known groundwater levels obtained from bedrock monitoring wells, where the dipole-dipole array was the most suitable choice to retain the best possible resolution with increasing depth.

3.3 Applications of the Electrical Resistivity Method

Numerous studies have evaluated the use of electrical resistivity methods in carbonate rocks. Van Schoor (2002) determined that dipole-dipole electrical resistivity data can be effective in identifying probable locations of sinkholes in dolomitic geologic setting. A dipole-dipole resistivity survey to a depth of approximately 30 m was completed to identify low resistivity zones that may be related to sinkholes which affected a nearby roadway. The survey concluded that a dipole-dipole resistivity survey is capable of discriminating between developing sinkholes (low resistivity) and air-filled sinkholes (high resistivity). Beck et al. (1999) observed the effectiveness of using ERI imaging methods for defining depth to bedrock in karst terrain. Dipole-dipole electrical resistivity imaging was used to map the bedrock surface, where the limestone bedrock was covered by nine meters of overburden. Forty-nine ERI transects were collected with an electrode spacing of three meters and transect lengths ranging from 81 m to 249 m. The results indicated that shorter lines provided greater near surface resolution at the overburden-bedrock interface, and that averaging the depth to bedrock provided a more realistic value over the approximately 42,037 m² site. This paper has indicated how dipole-dipole resistivity

measurements in a clay-dolomite environment, such as observed at this research site, can be highly effective in resolving depth-to-bedrock and bedrock undulation across a survey area.

Cabrera et al. (2010) tested the potential of electrical resistivity survey methods to detect a fault zone from the ground surface in limestone and argillaceous formations. A well-known regional fault was surveyed using 2D electrical resistivity to identify resistivity discontinuities that correspond to the position of the fault. It was determined that sub-vertical low resistivity discontinuities correspond to the upward extension of the fault, and that these upper, shallower expressions of the fault correlate to the anticipated position of the fault and continue downward and well into bedrock formations.

Electrode geometry selection is critical in resolving certain structural geologic features, especially in a karst environment. Adams et al. (2002) addressed the problem of electrode array geometry selection to best image respective karst features. Numerical forward modeling was conducted using dipole-dipole, Wenner, and Schlumberger arrays, and it was determined that a mixed array which includes data from all three arrays is typically best in karst settings, although much more time consuming and expensive. The conclusion of this analysis suggests that the dipole-dipole array is the most effective and least costly electrode configuration to apply in karst settings.

One of the few evaluations of hydrocarbon contamination using geophysics was conducted by Atekwana et al. (2000). They evaluated the utility and resolution of geoelectrical methods at a hydrocarbon contaminated site set within a glacio-fluvial geologic setting in central Michigan. The 2D electrical resistivity method was combined

with ground penetrating radar (GPR), electromagnetic (EM), and in situ soil boring data to investigate electrical properties of an LNAPL plume which resulted from 50 years of leakage into the ground. The results of the research indicated that resistivity and GPR methods can be used to observe variations in stratigraphy and subsurface structures, and further showed that low resistivity zones were coincident with both “shadow zones” observed in GPR responses (caused by greater conductivity) and observed presence LNAPL from soil borings.

Loke (2000) provided a series of successful applications of a variety of resistivity methods applied to a wide array of questions. The following list is from the case studies provided in his paper: Agricultural Pollution – Asrhus, Denmark, Odarslov Dyke – Sweden, Underground Cave – Texas, Landslide - Cangkat Jering, Malaysia, Old Tar Works – U.K., Holes in Clay Layer – U.S.A., Magusi River Ore Body – Canada, Marine Underwater Survey – U.S.A, and Time-lapse Water Infiltration Survey – U.K.

3.4 Borehole Geophysical Methods

Borehole geophysics is defined as the science of recording and analyzing physical properties made in wells or test holes, where probes measuring differing parameters are lowered into a given borehole to collect continuous or point data of the surrounding geologic material (Chu et al., 2004). Typically, a suite of geophysical logs is collected, combined, and analyzed, taking advantage of their synergistic nature, as much more can be learned by the analysis of a suite of logs than by individual analysis (Williams, 1999). Borehole geophysical methods are typically used in environmental investigations in order

to obtain information on water quality, porosity, permeability, lithology, and structural geology. Borehole geophysical systems can vary, but typically include numerous probes, winch with data communication cables and data logger, a power supply (typically a generator of sufficient power), and data recording apparatus (typically a laptop computer). Geophysical logs provide scientists and engineers with an array of useful information that allows for a clearer understanding of the subsurface of which is under investigation. The unbiased and in-situ data provides further insight into subsurface conditions than data obtained by traditional drilling samples. The suit geophysical probes used in this research are described in detail below and were selected to best provide respective subsurface information.

3.5 Borehole Geophysical Instruments

Four geophysical probes were selected for use in this investigation which totaled ten measured parameters: 1) Optical Televiewer, 2) Three Arm Caliper, 3) Multi-parameter Resistivity Probe, and 4) a Heat Pulse Flow Meter. Typically, a suite of logs can provide a more detailed characteristics of borehole conditions than utilizing a single probe. Detailed explanations and common uses of the downhole probes used in this research have been defined below.

3.5.1 Optical Televiewer

An optical televiewer (OPTV) log records a 360-degree optical image of the borehole through the use of an oriented (magnetic north), downhole RGB (red, green, blue)

CCD (charged-coupled device) camera (Advanced Logic Technology, n.d.). From this oriented image, character, relation, and orientation of lithologic and structural planar features can be studied of fractured rock aquifers (Johnson et al., 2004). The OPTV image is typically presented in an unwrapped format, such that the inner borehole wall is fully displayed. Planar fractures running through the borehole appear as sinusoids in the unwrapped image. These sinusoids can then be curve-matched and modelled to determine the apparent dip direction and dip angle of a given fracture. The OPTV log provides fine fracture definition, high resolution of formation features, and variations in formation color (Table 2.2). Applications of the OPTV are primarily used to for identifying the structural geologic features shown in Table 2 below.

	Tectonic	Sedimentary	Diagenetic
Self-evident	Structural dip	Bedding surfaces	Stylotites (high amplitude peaks)
	Natural Fractures Drilling	Laminations	
	induced fracture/ breakout	Cross-bedding	
	Folds	Grading	
		Erosional surfaces	
		Deformation features	
Ambiguous	Faults	Cobbles, pebbles, Breccia	Nodular concretions
		Detrial shales, ripples	Cherts
		Bioturbation	Vugs
		Grain size/texture	
Needs Core	Small fractures	Bioturbation	Stylotites (low amplitude peaks)
	Horizontal fractures	Thin lamination	
		Limestone textures	

Table 2 Tectonic, sedimentary and diagenetic features usually recognized on borehole images (Pezard et al., 2007).

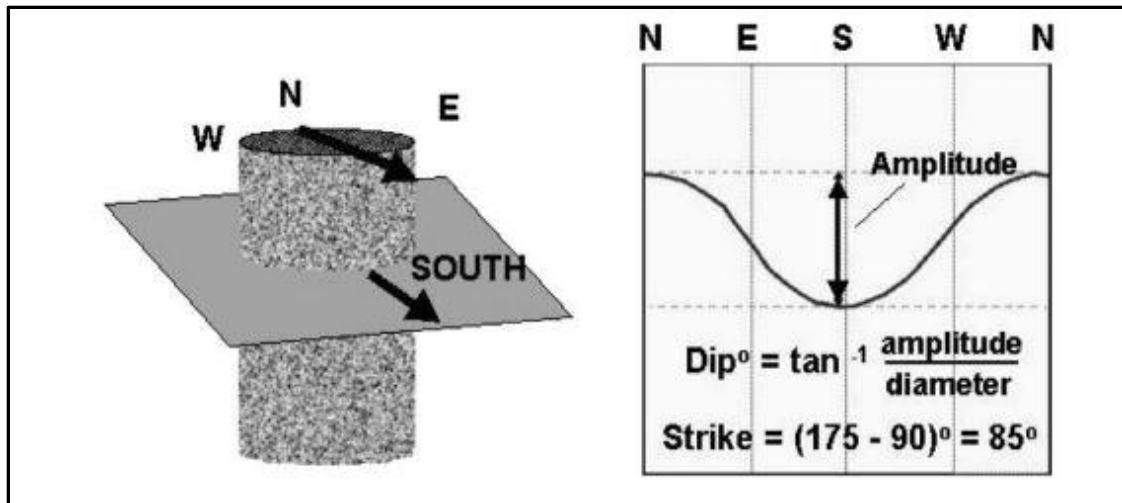


Figure 3.2: Strike/dip from OPTV logs (Johnson et al., 2004).

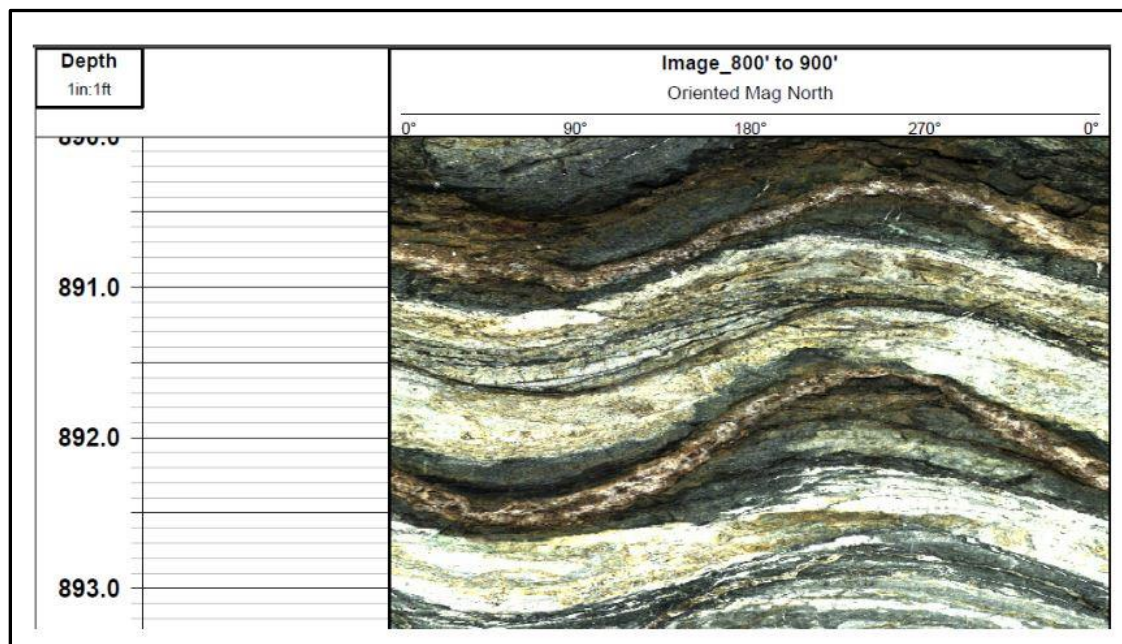


Figure 3.3: Example output for OPTV data (Mount Sopris Instruments, 2018).

As Chu et al. (2004) observed, OPTV data can be extremely useful for determining dip azimuth and apparent dip angles of fractures, fracture population and fracture density, fracture aperture and other fracture and formation characteristics such as variations in coloring and mineralogical infilling of fractures. They suggest that structural data obtained

from OPTV logs can be further evaluated using supplemental geophysical, hydrogeophysical, and hydrogeologic data to draw correlations between measured structural features from the OPTV logs to variations in lithology, flow, or large-scale regional trends that may influence groundwater movement (Chu et al., 2004). Although this particular report describes the measurement of structural features in a crystalline rock environment, the principal of the measurements can still be used in a sedimentary bedrock setting.

3.5.2 Three-arm Caliper Probe

A three-arm caliper instrument records a continuous record of borehole diameter with respect to depth. Three mechanically coupled arms apply constant pressure to the borehole wall, record variation in borehole diameter, and sends an electronic signal along the wireline to a laptop computer for real time evaluation. Abrupt increases along the line graph represent variations in borehole diameter. These peak responses are typically associated with natural openings such as fractures, bedding plane features, voids, and the breakup of fractured rocks during the drilling process. Applications of the Three Arm Caliper probe are primarily used for borehole diameter measurement, volume calculation (prior to borehole completion/cementation), fracture and void location (depth), fracture density evaluation, and bedrock integrity (or competency).

Figure 3.6 below depicts the standard caliper probe operation within the borehole. The probe is lowered to the bottom of the borehole and opened prior to starting data collection so as not damage the instrument. Standard data output shown below is

mimicking the openings in the borehole wall and is intended to show this mechanical effect. Data outputs vary greatly, but a log format showing a graph where depth is on the y-axis and the borehole diameter is on the x-axis, thus showing variations in borehole diameter with respect to depth. Note that in this format, a flat line in the center of the log represents a non-variation scenario (well casing), and deviations can occur on both left and right from log center (bedrock).

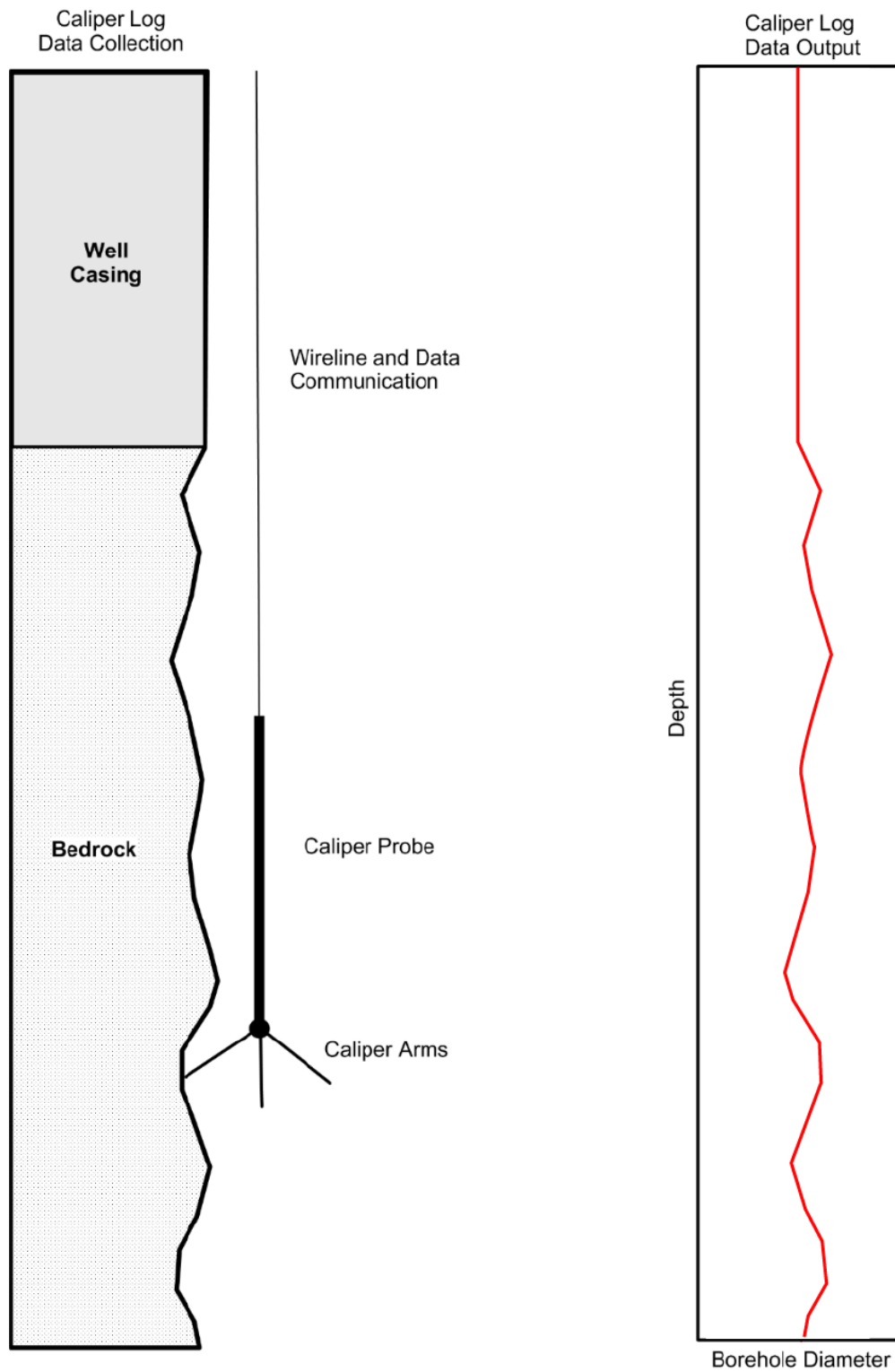


Figure 3.4: Conceptual drawing of caliper probe and data output (original).

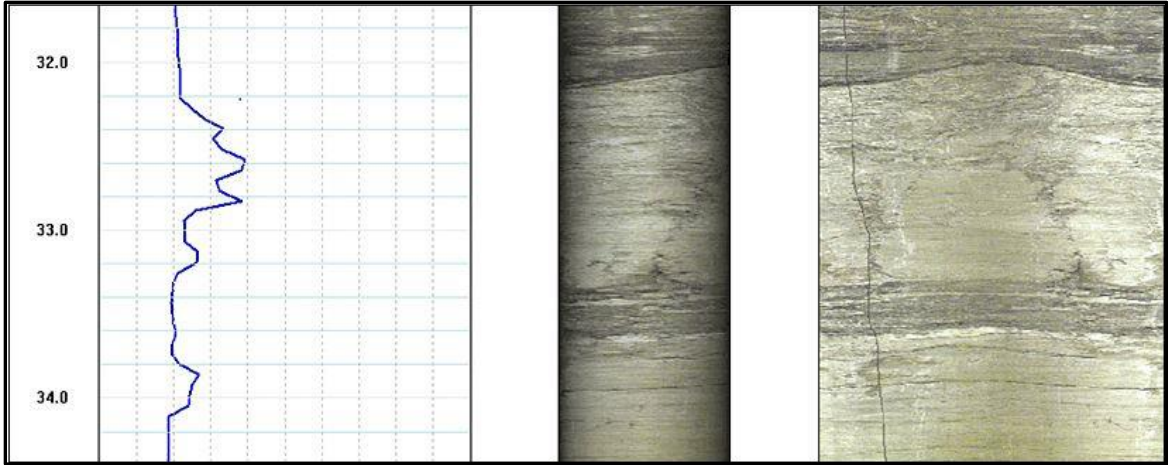


Figure 3.5: Caliper data output adjacent to OPTV log (Mount Sopris Instruments, 2017).

Figure 3.7 shows a typical Three Arm Caliper response adjacent to two OPTV logs. The y-axis represents depth and the x-axis represents borehole diameter. Typically, the low or constant responses are scaled with respect to both borehole diameter and peak response values; an example, for instance, would be an 8 cm to 23 cm scale for a 15 cm borehole, where the 15 cm reference point is centered along the x-axis. This is done to best depict fracture openings, density, and overall competency of the borehole. Note that the peak response in Figure 2.7 appears to correlate with possible bedrock fractures on the OPTV logs (right).

3.5.3 Multi-parameter Resistivity Tool

A gamma ray/fluid resistivity/temperature probe, or multi-tool (MT), measures a continuous record of these parameters as the probe moves vertically within the borehole. Changes in values of these parameters at a particular depth may indicate a water-producing

(temperature/fluid resistivity curves), a change in lithology (gamma ray/ resistivity curves) or other hydrogeologic characteristics. For example, localized minor variations in fluid temperature or resistivity values may indicate that groundwater with a slightly different temperature or composition is entering a given borehole at some measured depth.

Similarly, changes in lithology can be determined when significant variations in gamma ray and resistivity responses are observed, where an increase or decrease in gamma or resistivity responses are directly related to the amount of potassium, uranium, thorium, and saturation, such as in a dry sand-to-moist clay scenario; given this scenario, low gamma/high resistivity values should be observed in dry sand, and high gamma/low resistivity values should be observed in moist-clay units. The MT measures 8", 16", 32", and 64" (or 20 cm, 40 cm, 80 cm, and 160 cm) normal resistivity, single point resistance (SPR), fluid temperature, fluid resistivity, and natural (or passive) formation gamma responses. Applications of the multi-tool are typically used to identify possible water-bearing zones, possible fractures, determine lithologic variation, facies change, and bedrock integrity (or competency).

3.5.4 Heat Pulse Flow Meter

A heat pulse flow meter (HPFM) probe measures vertical flow within the borehole. The probe is charged with an electrical current and subsequently introduces a heat pulse into the water column. Canisters containing temperature sensitive sensors are located above and below the release point of the heat pulse. When temperature increases are detected above or below the release point of the heat pulse, vertical flow can be obtained by

calculating the time it takes the heat move up or down a given borehole to a receiving canister. The probe is suited best for low-flow environments and has a detection limit of 0.05 to 1.0 gallons per minute (gpm).

3.6 Applications of Borehole Geophysical Methods

Instrumentation selection for borehole geophysical investigations is crucial. One of the primary pieces of literature describing the benefits and limitations of logging instruments is *A Practical Guide to Borehole Geophysics in Environmental Investigations* (Keys, 1997). The book describes numerous applications of borehole geophysics in correlating lithology, determining porosity and permeability, fracture location and characterization, locating contaminant plumes, verification of well construction/integrity, and locating the perched water and the water table. The book further describes log analysis from both a qualitative and quantitative perspective and emphasizes quality control. Case histories from Loring Airforce Base, Cape Cod, and Idaho National Engineering Laboratory are provided and show the success of borehole logging applied in respective conditions.

A key measurement in determining vertical flow and aquifer conditions in a karst environment is the heat pulse flow meter measurement. Crowner et al. (1996) discuss the applications of a high-resolution heat pulse flowmeter probe. The benefits of such fine measurements are discussed based on the probes ability to measure very low flow (0.01 gal/minute). Specific useful applications discussed are the ability to relate vertical flow measurements to aquifer hydraulics, permeability, characteristics of groundwater flow

(over time), and the usefulness of the probe to determine apparent flow connections between wells. As observed at this research site, Johnson et al. (2004) also successfully used acoustic and optical borehole imaging techniques in a fractured rock aquifer study. Although similar data are acquired, the two instruments are compared, and both the benefits and drawbacks are discussed. For example, structural features are better defined in areas where dark colored rocks limit the visual output of the optical televiewer. Conversely, the optical televiewer can allow direct viewing of changes in lithology, and relate to fractures, foliation, and bedding.

Haeni et al. (2002) conducted a borehole geophysical investigation to characterize the hydrogeology of the fractured-rock aquifer and the distribution of unconsolidated glacial deposits near a former landfill in Storrs, Connecticut. The survey consisted of caliper, gamma, fluid temperature, fluid resistivity, induction, heat pulse flowmeter, and optical and acoustic imaging measurements. The suite of logs was successfully used to characterize fractures, foliations, variations in lithology and hydrogeologic parameters. This study emphasizes the importance of utilizing a suite of probes in a borehole investigation in order to make proper interpretations, such as implemented in this research. Bradbury et al. (2001) used natural gamma log data to correlate variations in lithology to stratigraphic and hydrogeological data collected in 14 high-permeability zones. The gamma logs were used to identify relative stratigraphic positions of flow features in each well. Flow features were then correlated with specific stratigraphic horizons. Although no major variations in gamma responses were anticipated at this research site, this paper helped in geophysical survey design.

CHAPTER 4

METHODS: SURVEY DESIGN, DATA QUALITY, AND DATA PROCESSING

This chapter describes the geophysical survey design, data quality, and data processing techniques of the geophysical measurements used in this study. The combined ERI and downhole approach for this research is discussed in detail below. This chapter further explains the processes for ensuring data quality for pre-and-post survey results and defines the following charts and plots used as visual representations for data quality control. These charts include: Contact Resistance Test, Crossplot of Measured vs. Apparent Res Data, Scatterplot of Repeat Measurement Errors (%), and Data Misfit Histogram for Removal of Poorly Fit Data charts.

4.0 Electrical Resistivity Imaging Survey Design

The locations and orientations of six ERI Lines were selected in order to best image upper expressions of an anticipated thrust fault identified by the USGS and to ensure data were collected directly over and surrounding the documented LNAPL plume (Figure 4.0). Because the apparent LNAPL plume boundary interpretation is based on nearby bedrock wells, it is subject to vary in actual distribution as a direct result of the contouring process. Moreover, since it was hypothesized that the strike of the thrust fault was a significant structural feature contributing to plume migration, the ERI Lines 1-4 were oriented roughly perpendicular (northwest-to-southeast) to the fault strike, where the USGS plotted fault line fell laterally along these line at their respective center points. Both the USGS fault and plume boundary were scaled and overlaid onto a high-resolution, georeferenced

orthophoto. Six proposed ERI lines with lengths of 202 meters each were then drawn onto the map, and coordinates were obtained for the start and end points of each line from the map to be used as line placement positions in the field. Note that the map scale on Figure 4.0 is in U.S. survey feet because SI units were not available from the New Jersey Geographic Information Network (NJGIN) database.

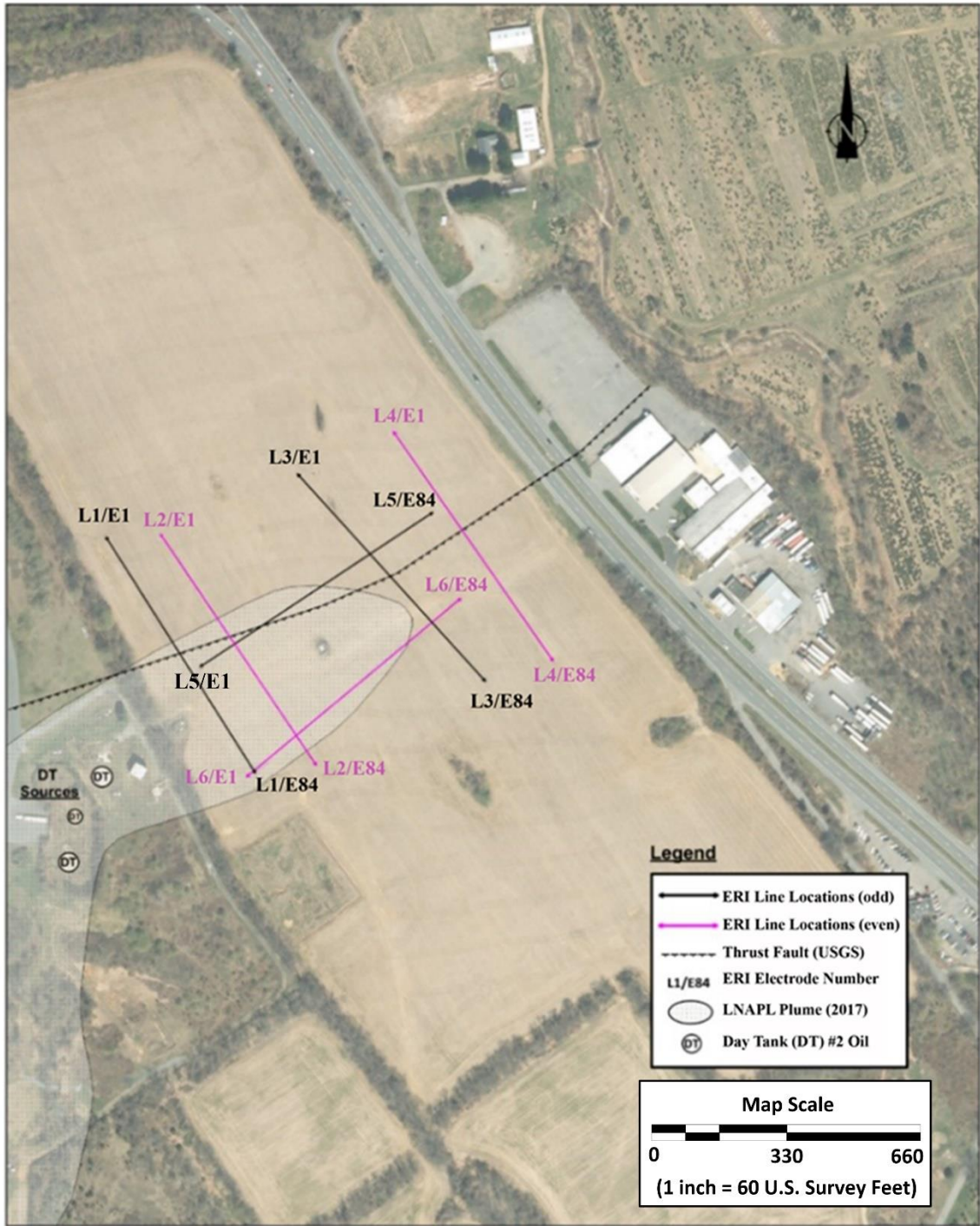


Figure 4.0 ERI line placement, LNAPL plume, source, and USGS fault (NJGIN, 2012).

4.1 Procedures Prior to Field Setup

Prior to collecting resistivity data in the field, a Command File (.cmd) was generated in the Administrator software from Advanced Geosciences, Inc. (AGI) which defines specific geometric data collection parameters. Electrode geometries are selected, and maximum spacing units are defined. For this survey, the dipole-dipole array type was selected with a max n spacing of 2.4 m and the max dipole was set to 26, which is the default setting, as shown in Figure 4.1 (AGI, 2018). After the .cmd file was created, it was stored on a removable drive and uploaded to the system's internal hard drive.

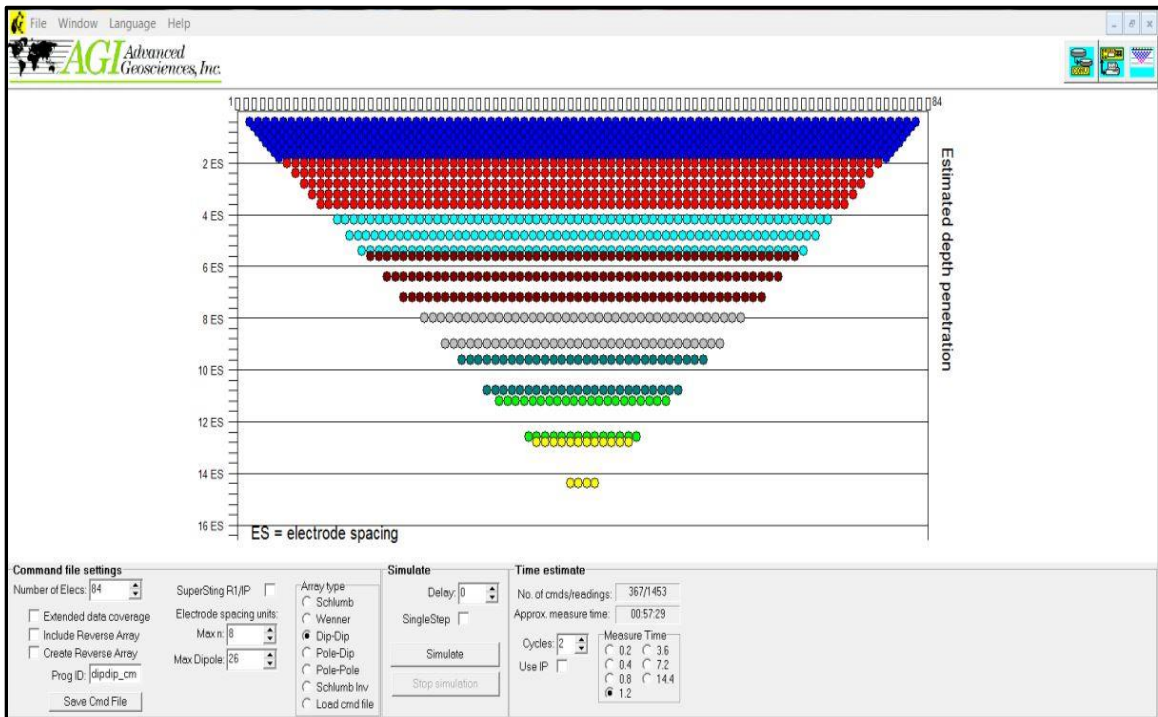


Figure 4.1 Command file created in AGI Administrator.

4.2 Electrical Resistivity Imaging Survey Procedures

The SuperSting Swift automatic multi-electrode system used in this investigation consisted of 84 electrodes. The Swift controller is connected directly to the Sting R-8/IP resistivity meter which was pre-programmed using the Administrator software by Earth Imager to collect data using the dipole-dipole configuration (AGI, 2018). Two 90-meter and one 30-meter tape measures were pulled to the total length of the ERI spread for referencing placement of each electrode. The electrodes were spaced 2.44 meters apart at a total length of 202 meters to provide an anticipated depth of investigation of approximately 27.8 meters below ground surface, respectively. Upon completion of the electrode array set-up, electrode contact resistance tests were conducted to ensure that all electrodes were correctly attached prior to starting data collection, and that the resistance between the ground and the electrodes were within an acceptable range as suggested by the equipment manufacturer. Upon the completion of the contact resistance test, the resistivity meter was set to automatically sample the dipole-dipole data.

4.3 Contact Resistance Test (CRT)

The contact resistance test measures the contact and ground resistance throughout the cable alignment. At the start of the test, the instrument releases a current from the 12V source between the first two electrodes only, while at the same time measuring voltage. As the AGI manual states, a value comprising the contact resistance between the first stake and the ground, the resistance in the ground and the contact resistance between the ground and the second stake will be measured (AGI, 2018). This test continues throughout

subsequent electrodes 2-3, 3-4, etc., until the test is complete. Contact resistance values are shown on the screen and can be viewed in real time to ensure the contact resistance values fall within the acceptable range of 150 Ω to 2000 Ω , as defined by the manufacturer.

All contact resistance values that fell outside of the 150 Ω to 2000 Ω range during the in-field test were checked for poor electrode cable-stake connections and the contact between the stake and the ground. Common connection corrections were encountered in the field such as poor stake sitting (e.g. not deep enough) and breakages in rubber bands holding the cable contacts to the ground stake. When high values or errors were displayed on the screen during this process, the test stopped until the problem was fixed. After any connection error was identified in the field, it was then corrected, and the contact resistance test would restart from electrode 1. Contact resistance test results for Lines 1-6 were stored on an internal hard drive on the SuperSting system and were later extracted and subsequently plotted for a visual representation of test results. The data outputs of each chart are provided below as well as brief descriptions of the distribution of contact resistance values and general characteristics of each chart. These charts (i.e. Figure 4.21) represent the actual CRT results obtained prior to starting data collection for each ERI line in the field.

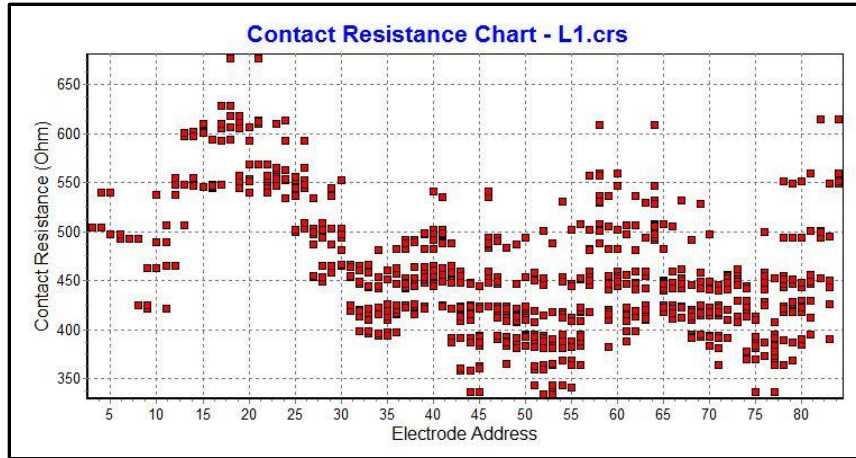


Figure 4.2 Line 1 – contact resistance chart. The Contact Resistance Chart (CRC) for Line 1 shows resistance values with a range of approximately 325 Ω to 675 Ω . Generally, variations in contact resistance (CR) values are greatest between electrode address (EA) 1 to EA 27, where a tighter clustering is present for the remaining electrodes. All CR values fall between 150 Ω to 2000 Ω .

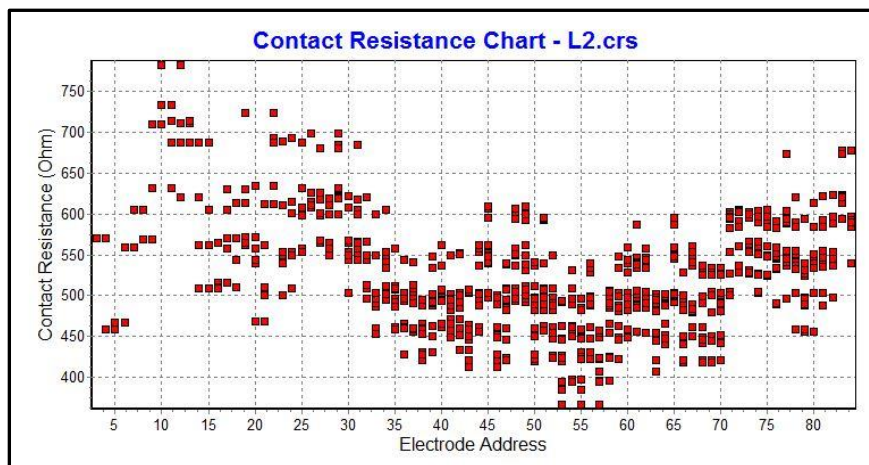


Figure 4.2.1 Line 2– contact resistance chart. The CRC for Line 2 shows resistance values with a range of approximately 325 Ω to 775 Ω . Greater variation occurs between EA 1-25, followed by a tighter grouping of values to the end of the spread. All CR values fall within the acceptable range of 150 Ω to 2000 Ω .

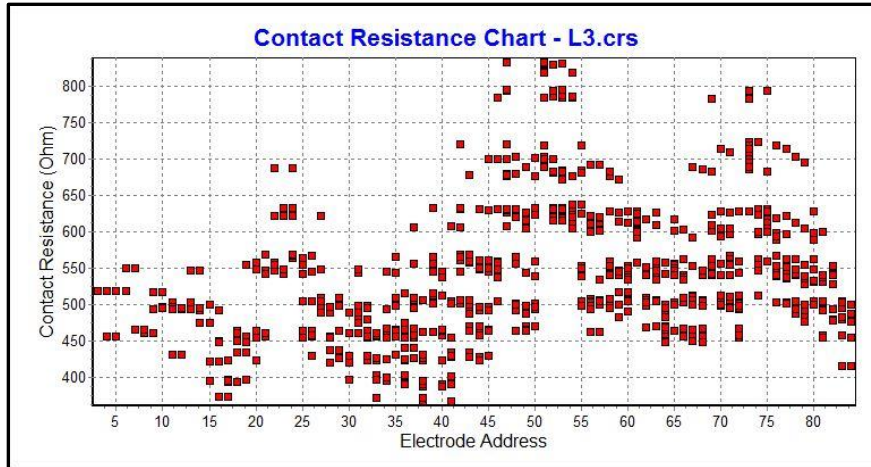


Figure 4.2.2 Line 3 – contact resistance chart. The CRC for Line 3 shows resistance values with a range of approximately 325 Ω to 850 Ω . Although the data appears more sporadic than observed on CRT Charts 1 and 2, the results of this test still fall well within the acceptable CR range of 150 Ω to 2000 Ω .

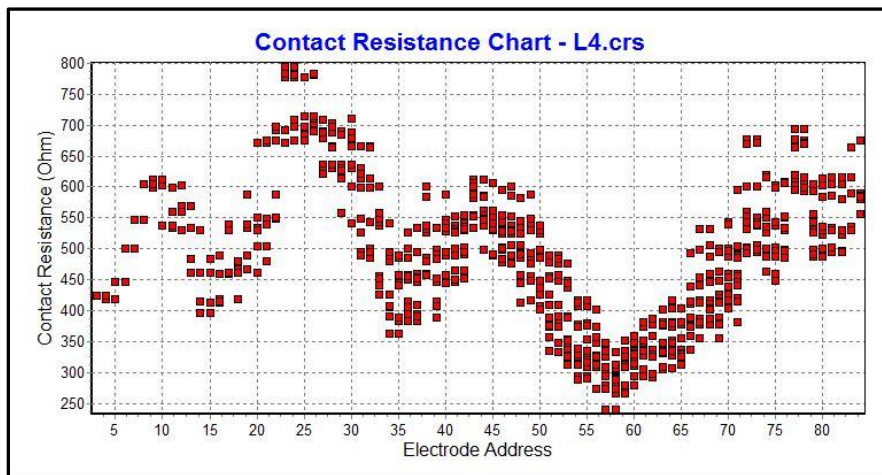


Figure 4.2.3 Line 4 – contact resistance chart. The CRC for Line 4 shows resistance values with a range of approximately 225 Ω to 800 Ω . The wave-like plot of responses shows a relatively tight cluster of data points which appear to vary closely, with respect to nearby data points. All values fall within the acceptable 150 Ω to 2000 Ω range.

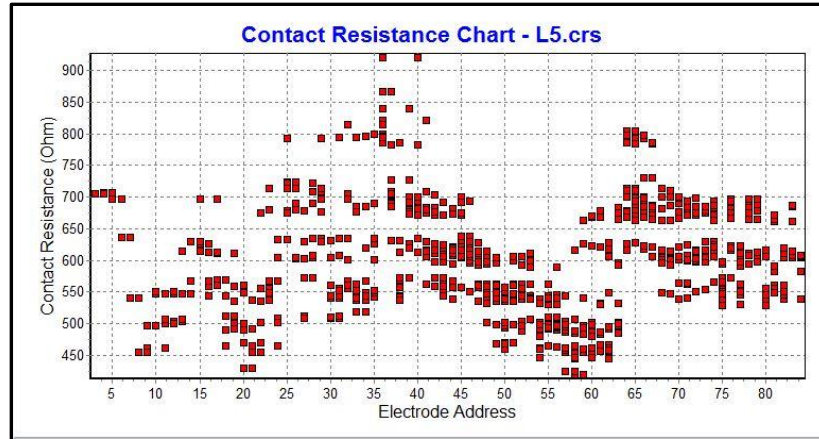


Figure 4.2.4 Line 5 – contact resistance chart. The CRC for Line 5 shows resistance values with a range of approximately 425 Ω to 925 Ω . In general, greater variation plotted data responses is observed between EA 1-36, and gradually becomes less varied from electrode 37-84. These values all fall within the acceptable range of 150 Ω to 2000 Ω .

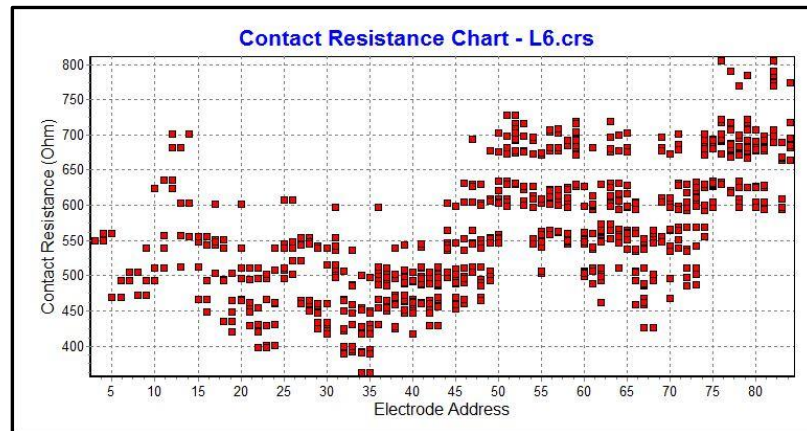


Figure 4.2.5 Line 6 – contact resistance chart. The CRC for Line 6 shows resistance values with a range of approximately 325 Ω to 810 Ω . The chart shows a collective, wave-like characteristic with slight increases in responses values as the test moved along the line from EA 1 to EA 84. A tight clustering of data points is displayed, where all values are between 150 Ω to 2000 Ω .

4.4 Electrical Resistivity Imaging Data Processing

The ERI data were processed and analyzed using Earth Imager software by AGI. The raw data were downloaded to a laptop computer, processed through a detailed and predetermined resistivity inversion algorithm (described in section 4.5), and viewed in the field to further ensure data quality prior to removal of the electrodes and cabling. Resulting cross-sectional resistivity profiles were then generated for each line. Annotations were later added which show significant resistivity boundaries and interpreted geologic conditions associated with the distribution of the resistivity measurements.

4.5 A Qualitative Explanation of Geophysical Inversion

The process of geophysical inversion to generate an interpretable electrical cross section of the subsurface is multifaceted. The main required parameters to generate the most accurate model of the distribution of physical properties within the Earth require measured data (e.g. resistivity measurements), prior information (i.e. geologic or well log data), and an inversion algorithm. The goal of this is to generate the most accurate model of data distribution within the subsurface and to relate those distributions to Earth structure.

Inversion is simply the process of estimating a best-fit model from an infinite set, when data are available. The inversion process first begins with the estimation for the Earth model based on available data. Next, a forward calculation of that model predicts what the measurements would be if the survey was completed over the initial model, where the resulting dataset is referred to as the predicted data. The results of which are then compared

to the predictions made in the initial model, and the calculated and predicted data are then compared to show the best fit model. Once the data have been compared and a close fit has been determined, the data can then be inverted again for a more accurate model. This iterative inversion process has been applied to each resistivity model below, where the appropriate iteration was selected based on the model output which likely best depicts actual subsurface conditions.

4.6 Data Quality Outputs and Poorly Fit Data Removal

Cross Plot of Measured vs. Predicted Apparent Resistivity Data

This cross plot of measured versus predicted apparent resistivity shows the relationship between the measured (or raw data) versus the predicted apparent resistivity values. Large variations along the line are shown as outliers and are plotted farther away; therefore, more closely spaced data indicates a best fit.

Scatterplot of Repeat Measurement Errors (%):

The scatterplot of repeat measurement errors shows the percent error for a given node (data point) within the dataset. Zero percent error points are indicated with blue, with increasing percent error values following an increasing sequence and area displayed as green, yellow, and red, which indicates the greatest percent error.

Data Misfit Histogram for Removal of Poorly Fit Data:

The data misfit histogram shown below is the final data quality processing technique prior to inverting the data to produce an apparent resistivity cross section. This output allows users of the software to remove poorly fit data and should be completed prior to inverting datasets to ensure that the most accurate dataset is being processed.

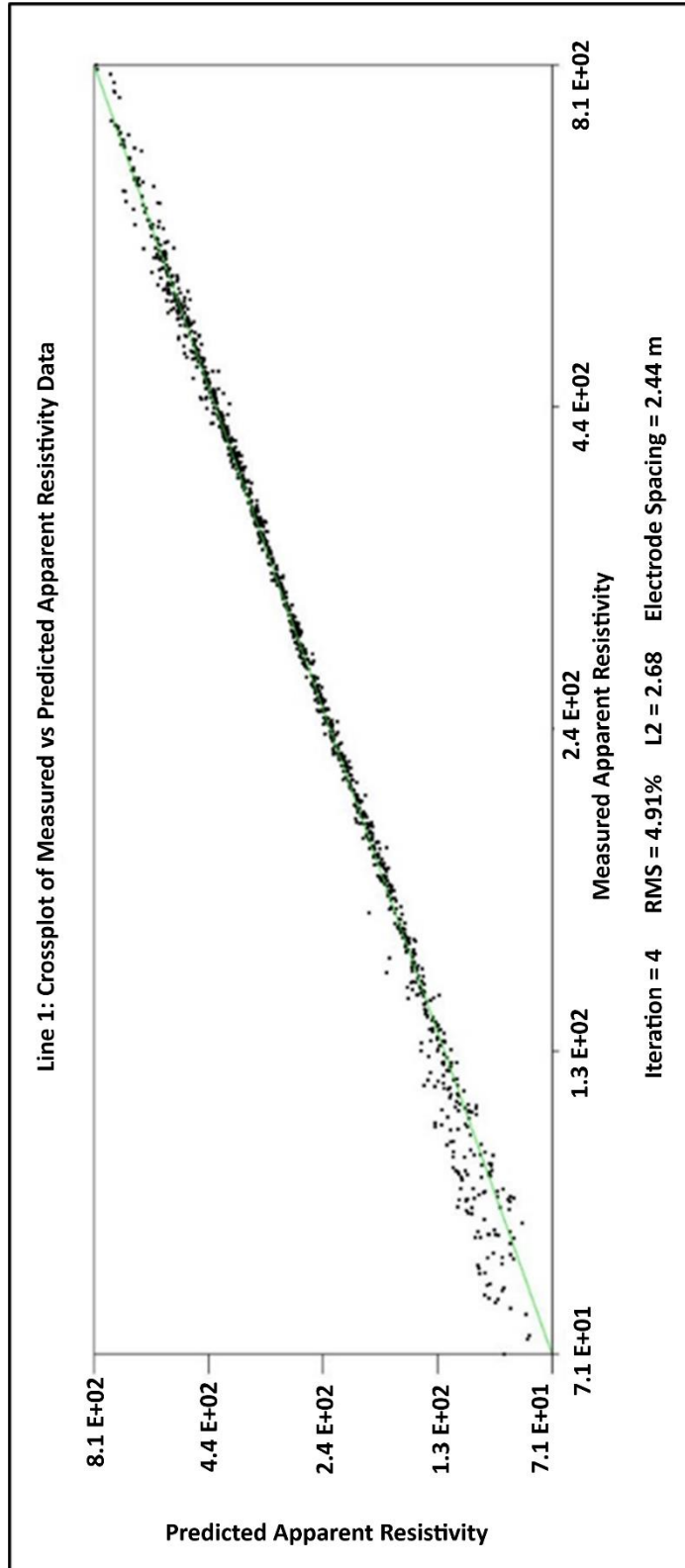


Figure 4.3 Line 1 – cross plot of measured vs. predicted apparent resistivity

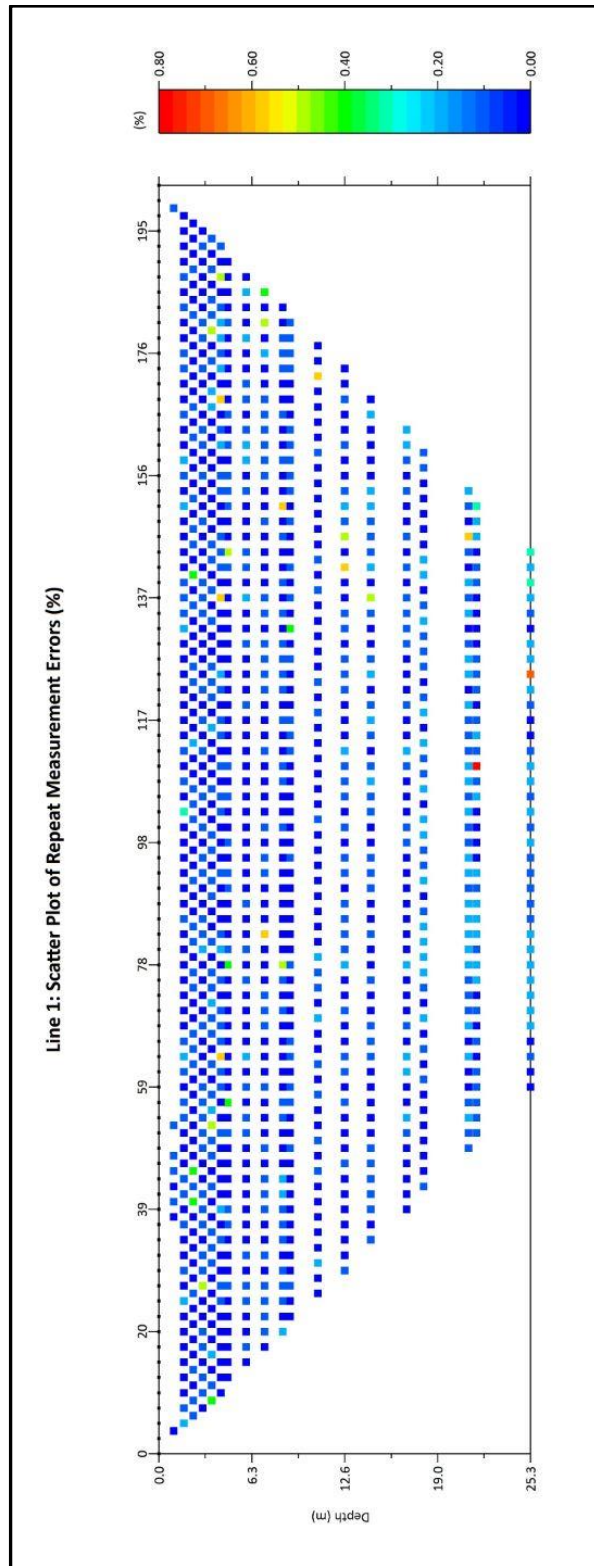


Figure 4.3.1 Line 1 – scatter plot of repeat measurement errors (%)

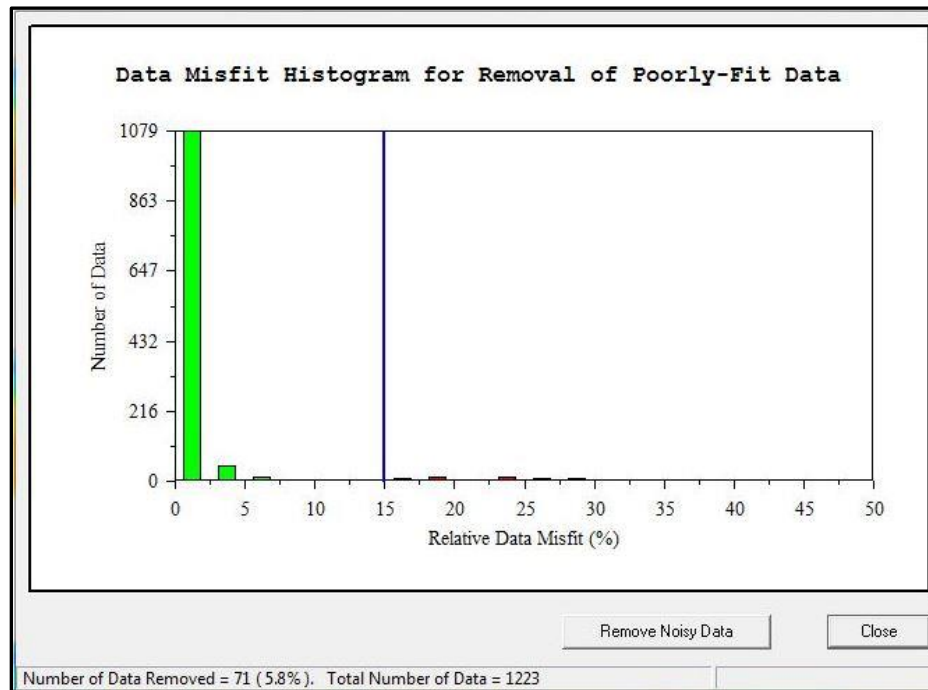


Figure 4.3.2 Line 1 – data misfit histogram for removal of poorly-fit data

Prior to processing the data through the inversion algorithm, all data misfits were removed. Figure 3.42 above shows that a very low percentage of data points needed to be removed. The total number of data points above is 1,223, where the software quality control measure suggested the removal of 71 data points, giving a total of 5 percent removal. The manufacturer suggests that this value does not exceed 10 percent of an entire dataset. It should be restated at this point that the data removal process shown above is completed after the initial inversion. This is to identify excessive data misfits that may affect the final output for the apparent resistivity sections. It should further be noted that there will always be some relative data misfit, and that repetitive data removal can become counter-effective, where the data becomes over-processed.

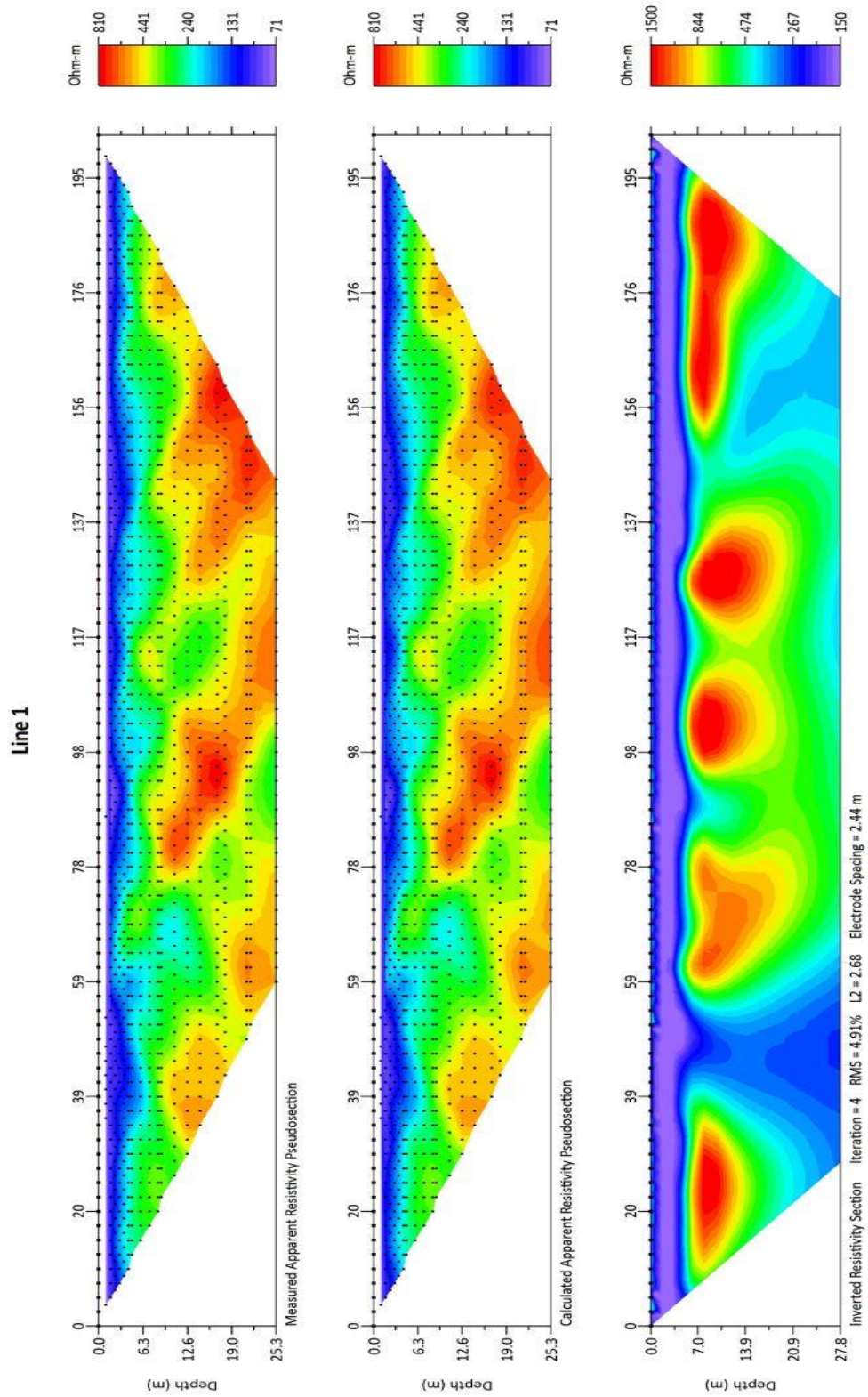


Figure 4.3.3 Line 1 – measured/calculated pseudo sections and inverted resistivity section

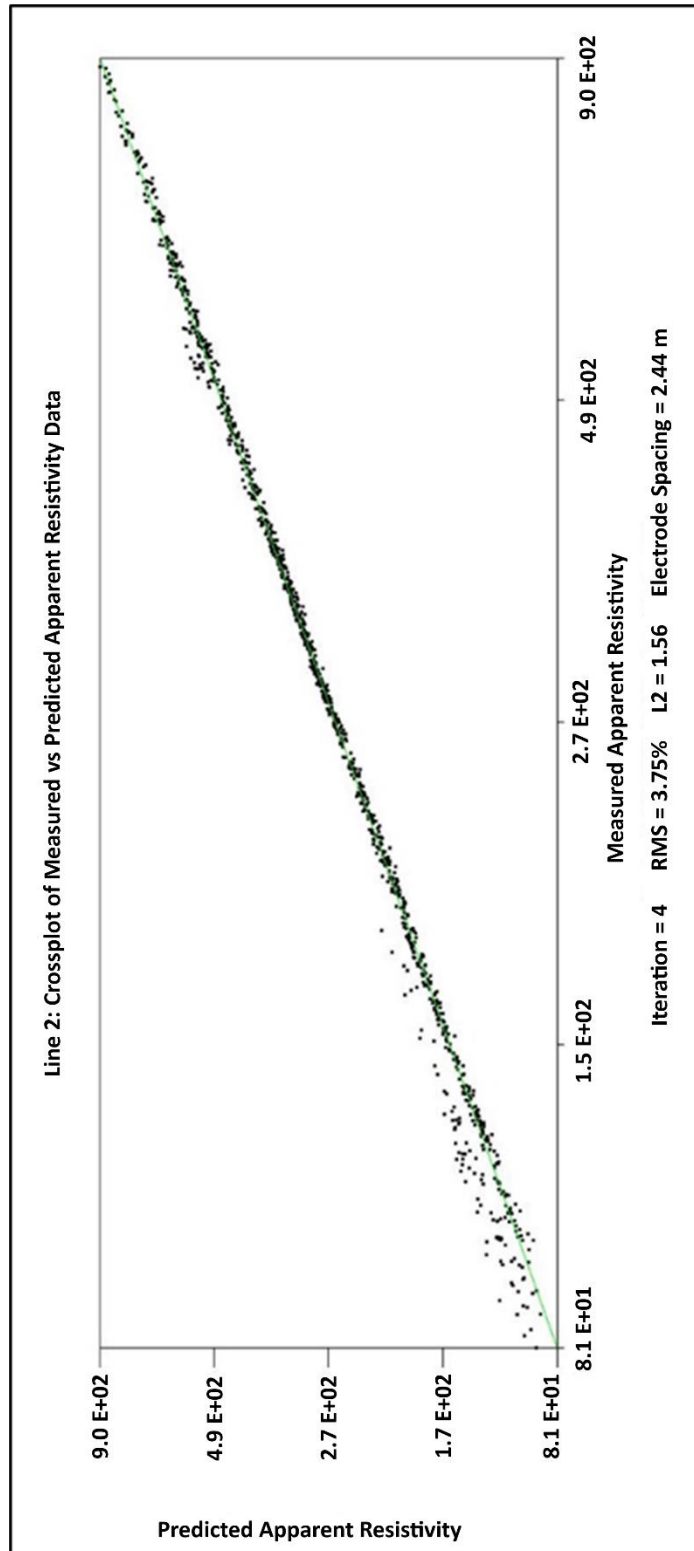


Figure 4.4 Line 2 – cross plot of measured vs. predicted apparent resistivity

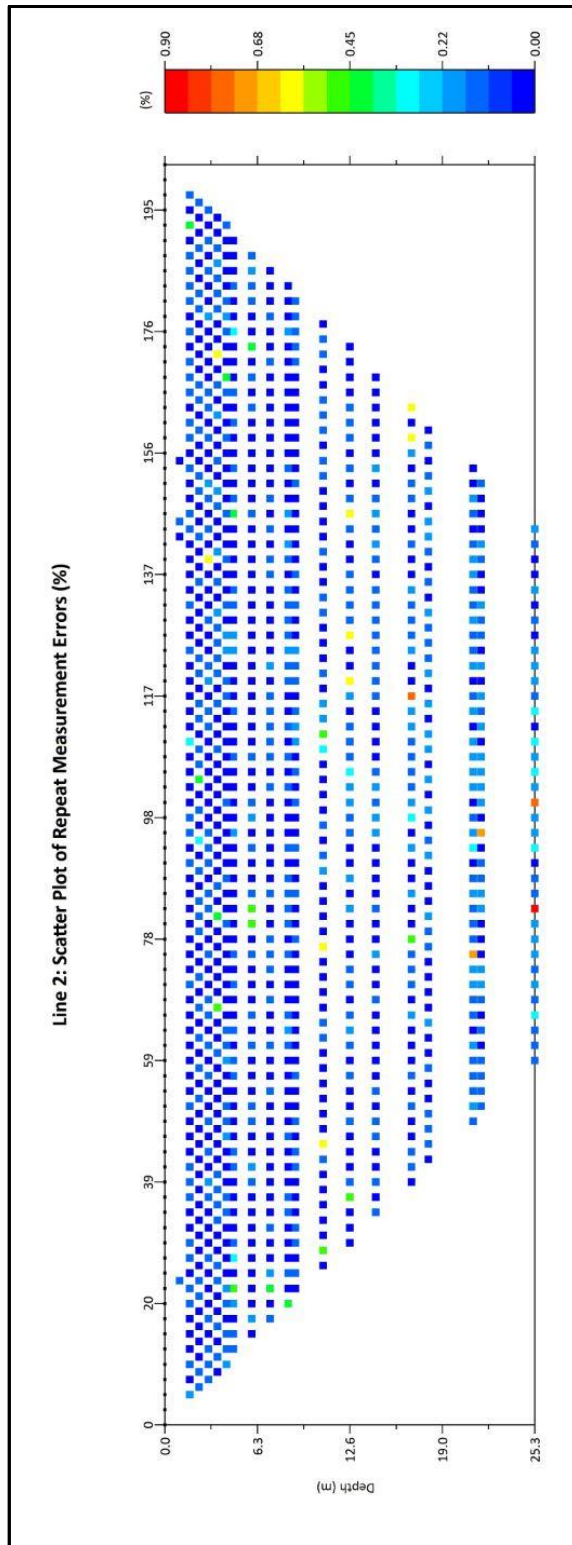


Figure 4.4.1 Line 2 – scatter plot of repeat measurement errors (%)

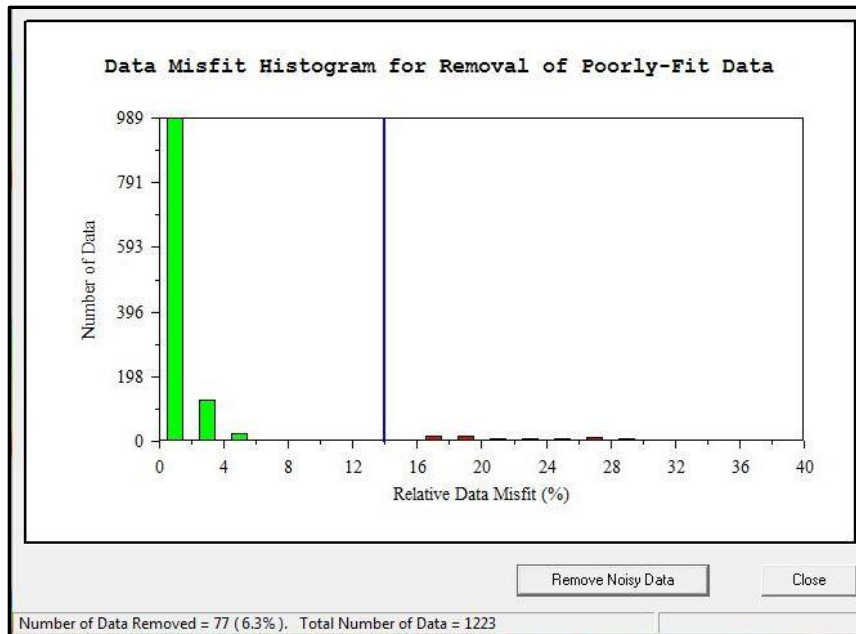


Figure 4.4.2 Line 2 – data misfit histogram for removal of poorly-fit data.

All identified data misfits observed above were removed from the Line 2 dataset. Figure 4.42 above shows that a very low percentage of data points needed to be removed. The total number of data points above is 1,223, where the software quality control measure suggested the removal of 77 data points, giving a total of 6.3 percent total removal. This falls well within the manufacturer- suggested range of 10 percent or less. Following the removal of the data misfits, the Line 2 dataset was inverted again to ensure the data quality of the apparent resistivity section was optimized.

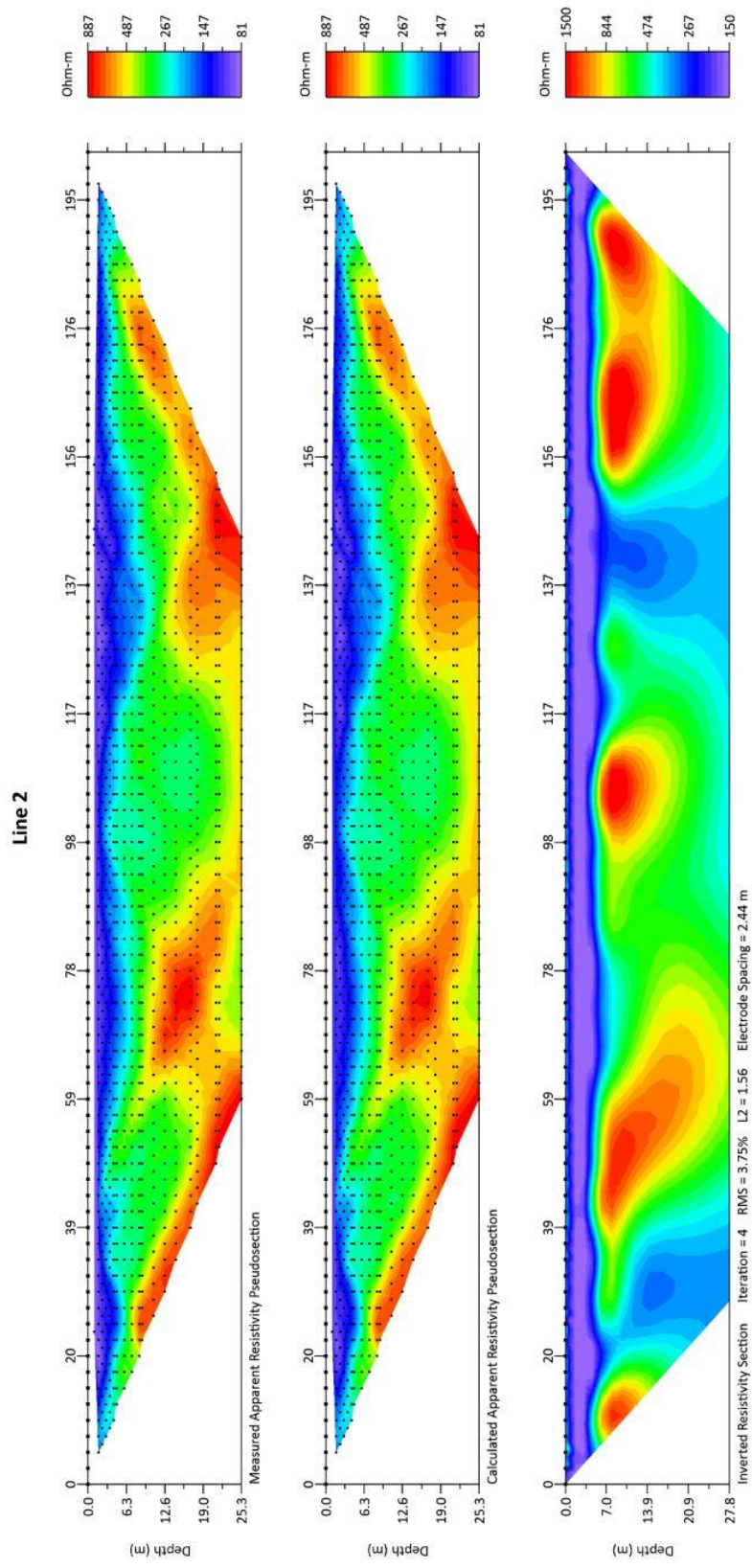


Figure 4.4.3 Line 2 – measured/calculated pseudo sections and inverted resistivity section

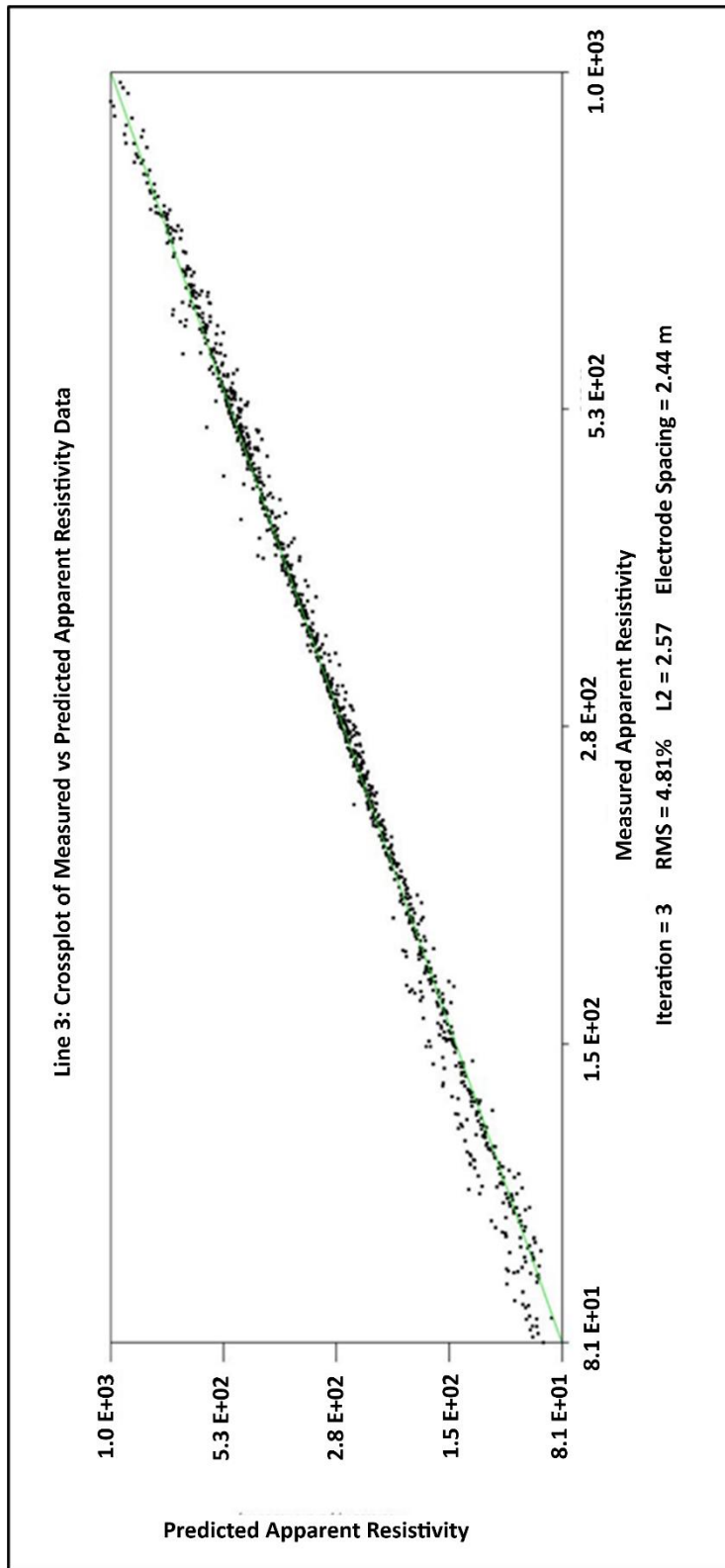


Figure 4.5 Line 3 – cross plot of measured vs. predicted apparent resistivity

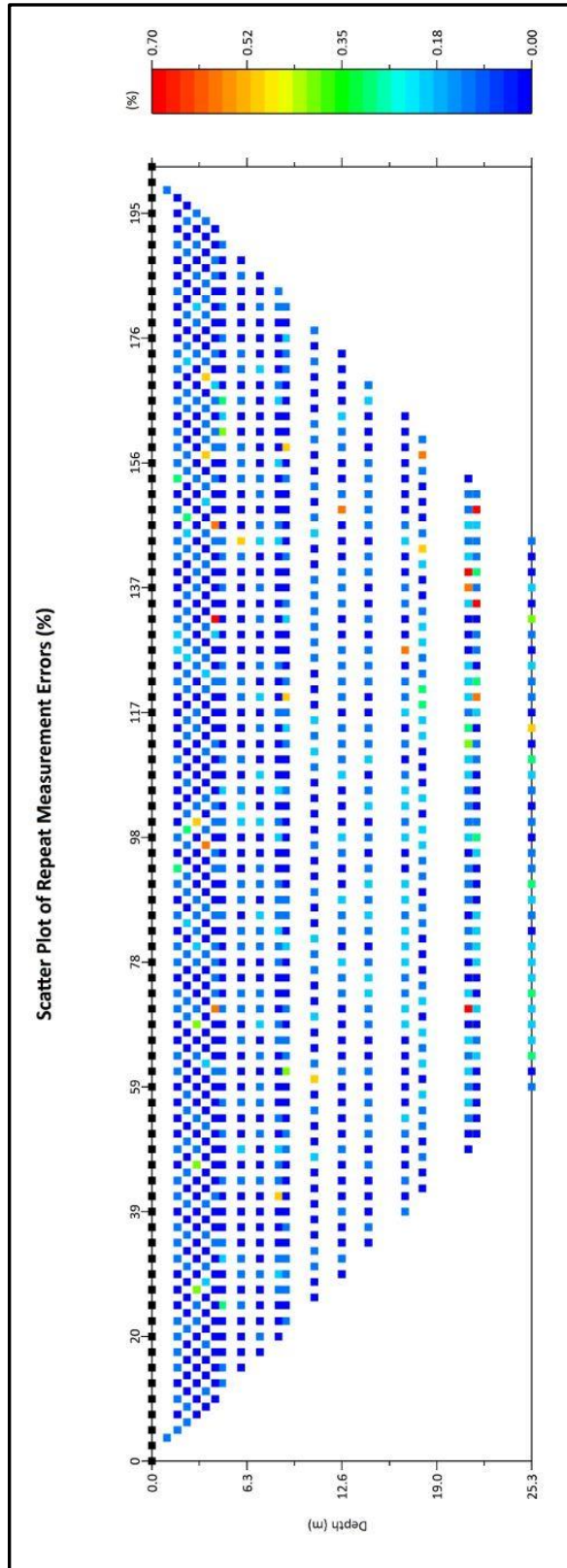


Figure 4.5.1 Line 3 – scatter plot of repeat measurement errors (%)

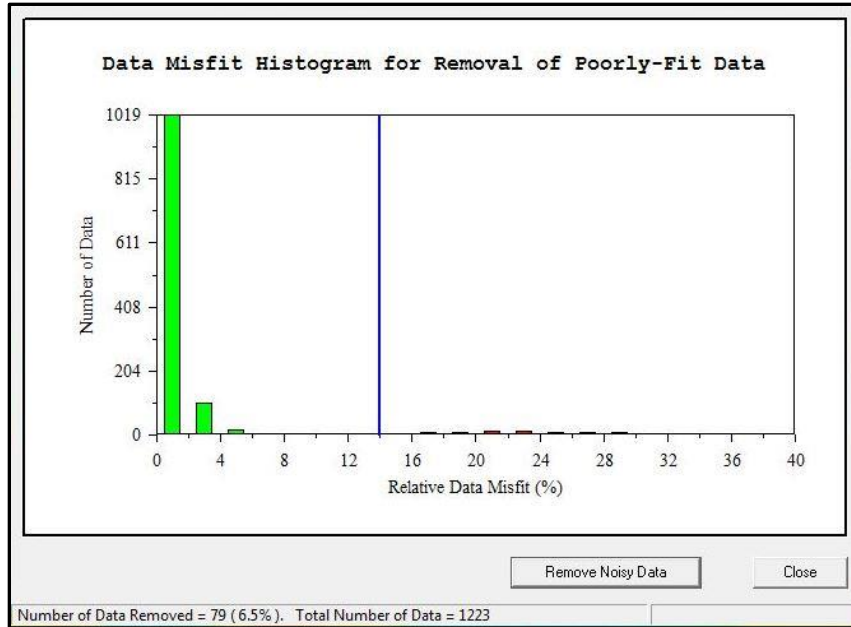


Figure 4.5.2 Line 3 – data misfit histogram for removal of poorly-fit data

All identified data misfits were removed from the Line 3 dataset. Figure 4.5.2 above shows that a very low percentage of data points needed to be removed. The total number of data points above is 1,223, where the software quality control measure suggested the removal of 79 data points, giving a total of 6.5 percent total removal. This range also falls well within the manufacturer- suggested range of 10 percent or less. Following the removal of the data misfits, the Line 3 dataset was inverted again to ensure that the data quality of the apparent resistivity section was optimized.

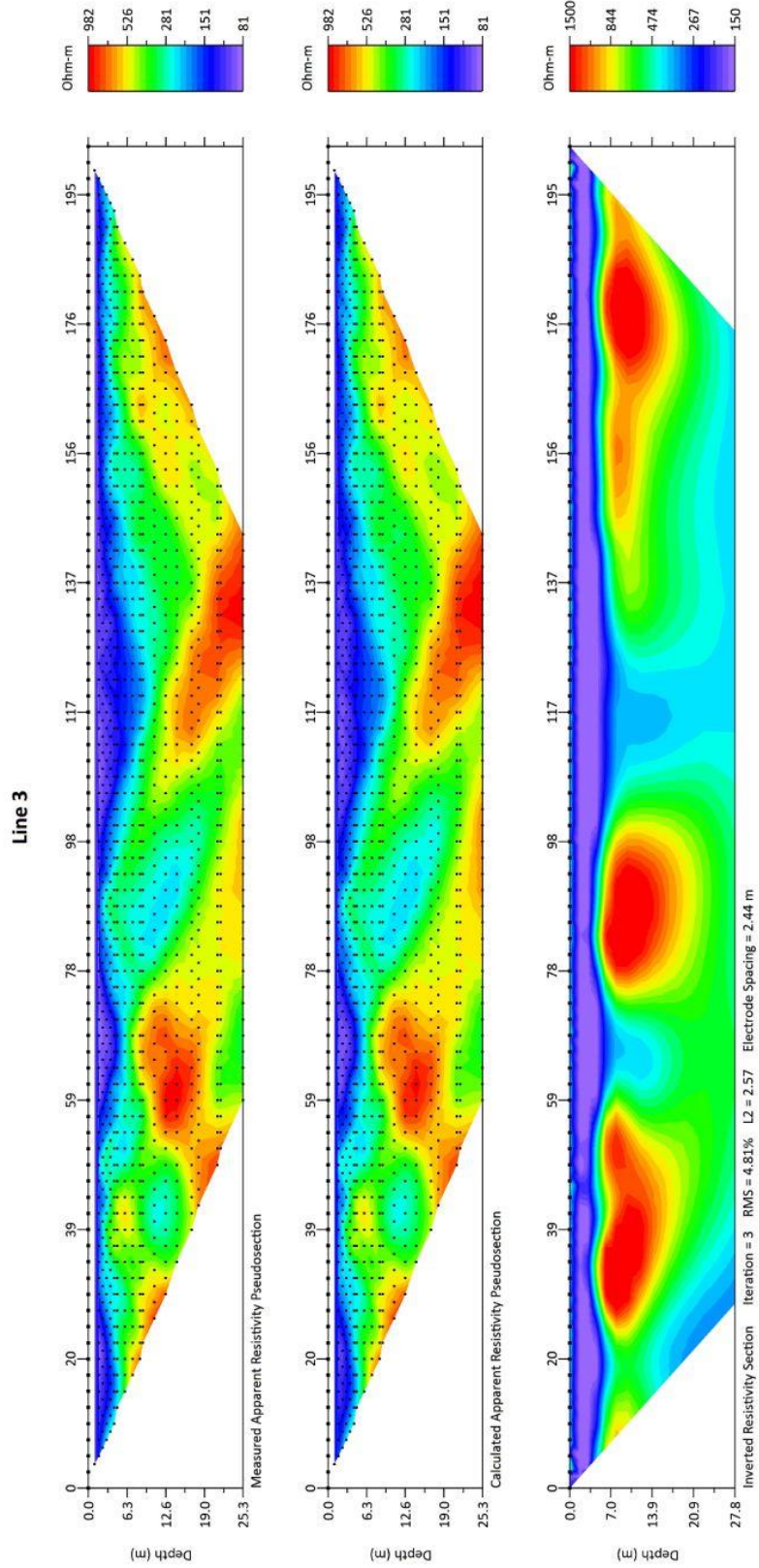


Figure 4.5.3 Line 3 – measured/calculated pseudo sections and inverted resistivity section

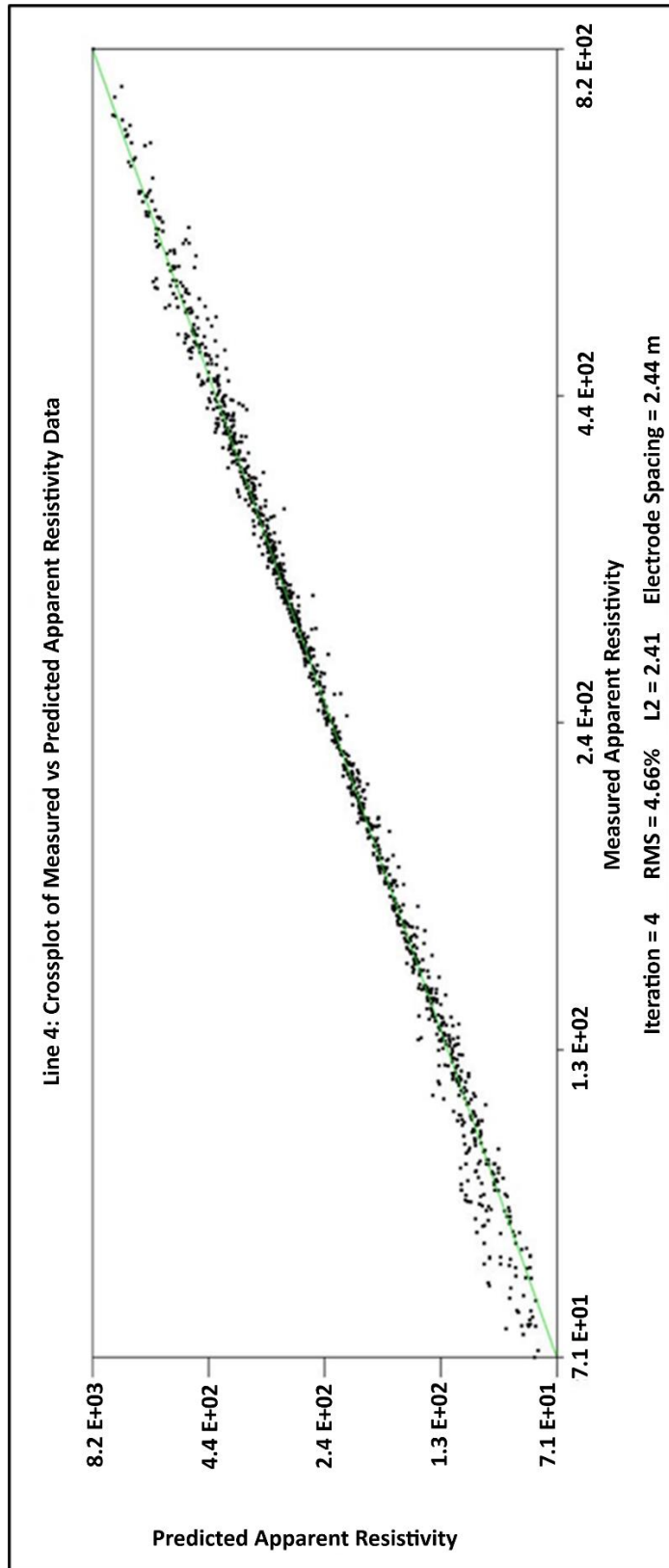


Figure 4.6 Line 4 – cross plot of measured vs. predicted apparent resistivity

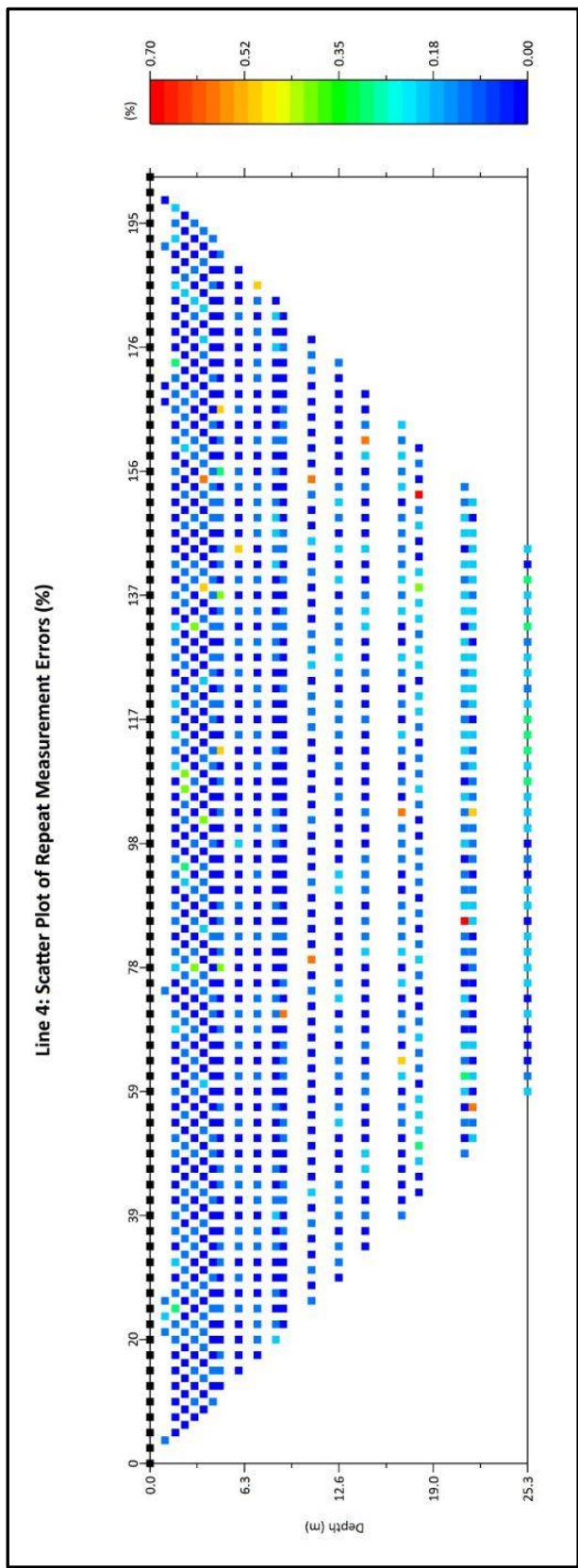


Figure 4.6.1 Line 4 – scatter plot of repeat measurement errors (%)

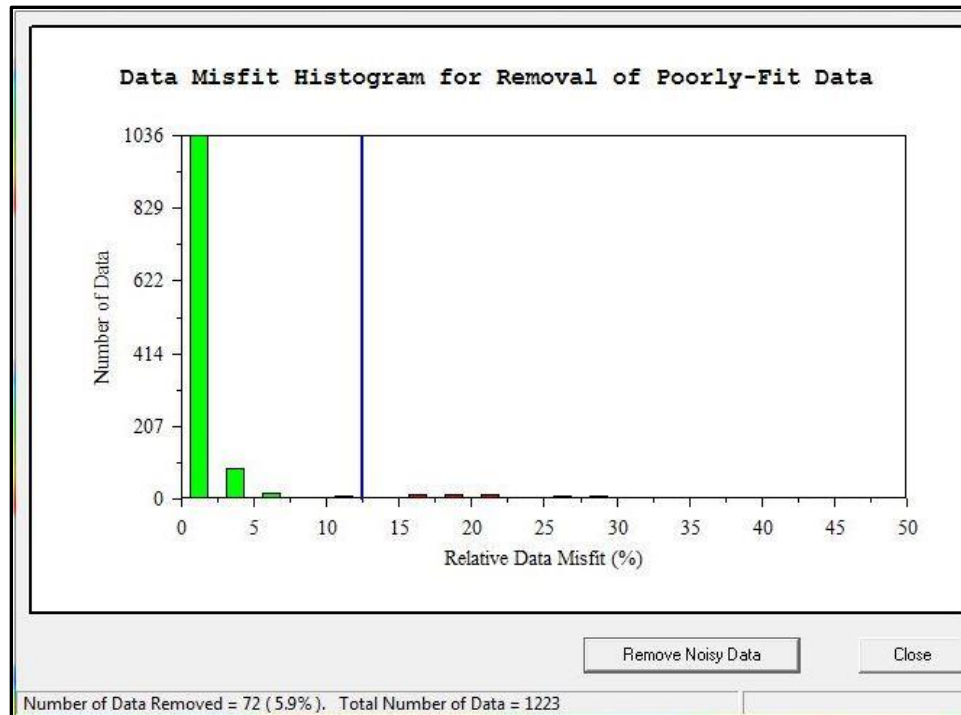


Figure 4.6.2 Line 4 – data misfit histogram for removal of poorly-fit data

All identified data misfits were removed from the Line 4 dataset. Figure 4.6.2 above shows that a very low percentage of data points needed to be removed. The total number of data points above is 1,223, where the software quality control measure suggested the removal of 72 data points, giving a total of 5.9 percent total removal. This range also falls well within the manufacturer- suggested range of 10 percent or less. Following the removal of the data misfits, the Line 4 dataset was inverted again to ensure that the data quality of the apparent resistivity section was optimized.

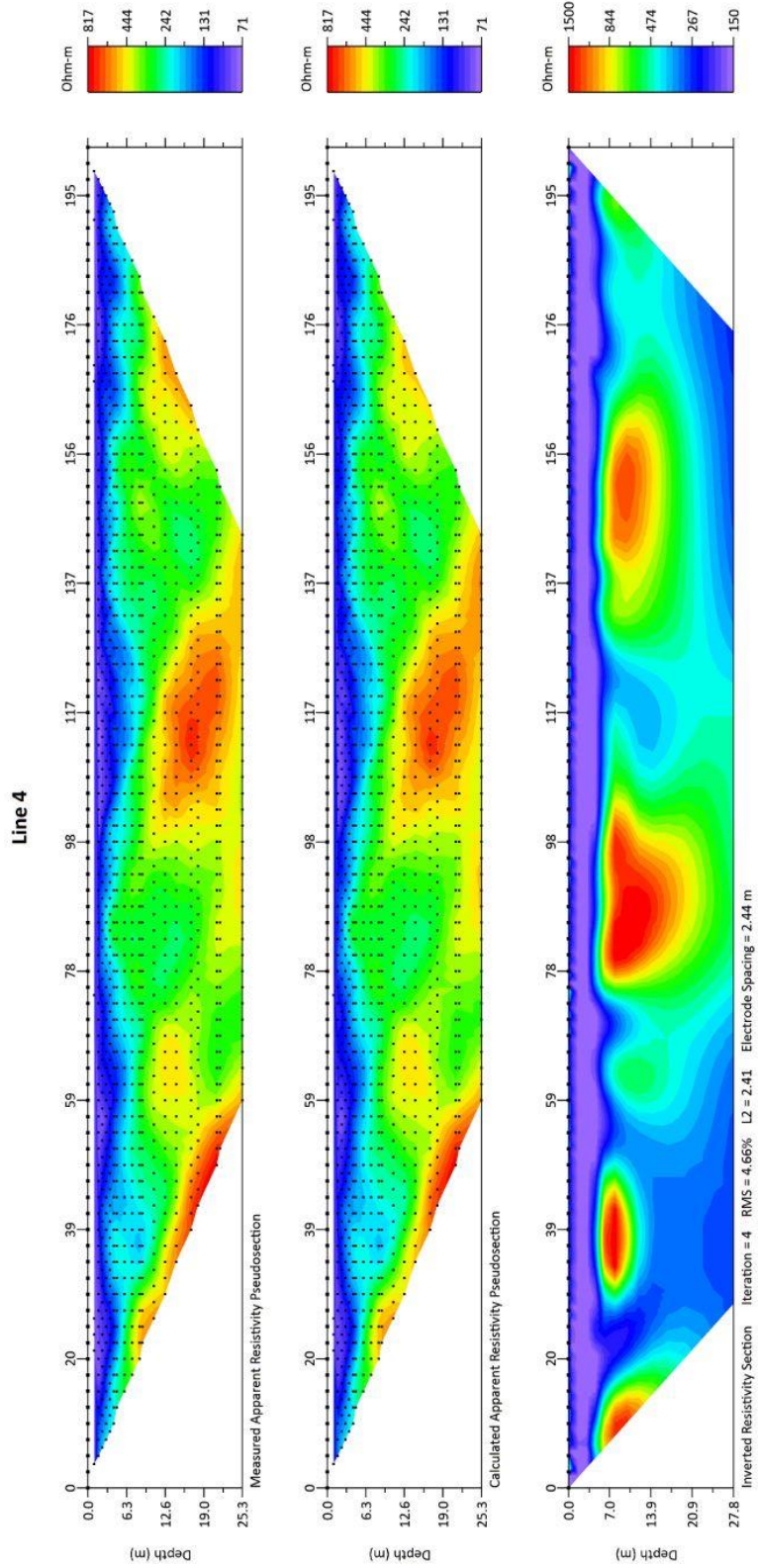


Figure 4.6.3 Line 4 – measured/calculated pseudo sections and inverted resistivity section

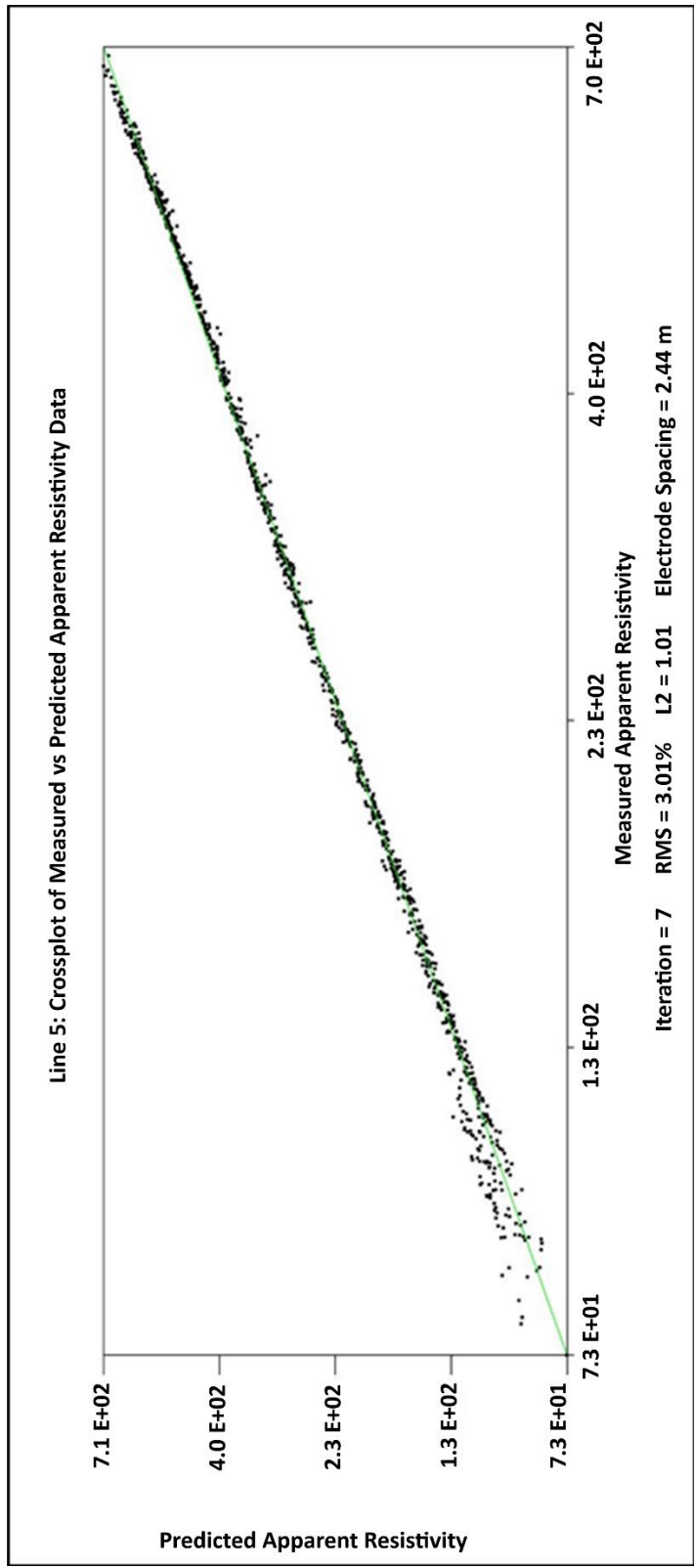


Figure 4.7 Line 5 – cross plot of measured vs. predicted apparent resistivity

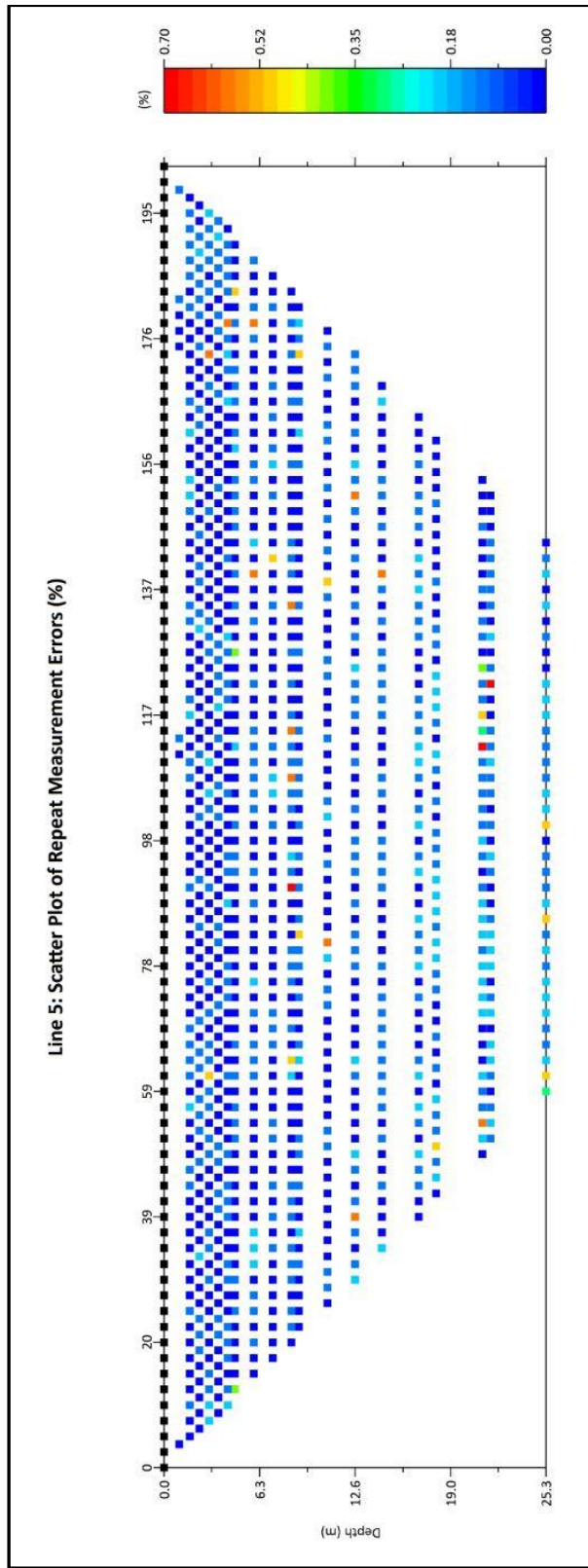


Figure 4.7.1 Line 5 – scatter plot of repeat measurement errors (%)

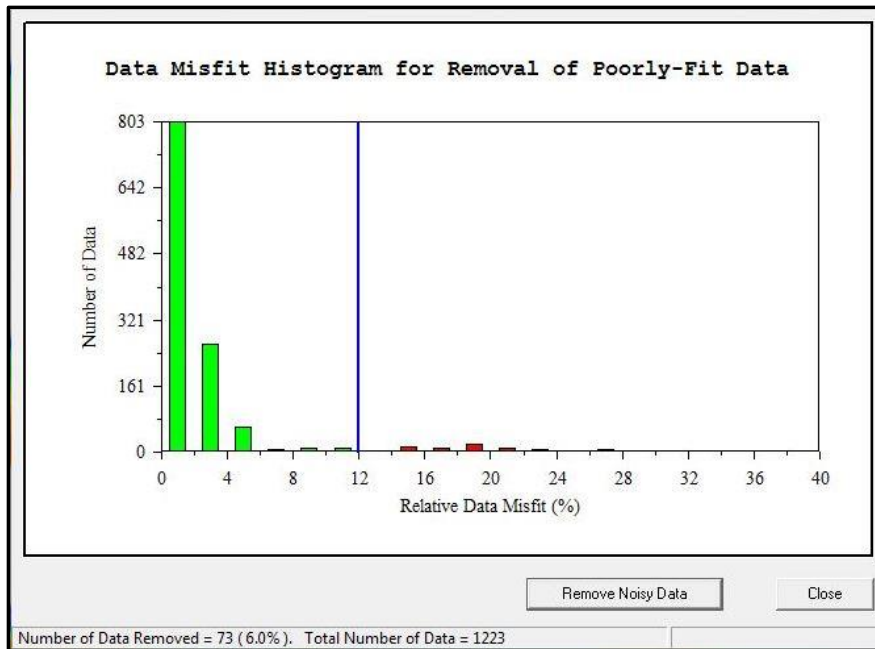


Figure 4.7.2 Line 5 – data misfit histogram for removal of poorly-fit data

All identified data misfits were removed from the Line 3 dataset. Figure 4.7.2 above shows that a very low percentage of data points needed to be removed. The total number of data points above is 1,223, where the software quality control measure suggested the removal of 73 data points, giving a total of 6.0 percent total removal. This range also falls well within the manufacturer- suggested range of 10 percent or less. Following the removal of the data misfits, the Line 5 dataset was inverted again to ensure that the data quality of the apparent resistivity section was optimized.

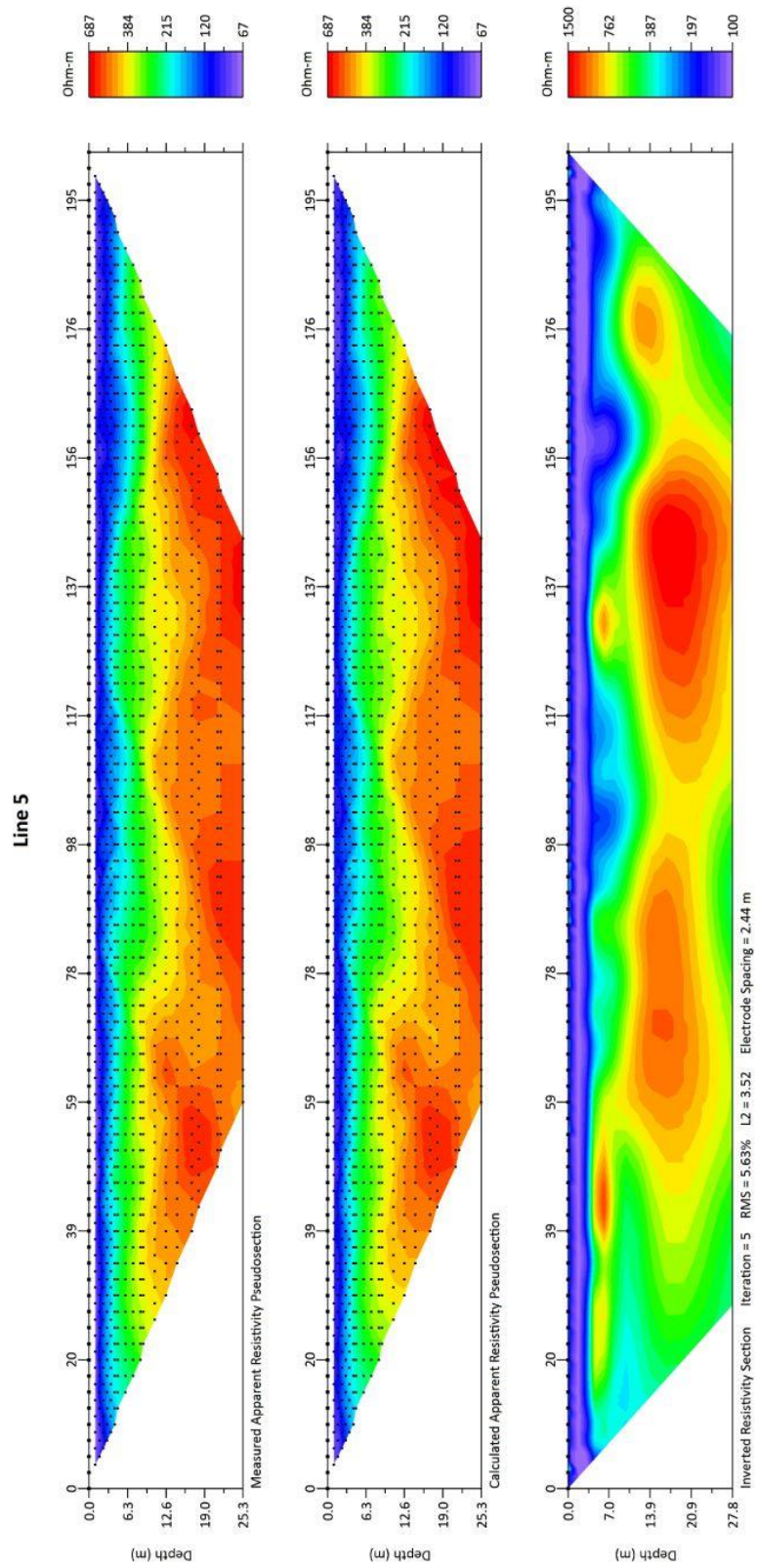


Figure 4.7.3 Line 5 – measured/calculated pseudo sections and inverted resistivity

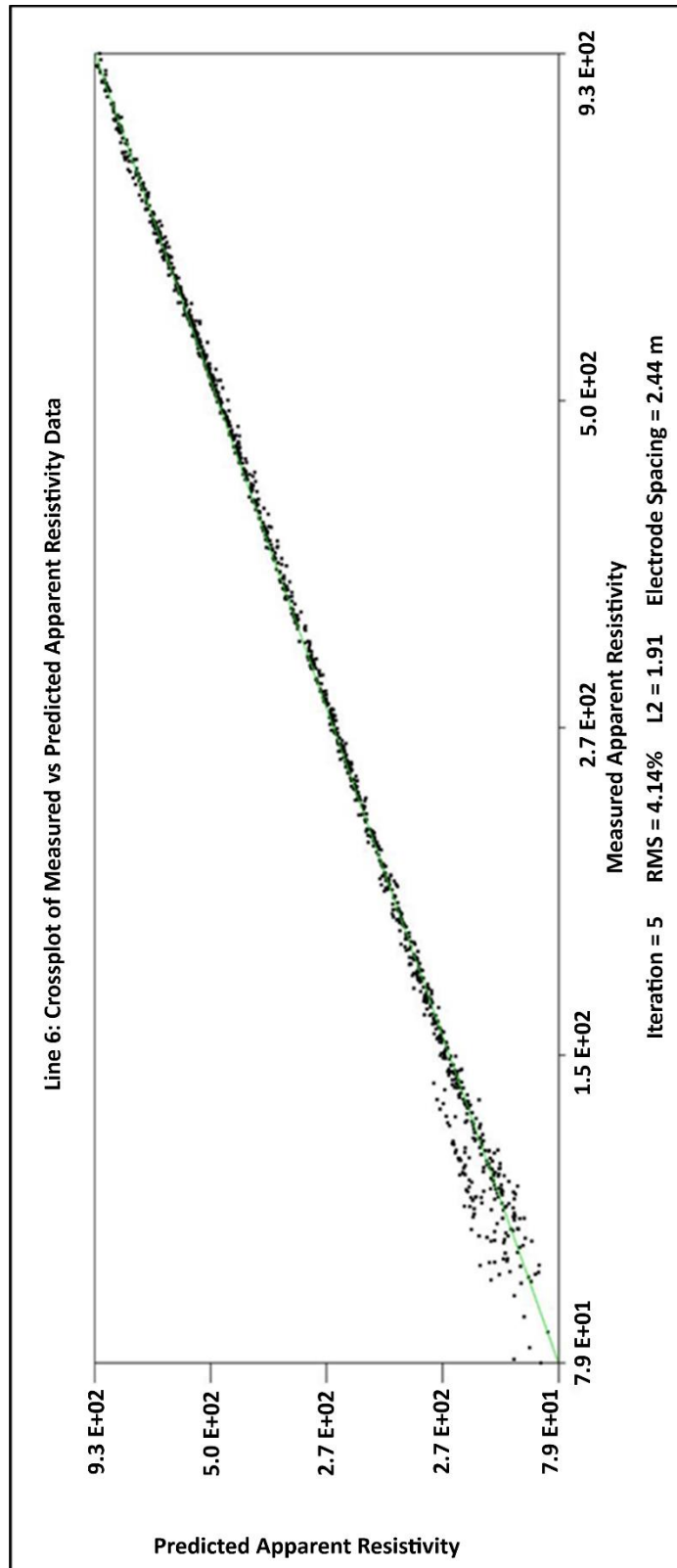


Figure 4.8 Line 6 – cross plot of measured vs. predicted apparent resistivity

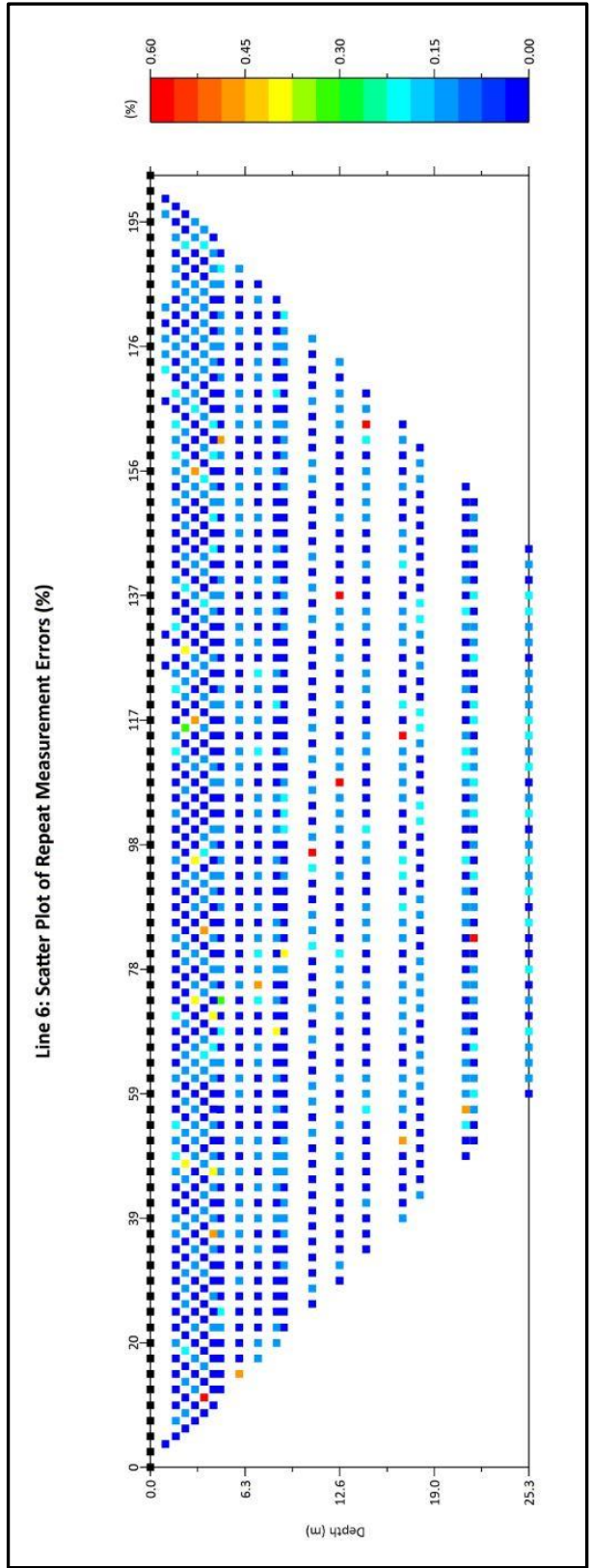


Figure 4.8.1 Line 6 – scatter plot of repeat measurement errors (%)

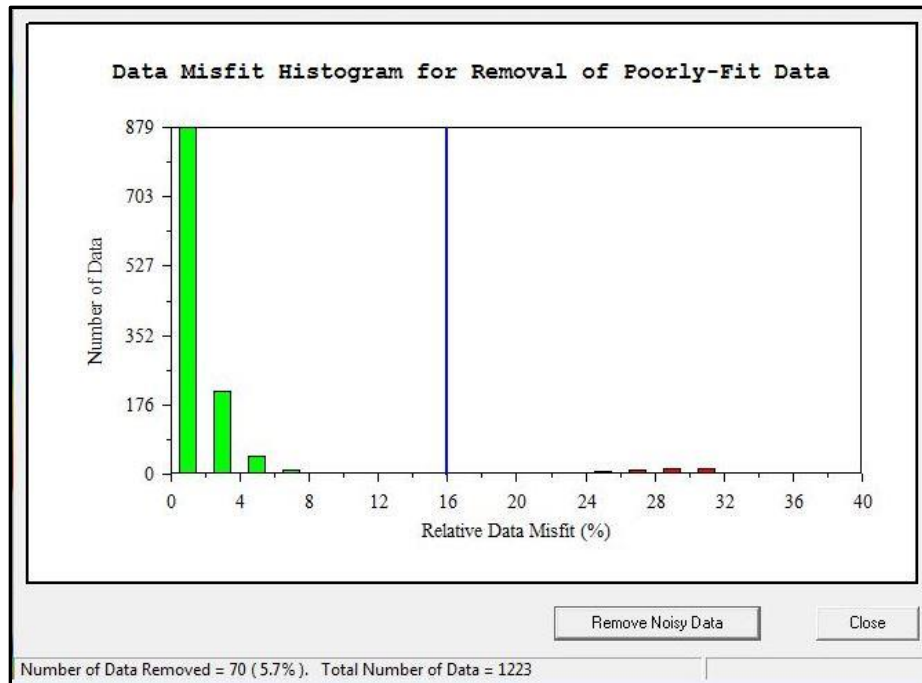


Figure 4.8.2 Line 6 – data misfit histogram for removal of poorly-fit data

All identified data misfits were removed from the Line 3 dataset. Figure 4.8.2 above shows that a very low percentage of data points needed to be removed. The total number of data points above is 1,223, where the software quality control measure suggested the removal of 70 data points, giving a total of 5.7 percent total removal. This range also falls well within the manufacturer-suggested range of 10 percent or less. Following the removal of the data misfits, the Line 6 dataset was inverted again to ensure that the data quality of the apparent resistivity section was optimized.

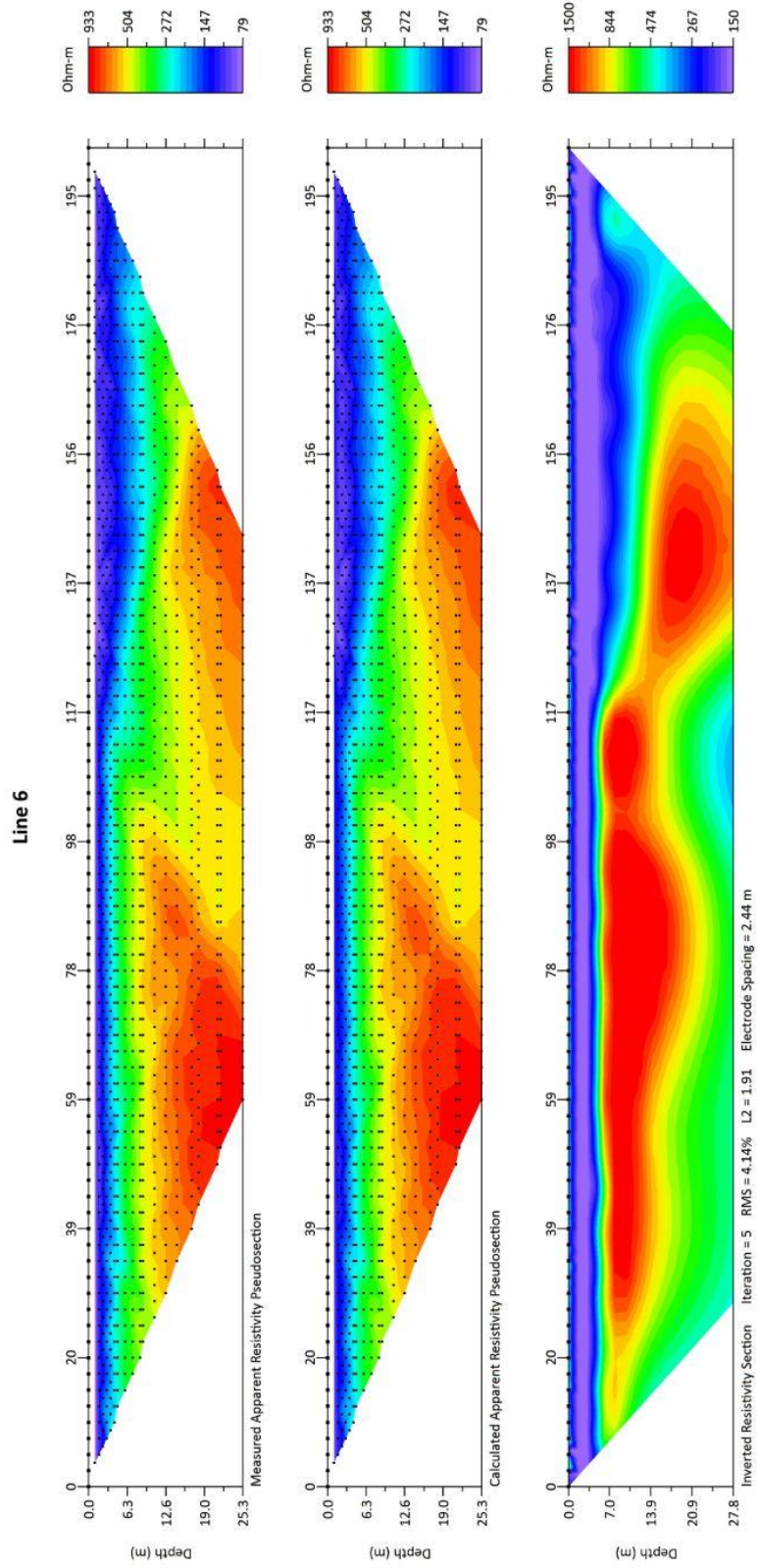


Figure 4.8.3 Line 6 – measured/calculated pseudo sections and inverted resistivity

4.7 Borehole Geophysical Survey Design

The borehole geophysical survey for this research was designed to best characterize bedrock wells MW-17 and MW-19. The suite of logs selected was chosen to best provide structural data of bedding planes, fractures, fracture density, lithologic variation, vertical flow characteristics of groundwater, and to identify potential water-producing or water-receiving zones. It should be noted that previous log data from MW-18, MW-20, and RW-3 were obtained for this research, as discussed in Chapter Three, and only included structural results from the optical televiewer data. The additional measurements added to this survey were to obtain a further understanding of the subsurface characteristics. It was not possible to re-log MW-18 or MW-20, as each well was abandoned and filled with concrete prior to commencing this research. Additionally, RW-3 is an active recovery well and was inaccessible for this research.

4.8 Borehole Geophysical Survey Setup

The logging procedures conducted at the research site followed industry standard downhole protocol for similar geophysical investigations. Each instrument was attached to a cable head at the end of a 4-conductor wireline. The “zero” depth of each probe was established at the appropriate benchmark (ground surface), and the recording mode of operation was initiated. The optical televiewer probe was lowered down the well via generator-powered winch at approximately 1 m/minute, the multi-parameter resistivity probe was lowered at approximately 3 m/minute, and the caliper was hoisted up the well at a rate of approximately 4 m/minute. The heat pulse flowmeter was lowered to

predetermined positions that were typically above and below notable fractures identified in the field with the OPTV and caliper probes. The recording mode was terminated when the probe touched the bottom of the wells. Up-log sections were also completed to ensure that geophysical responses were accurate, repeating, and within a close depth tolerance to the down log. Due to the mechanical nature of the caliper log, only up-log sections were collected with this tool.



Figure 4.9 Site photo showing OPTV probe and MW-19 (original).

4.9 Borehole Geophysical Data Processing Considerations

Following the collection of all measurements in the field, all borehole data were downloaded and processed in WellCAD – a commercially available software package designed for processing well log data (WellCAD, 2019). Specific processing practices applied to this data are described below. Note that the multi-parameter resistivity probe has seven measurements combined within a single probe, where specific processing considerations for each measurement are further described.

Optical Televiewer Probe

As discussed in chapter three, the optical televiewer is a magnetically oriented, 360-degree image of the borehole wall. Sinusoidal features which appear on the logs are through-hole features, meaning that the imaged feature spans across the entire borehole wall. As Apel et al. (2017) demonstrate in the below figure, an angular planar feature crossing through a given point along a cylinder can be plotted as a sine curve. Because the optical televiewer is oriented to magnetic north, the dip direction and dip angles of identified through-hole features can be measured. This is the key concept behind the structural analysis of bedding features and fractures.

After identifying through-hole features, each feature then undergoes a curve-matching process whereby a horizontal line is manipulated so that it matches the sinusoidal characteristic of a given borehole feature. The end result of the curve-matching process provides depth, strike, and apparent dip direction and dip angles of a given feature for further analysis and interpretation. Open fractures typically appear as dark colored sine

curves and can be compared to caliper data for further characterization. In-filled fractures or bedding features typically have a lighter color characteristic and an associated little-to-no deviation response on the caliper log. Processing and interpretation considerations also relate to fracture aperture. Broader, sinusoidal responses related to fractures are considered more significant, and the difference in depth between the top and bottom of each broad fracture can provide approximate apertures of identified significant fractures. It should be noted that the finer the fracture is, the more difficult it is to obtain aperture measurements and it is a function of resolution.

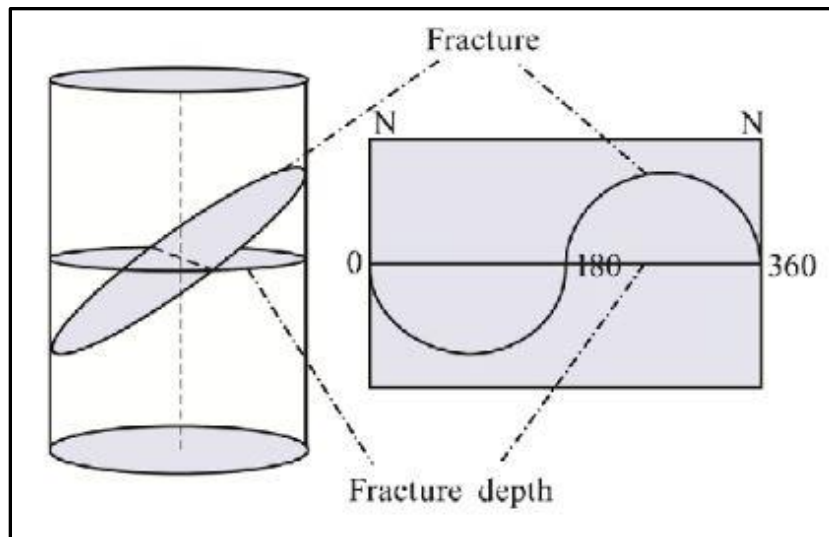


Figure 4.9.1 Planar fracture sinusoidal trace (Apel et al., 2017).

Caliper Probe

The primary processing considerations for the caliper probe are scale and orientation of fractures. Typically, the scale is set such that the center of the log represents the center of the borehole. For example, the 6-inch wells logged in this research were 6 inches in diameter, and the scale was set with a range of 5.5 to 10 inches (or 14-25 cm). This allowed for the visualization of both small- and large-scale fractures and general deviations in borehole diameter that stem from voids and small scale vugs.

Another important consideration is the mechanical nature of this probe versus the orientation of encountered fractures. For example, a significant near vertical fracture with a large apparent aperture as observed on the optical televiewer log (such as observed in MW-19) may appear to have less measured variation in borehole diameter than in reality. This is a result of a combination of the positioning of the three-arms on the caliper and the vertical nature of the fracture. This type of scenario will not produce sharp, peak responses, but rather longer, less pronounced variations on the caliper curve.

Multi-parameter Resistivity Probe

As with the caliper log, the primary processing procedures for the gamma, resistivity (8, 16, 32, and 64-inch normal), fluid resistivity, and temperature logs are to consider a reasonable scale for the obtained data. Refined scales were applied to each log respectively to best show data responses and ultimately allows for more accurate interpretations of the geophysical response.

Gamma Ray Probe

An additional processing procedure applied to the log data obtained from this probe is the filtering process. This process is completed on logs to best show realistic responses of the data. For example, the radioactive processes associated with the gamma measurement are subject to statistical variation, and the curve should not appear smooth. If needed, a running average filter can be set (typically a 2 or 3-point running filter) and is based on the gamma measurement with respect to depth. This filtering process can be useful to more accurately display the data responses of this curve, where a somewhat jagged characteristic is more realistic than a smooth curve. Similarly, running filters can be applied to allow for more or less variation in given responses for all curves to best show log responses. This process is typically trial and error.

Heat Pulse Flowmeter Probe

Because the calculated flow rate for this measurement is based on the distance that the heat pulse travels over time, the primary consideration is based on pick times, as earlier arrival times are equal to greater flow. Two examples are depicted below to best show how the heat pulse data times are selected. Time is shown on the x-axis, and vertical flow rates are shown on the y-axis. Upward flow is indicated above the horizontal and is represented by positive values. Conversely, downward flow is indicated below the horizontal and is represented by negative values. Pick times are selected at the inflection point along the curve.

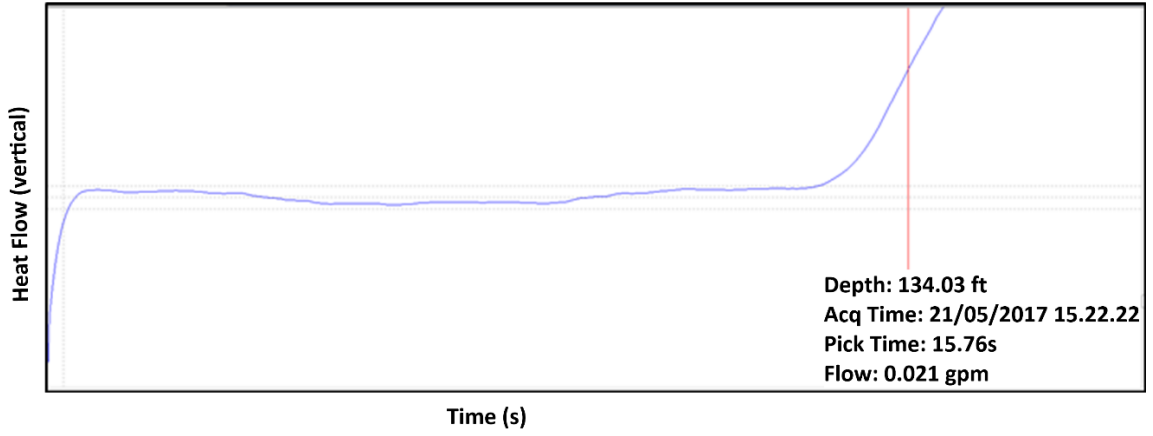


Figure 4.9.2 Pick time of upward flow within MW-17

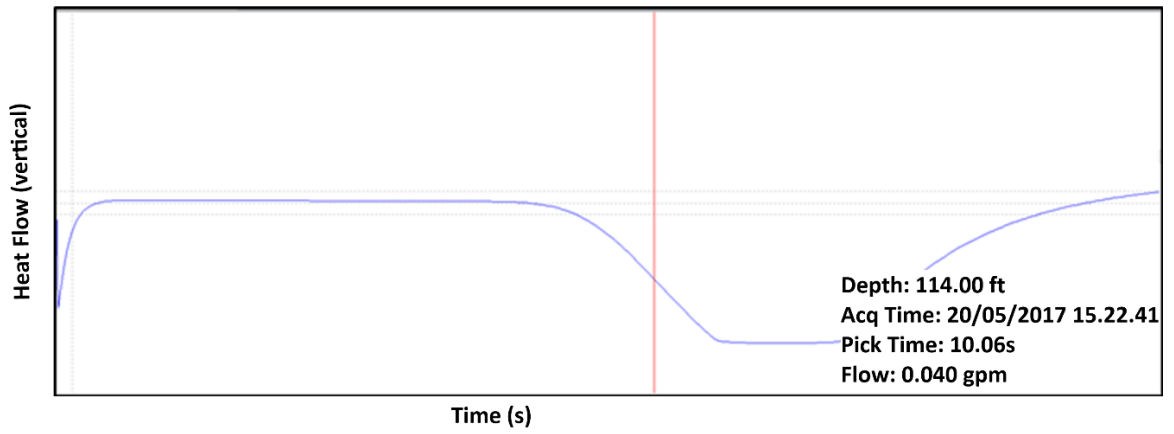


Figure 4.9.3 Pick time of downward flow in MW-19

CHAPTER 5

ANTICIPATED RESULTS

5.0 Forward Modelling of Electrical Resistivity Imaging Data

Prior geologic and hydrogeologic data allowed for a desktop feasibility study prior to conducting the field effort for the ERI survey. Based on this prior data and site conceptual models, anticipated electrical resistivity conditions at the site can be determined (typically average values of assumed materials are used if the range is large). After determining the likely resistivity conditions at the site, true resistivity values are assigned and modeled; this is known as a Forward Model. A Forward Model is a modeled set of resistivity values that are anticipated in the field and derived from an anticipated set of subsurface conditions. The data are then processed and analyzed in the same anticipated way as the actual dataset, where the result of the processing (as described in Chapter Three) is an inverse model and synthetic resistivity image. This process gives a realistic idea about the best obtainable results that may be encountered in the field. It should be noted that the synthetic model will not always match the true resistivity model and is based on site conceptual models.

The Earth Imager software by AGI used in this project allowed for a complete desktop feasibility study through the Survey Planner. The survey planner accounts for factors such as electrode spacing, survey geometry, and realistic measurement errors to best model the likely real-world results of an actual survey. After all desired values are selected and input into the model, a comparison of the true resistivity model to the predicted

inversion results he can determine if the desired target or targets can be resolved using a given survey design.

The assumed resistivity values used in the forward models below were derived from geologic logs completed during the installation of bedrock monitor wells. The factors that were accounted for were the overburden thickness of approximately 5 m, a limestone and dolomitic geologic setting, the presence of LNAPL with a thickness of approximately 3 m in the rock matrix, potential air or water-filled cavities, approximate depth to the water table, and both saturated and unsaturated rock. Additionally, resolution was greatly emphasized in the models, as attempting a deeper study would lessen resolution above the water table. Because LNAPL contamination is less dense than water, it will typically settle at the water table. For the purposes of this research in attempting to better understand LNAPL migrations at the research site, this is an extremely important factor when completing a survey design and in the generation of a forward model. Because dipole-dipole array geometry loses resolution with depth, the survey was designed to collect data just below the water table to retain resolution and anticipated targets.

Three Forward Models (Forward Model 1, Forward Model 2, and Forward Model 3) below were generated with predetermined 2.4 m (8 foot) electrode spacing, dipole-dipole array geometry, 5% measurement error, and relative resistivity values for anticipated overburden, unsaturated dolomite, dolomite, and structural features that fall within those respective zones. Specifically, Forward Model shows the anticipated result of the thrust fault at the overburden-bedrock interface, Forward Model 2 shows a shallow saturated void

adjacent to the thrust fault, and Forward Model 3 shows an LNAPL just above the water table with an assumed thickness. The forward models are described below in greater detail.

Forward Model 1 depicts clay layer as a very low resistivity zone, where the range is approximately 50 Ω m to 200 Ω m and falls between the range of electrical resistivity values of common earth materials on Table 2.0 in Chapter Three. The unsaturated dolomite ranges from 1500 Ω m to 4087 Ω m, the saturated dolomite falls between 400 Ω m and 1500 Ω m. The thrust fault also is indicated as a low resistivity zone, as it is assumed to be a likely preferential pathway for fluid movement. Note that the shallower expression of the modeled thrust fault contains slightly higher resistivity values as it lay above the water table and is surrounded by the assumed unsaturated dolomite.

The range of values for the modeled thrust fault section, which separates the unsaturated high resistivity zones, is 400 Ω m to 500 Ω m. The range of values for the lower expression of the modeled thrust fault that falls below the water table was given very low resistivity values of approximately 50 Ω m. Model 1 below has been annotated showing the underlying assumptions made prior to constructing the model. Note that the thrust fault was placed in the anticipated portion of the resistivity section where the fault zone falls along the anticipated ERI Line 1. This was intentionally modeled in this manner to view lateral resolution limitations of the fault zone should it fall near the spread edges of a profile in the field. See the results of Forward Model 1 below.

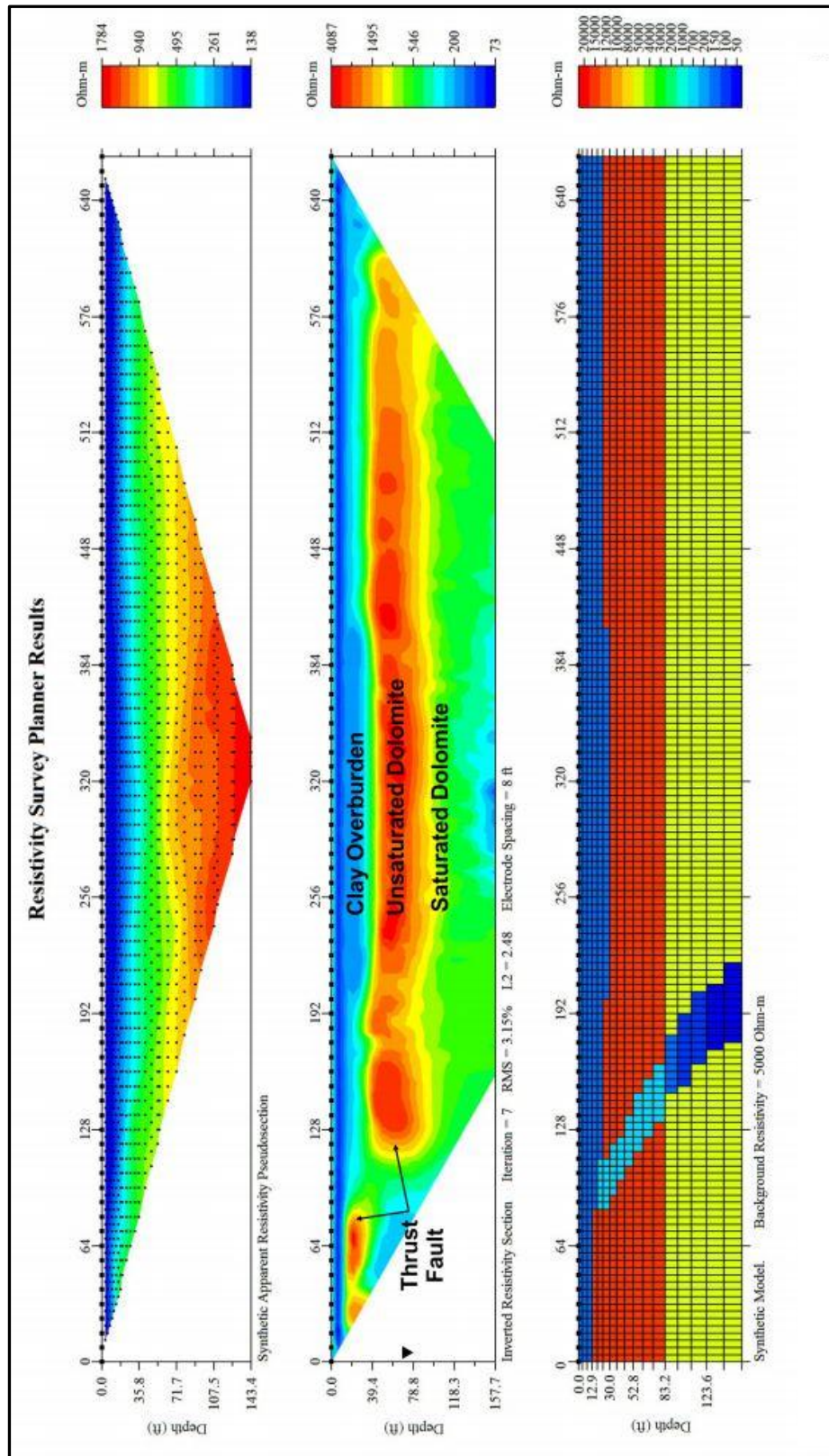


Figure 5.0 Forward Model 1

Forward Model 2 used the same underlying assumptions as Forward Model 1 in terms of the distribution of resistivity values for clay layers, unsaturated dolomite, saturated dolomite, and the thrust fault. This model was constructed to observe responses of shallow, saturated voids that may be present within the study area. The site background data indicated that karst features such as air and water-filled voids and small-scale solution cavities have been identified elsewhere within the industrial complex. The assumption in this model is that the shallow, saturated void would be expressed as localized and discrete very low resistivity response, and was assigned a value of 50 Ω m.

One important note is that the number of data points near the surface is greatest and provides the best resolution of this type of near surface feature. The distribution of data points is best observed on the synthetic apparent resistivity model, which shows the distribution of data points as small black dots. Moreover, the synthetic model showing the distributions of interpreted features further defines the data distribution, where the model depicts the loss of resolution with increasing squares.

Another important observation from Model 2 is the apparent effect the saturated void has on the expression of the fault zone. Note how the dispersion of low resistivity values is much greater than observed in Forward Model 1. Although the same iteration number (number 7) was used and similar RMS error values were observed as on Forward Model 1, the greater distribution of low resistivity values may be a result of over processing the model. See the results for Forward Model 2 below.

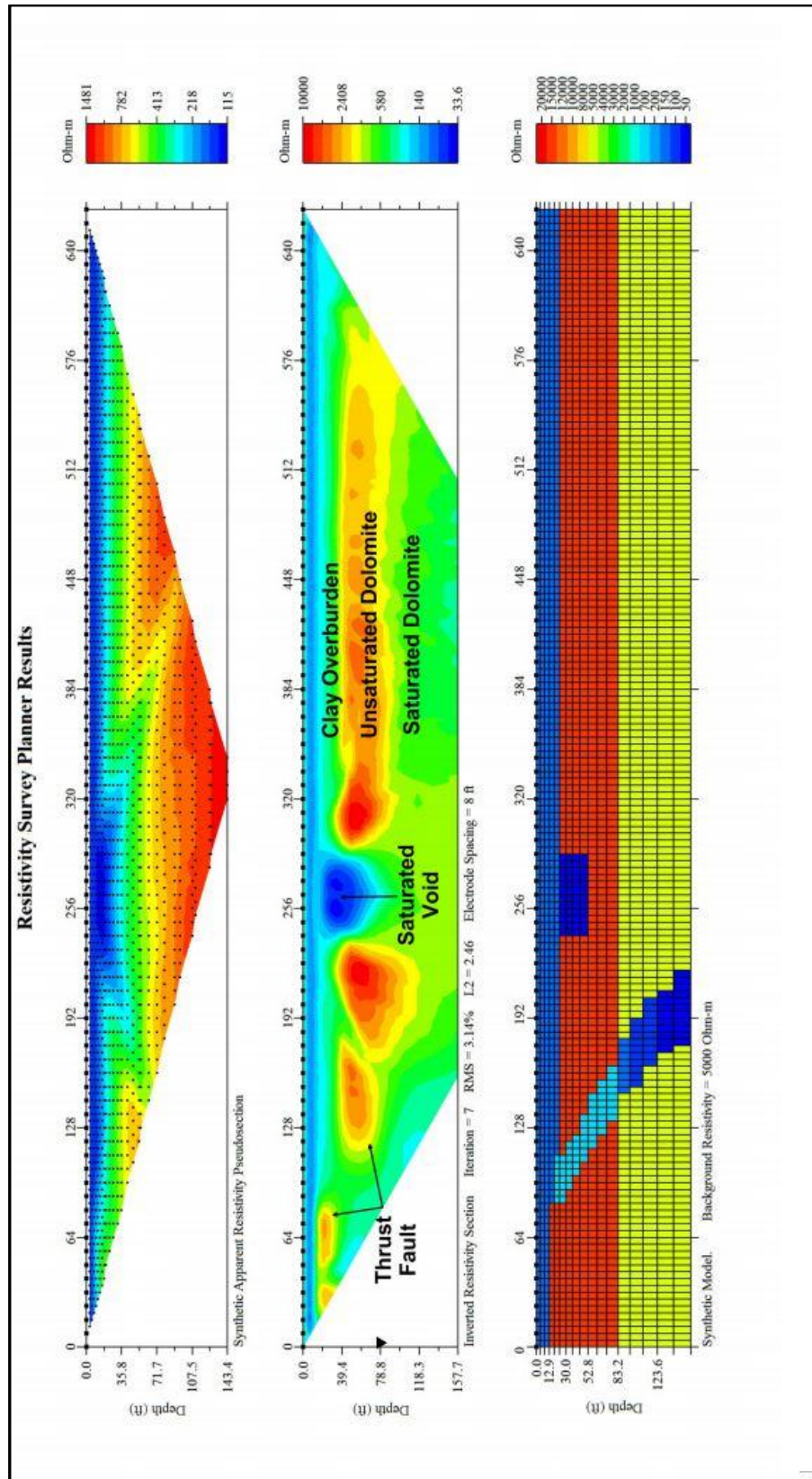


Figure 5.1 Forward Model 2

Forward Model 3 used the same resistivity values for clay, unsaturated dolomite, and saturated dolomite. The addition to this forward model was the presence of an approximately 3 m thick layer of assumed LNAPL located just above the water table and contained within the rock matrix. The annotations for the clay layer, unsaturated dolomite, saturated dolomite, and thrust fault have been removed to best show the modeled response of the LNAPL thickness at the anticipated depth. LNAPLs historically have a high resistivity characteristic, but this characteristic is completely dependent on surrounding material. Electrical resistivity responses are a bulk measure response, meaning that the electrical resistive value obtained is a measure of all of the given material within the measured area. Forward Model 3 was constructed to gain a better perspective on the feasibility of the dipole-dipole method to detect a significantly thick layer of LNAPL at the anticipated depth. In this model, the resistivity value of the LNAPL layer was assumed to be 1700 Ω m, or just slightly higher than the surrounding material. As indicated below in Forward Model 3 below, the modeled LNAP plume is not clearly defined on the inverted model. It was determined during this stage that a direct detection of the LNAPL plume would not be feasible based on the assumed parameters which were obtained from all available prior site data. However, based on the successful application of the model constraints applied to Forward Model 1 and Forward Model 2 to depict anticipated structural features, (e.g. thrust fault and water-fill voids) the method was deemed feasible to determine possible preferential pathways for both groundwater movement and, therefore, plume migration from the source.

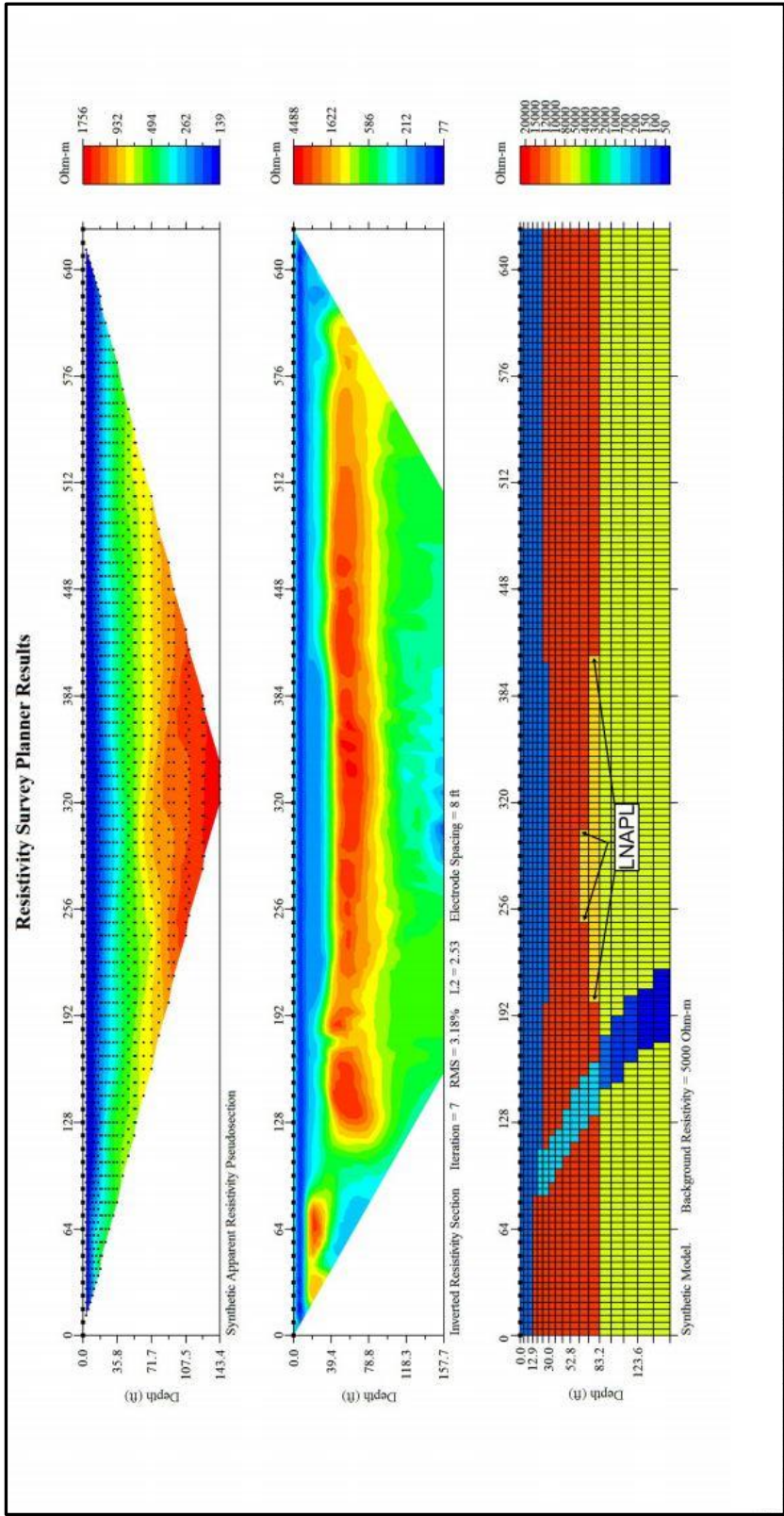


Figure 5.2 Forward Model 3

5.1 Anticipated Structural Responses Based On Previous OPTV Data

Because of the abundance of prior downhole geophysical data throughout the site described in detail in Chapter Three, the general structural responses from the previous OPTV data were anticipated to be highly similar. To review the ENSR (2005) data, of the 46 bedrock wells that were logged, a general trend for bedding strike was to the northeast, with a range of N10°E to N40°E, with the exception of an apparent small-scale trend in strike direction with the orientations in an easterly direction between N75°E and N90°E. The fracture analysis of all identified fracture planes shows a dominant fracture strike from N20°E to N40°E. The subordinate easterly trend in fracture strike direction is from N75°E to N90°E. The dominant dip direction of the observed fractures was to the southeast, where dip angles range from 30 degrees to 60 degrees, with an average of 44 degrees. Based on the abundant amount of previous data, MW-19 was anticipated to have similar structural characteristics.

CHAPTER 6

RESULTS

This chapter presents the results of the ERI survey and borehole geophysical investigation. Both annotated and unannotated ERI cross sections show resistivity interfaces and interpreted variations in lithology and structural geologic characteristics as they relate to measured ERI responses. Specific ERI interpretations are related to known geologic conditions obtained from geologic logs associated with nearby bedrock wells. Similarly, the downhole geophysical data from MW-17 and MW-19 are described in detail, followed by the annotated geophysical logs and data tables of structural data.

6.0 General Comparison of Forward Models to Modeled Resistivity Sections

In general, the predictions of Forward Model 1, Forward Model 2, and Forward Model 3 indicate that the distribution of resistivity responses throughout the subsurface were relatively similar to modeled sections. The forward models and modeled resistivity sections show a well-pronounced near surface resistivity boundary that likely represents the overburden-bedrock interface observed during the installation of MW-17 and MW-19. Both models clearly indicate variations in resistivity responses where the assumed saturated and unsaturated dolomite are present, and also that the upper expression of the fault zone would be expressed as a significantly low resistivity zone.

In this case, the modeled resistivity sections plainly define two zones of low resistivity that may be related to the upper expression of two distinct fault zones. Lastly, the distribution of resistivity values used in the forward models were relatively close for

the clay layer with a range of approximately 50 Ω m - 150 Ω m, 1000 Ω m to 1500 Ω m for the unsaturated dolomite, and 200 Ω m-1000 Ω m for saturated dolomite.

Although there is good correlation between the forward models and modeled sections, there are also significant differences. Greater variation occurs in the distribution of resistivity values throughout the cross-section from the modeled data, versus the relatively even distribution shown on the forward models; however, this was anticipated as the forward models were constructed in a simulated environment. One significant difference is in the abundance of smaller-scale possible fractures that are present on numerous cross-sections. Variations in bedrock topography were also more pronounced on the modeled sections and show a higher variability undulation occurs. This is particularly true as observed on Line 6, where clay thickness increases to approximately 10 m at the northeastern end of the transect.

Although variations do occur between the forward model and modeled sections, the differences are significant in the sense that preferential fluid movement is likely associated with the additional low resistivity zones identified on the modeled section. In addition, the forward model shows a much narrower near surface expression of the fault zone. In actuality, the two interpreted fault zones are likely broader with much greater variation from the surface expressions at depth. This difference is exceptionally useful in determining zones that may be more or less likely to act as preferential pathways for groundwater movement. Conversely, the greater variation in high resistivity units could indicate possible limitations on groundwater movement and the documented stagnant nature of the LNAPL plume movement to the east.

6.1 Electrical Resistivity Survey Results

Line 1

Line 1 dipole-dipole data were collected in a northwest-to-southeast fashion and is closest to the reported sources of contamination (Figure 7.0). Figure 6.0 shows a notable resistivity boundary containing low resistivity values was observed from 0 m to approximately 5.25 m, where the resistivity values range from 150 Ω m to 225 Ω m. Based on the resistivity responses and descriptions from geologic logs associated with nearby bedrock well installations, these responses likely derived from the clay and silty carbonate rock residuum (ENSR, 2005, p. 1-2). Variations in measured apparent thickness are minimal and within approximately 1 m to 1.5 m, suggesting little undulation.

The interpreted overburden-bedrock interface is well defined and uniform throughout the resistivity cross section. Bedrock resistivity values on Line 1 have a relatively broad range from approximately 475 Ω m to 1500 Ω m. Higher bedrock resistivity values are generally contained within the upper half of the cross section, with the greatest values measured near the overburden-bedrock interface. The high resistivity responses are likely related to more competent rock with low porewater content. Lower resistivity values with a range of 450 Ω m to 650 Ω m are primarily contained to the bottom half of the profile, or from approximately 14 m to a total depth (TD) of 27.8 m. Lower resistivity values are likely due to greater pore water content, especially nearer the groundwater table indicated on the profile.

The most notable features observed on the Line 1 resistivity cross section are two very low resistivity zones that extend vertically from the overburden-bedrock interface to the bottom of the profile. These two, well-pronounced, zones of very low resistivity have been interpreted as “Fault Zone 1” and “Fault Zone 2” (FZ-1 and FZ-2), respectively. Laterally along the Line 1 cross section, interpreted FZ-1 falls between 39 m and 56 m near the overburden -bedrock interface, and is a near- vertical feature that is roughly 17 m wide in the shallow subsurface, and widens gently with depth to 27.8 m, where the width is approximately 29.5 m. The resistivity values related to the FZ-1 structure are very low, and range from approximately 200 Ω m to 300 ohm-m.

Interpreted FZ-2 falls laterally along the line between 145 m and 149 m and also begins vertically at the overburden-bedrock interface. The resistivity values that define the FZ-2 structure range from 300 Ω m to 475 Ω m. The width of FZ-2 at the overburden-bedrock interface is roughly 4 m and is roughly vertical with a gentle apparent dip to the southeast along the profile. The near surface expression of this feature is much narrower than observed on FZ-1 but is still well pronounced within the data set. At a depth of approximately 14 m, FZ-2 widens to approximately 9 m; at this same point, the vertical expression of FZ-2 has an apparent change from vertical and becomes distributed more laterally to the southeast. At the base of FZ-2 near the interpreted water table, the lowest resistivity values of approximately 300 Ω m are present.

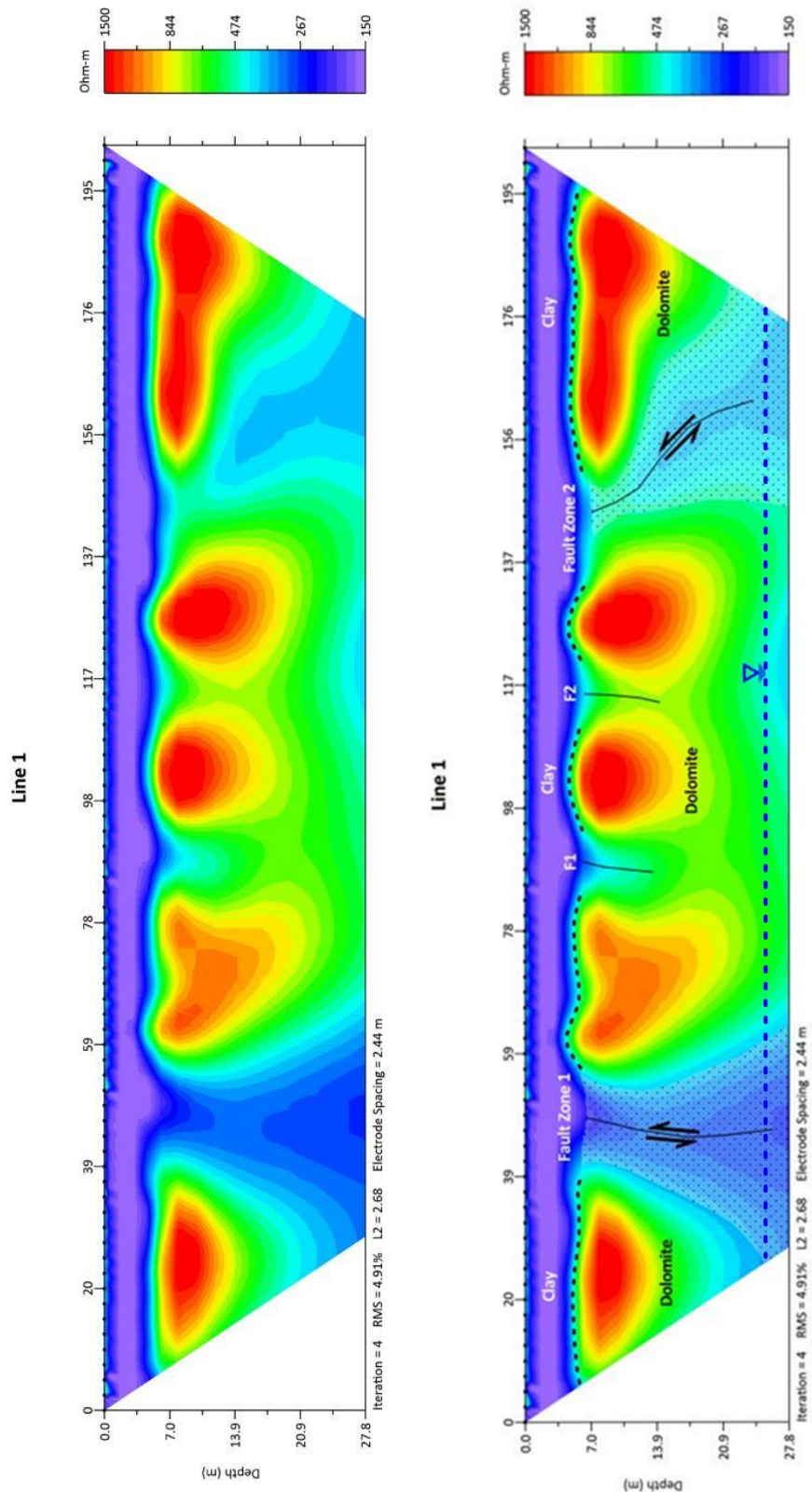


Figure 6.0 Line 1: Unannotated and annotated resistivity sections

Line 2

Dipole-dipole data were collected in a northwest-to-southeast fashion and was intentionally centered between recovery well RW-3 and recovery well RW-17 (Figure 7.0). Figure 6.1 shows a shallow, very low resistivity zone was observed and varies in depth from approximately 3.5 m to 6.5 m. Resistivity values within this zone range from 150 Ω m to 200 Ω m and are likely a result of overburden. Little undulation at the base of the clay unit is present, and a clear resistivity boundary separates clay from bedrock. Bedrock resistivity values range from 750 Ω m to 1500 Ω m, where greater values are typically at shallower depths near the overburden-bedrock interface, with the exception of a lobe containing higher resistivity values centered laterally at approximately 49 m to the base of the profile at 27.8 m and where the interpreted water table is at approximately 25 m. The most notable features on the Line 2 cross section are an apparent continuation of both FZ-1 and FZ-2 observed from ERI Line 1. Laterally along Line 2, FZ-1 falls approximately between 19 m and 25 m, has a low resistivity range between 250 Ω m and 400 Ω m, begins at the overburden-bed rock interface, and is present to the base of the profile to a depth of 27.8 m. In contrast to the FZ-1 on Line 1, this portion of FZ-1 on Line 2 is narrower near surface at approximately 6 m and has an apparent high dip angle to a depth of approximately 10 m, where the feature widens to approximately 20 m and becomes vertically oriented to the base of the profile. FZ-2 falls laterally along Line 2 between 135 m and 148 m and is a vertically oriented structural feature that is present from top of bedrock to the base of the profile. The vertical nature of this portion of FZ-2 on Line two contrasts with the observed apparent dip direction observed on FZ-2 on Line 1.

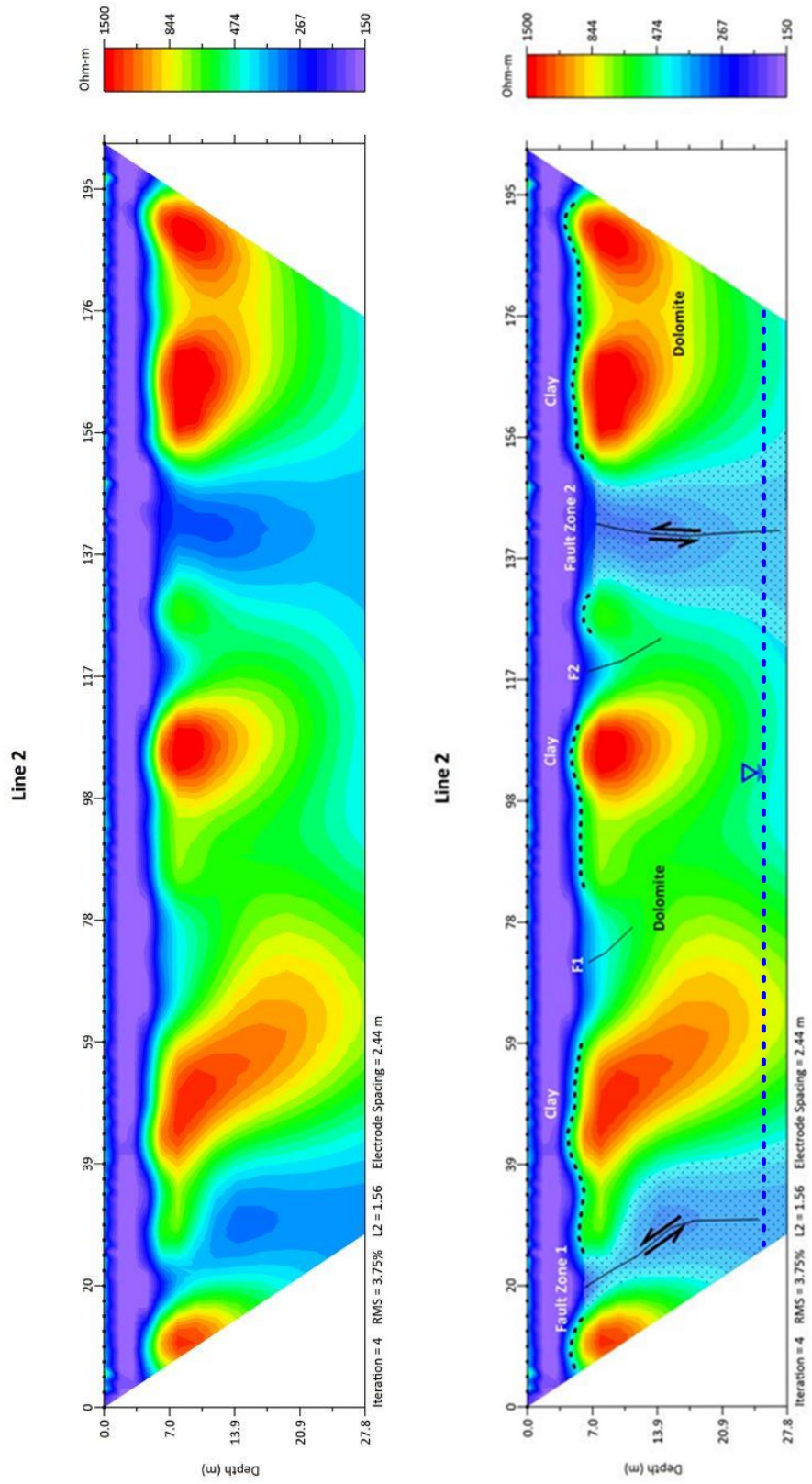


Figure 6.1 Line 2: Unannotated and annotated resistivity sections

Line 3

Line 3 dipole-dipole data were collected from northwest to southeast and is located outside the eastern extent of the documented LNAPL plume (Figure 7.0). Figure 6.2 shows a low resistivity zone from the ground surface to a variable depth between 3 m to 7 m was observed, where the resistivity values are very low with a range between 150 Ω m to 250 Ω m. This low resistivity zone continues to correlate with both the geologic logs and prior ERI lines (Line 1 and Line 2), suggesting that this zone is well defined on continuous to this point. Resistivity values continue to indicate a well-defined overburden-bedrock interface. Bedrock resistivity values range from 475 Ω m to 1500 Ω m. The greatest bedrock resistivity values are present at shallower depths. Bedrock resistivity values become less with depth; specifically, from 15 m to the base of the profile, where values are around 500 Ω m, with the exception of the low resistivity values related to FZ-1, FZ-2, and the interpreted water table at approximately 25 m. The most notable features on Line 3 are the two interpreted fault zones FZ-1 and FZ-2. FZ-1 appears on the very edge of the left side of the profile and falls laterally along Line 3 between 10 m to 22 m. FZ-1 appears to have similar structural characteristics as observed on Line 2, where the shallow expression of the faulted zone is more vertically oriented than the bottom $\frac{3}{4}$ of the profile, broadens with depth, and is apparently wider at the base. The width of the base of FZ-1 on Line three cannot be determined, as this zone extends beyond the profile to the north. FZ-2 is a well-pronounced, vertically oriented low resistivity zone that falls along Line 3 between 100 m and 125 m. The top of FZ-2 is at the bedrock interface and is roughly 20 m wide. FZ-2 appears to have a consistent width throughout the profile but slightly widens towards the base to approximately 21.5 m.

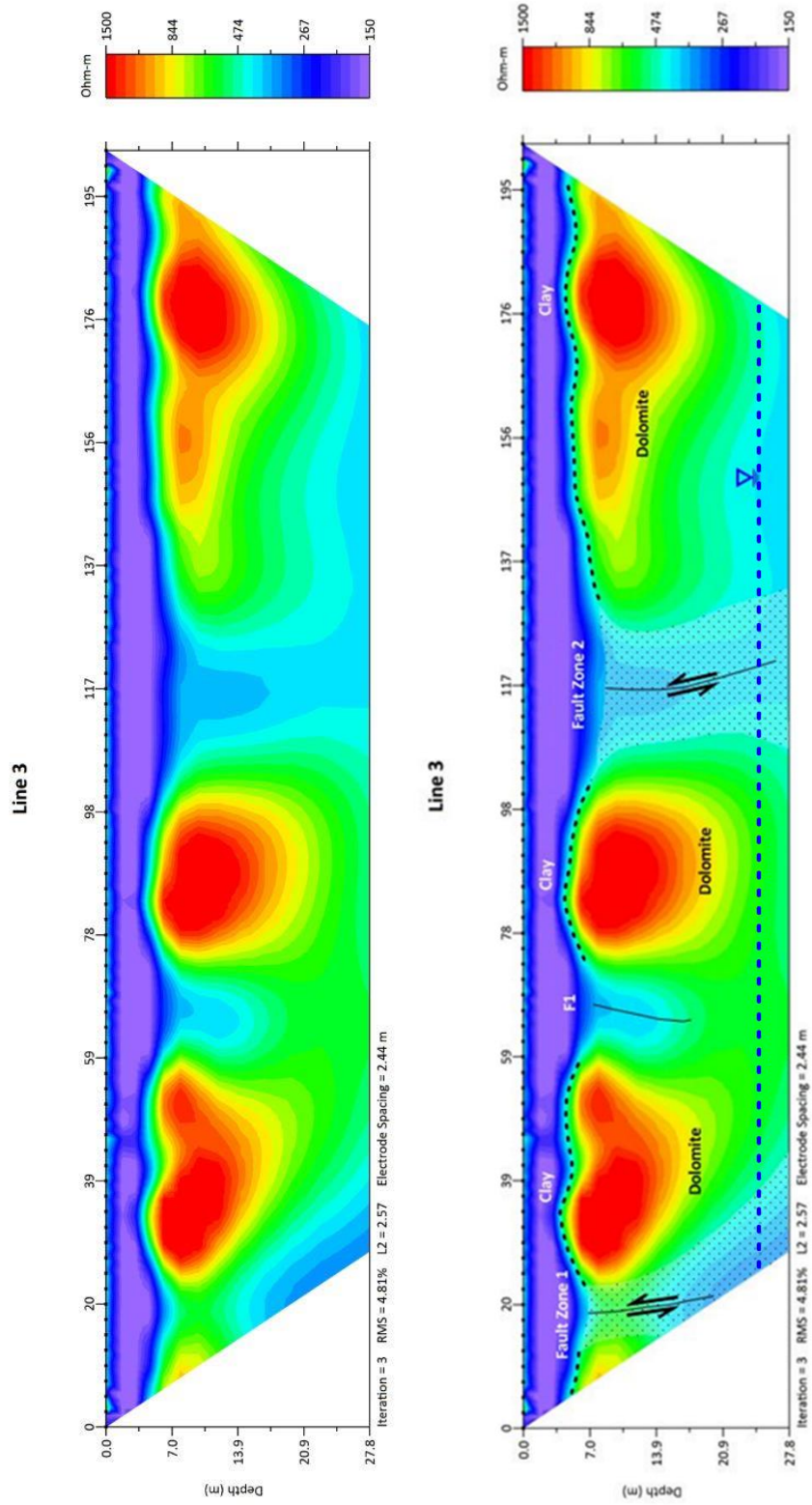


Figure 6.2 Line 3: Unannotated and annotated resistivity sections

Line 4

Line 4 dipole-dipole data were collected from northeast-to-southwest, is the easternmost profile, and is situated approximately 30.4 m northeast of the documented LNAPL plume (Figure 7.0). Figure 6.3 shows that the resistivity values within the interpreted clay layer range from 150 Ω m to 250 Ω m and indicates a clear overburden-bedrock interface. Bedrock is present from approximately 7 m to the base of the profile at 27.8 m. Bedrock resistivity values range from 350 Ω m to 1500 Ω m. High value resistivity measurements are present nearest the top of bedrock and are likely attributed to less porewater. Notable low bedrock resistivity values are most present towards the base of the profile near the interpreted water table at 75 m. FZ-1 and FZ-2 are the most notable features on Line 4. FZ-1 falls laterally along Line 4 between 10 m and 28 m and is present from the top of bedrock to the base of the profile. The resistivity values within FZ-1 range from 200 Ω m to 300 Ω m and has an apparent dip direction to the southeast. A significant interpreted fracture is also present near FZ-1 and falls laterally along Line 4 at approximately 56 m. Significant low resistivity values observed on the profile near these two features are likely attributed to greater pore water content. FZ-2 is still somewhat well-pronounced at near the top of bedrock and falls laterally along Line 4 between 115 m to 125 m. This zone also exhibits notably low resistivity values in the 200 Ω m to 300 Ω m range. A significant attribute to FZ-2 is that the fault zone appears to become narrower and indicates a slightly higher resistivity signature at the base of the profile. FZ-2 is approximately 15 m wide at the top of bedrock and appears to have an apparent dip direction to the northwest to a depth of 14 m.

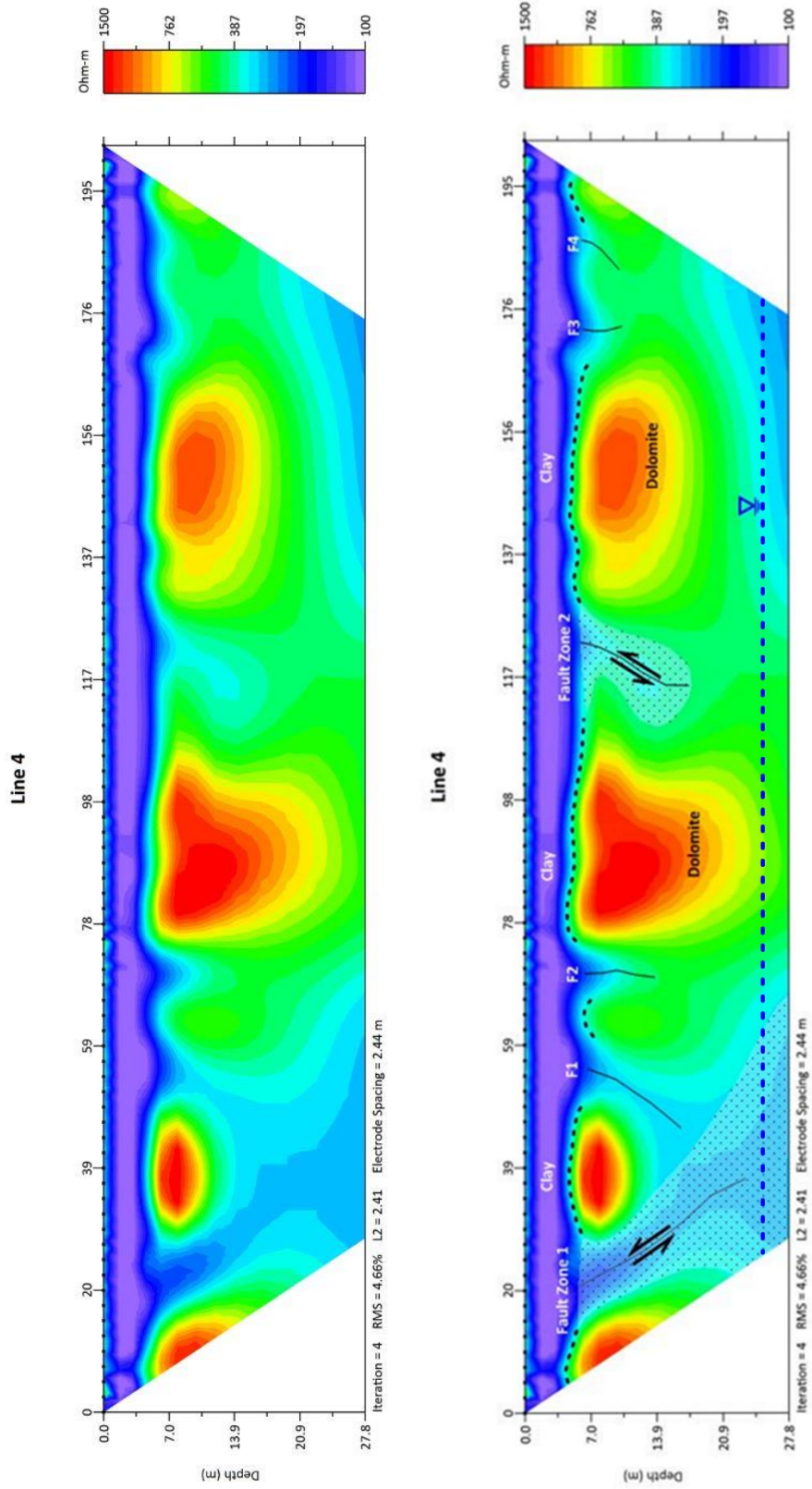


Figure 6.3 Line 4: Unannotated and annotated resistivity sections

Line 5

Line 5 dipole-dipole data were collected from southwest-to-northeast, or roughly perpendicular to Lines 1 – Line 4 (Figure 7.0). This line was located near the northern edge of the documented LNAPL plume and was positioned so that the boundary of the plume fell approximately halfway along the ERI line. As observed in ERI lines 1-4, Figure 6.4 shows that the interpreted clay layer is a well-defined low resistivity zone with values ranging from 100 Ω m to 150 Ω m. Clay thickness ranges predominantly from 3 m to 7 m, except for two notable, localized variations to a depth of 10 m, which fall laterally along Line 5 at 100 m and 160 m, respectively. Small scale fracturing is present and is presumably attributed to regional faulting. Bedrock resistivity values are relatively consistent throughout the profile and range from 500 Ω m to 1500 Ω m. The highest resistivity values are present on the right side of the profile and extend from the top of bedrock to the base of the profile. The left half of the profile shows slightly lower resistivity values of 750 Ω m to 1000 Ω m. This response may be due to slight variation in chemical weathering or somewhat higher pore water content. In general, Line 5 shows a clear overburden-bedrock boundary, little variation in bedrock topography, and some small-scale fracturing. Depth to water on this profile is difficult to interpret but is likely around 25 m. Lastly, a characteristic of Line 5 that may be significant is that the high resistivity boundary on the right half of the profile correlates to the same approximate boundary as the documented LNAP plume showed in Figure 5.6 below. As groundwater will follow the path of least resistance, the high resistivity zone identified in Line 5 may have a significant influence on the ability of groundwater to move within the subsurface at this specific location.

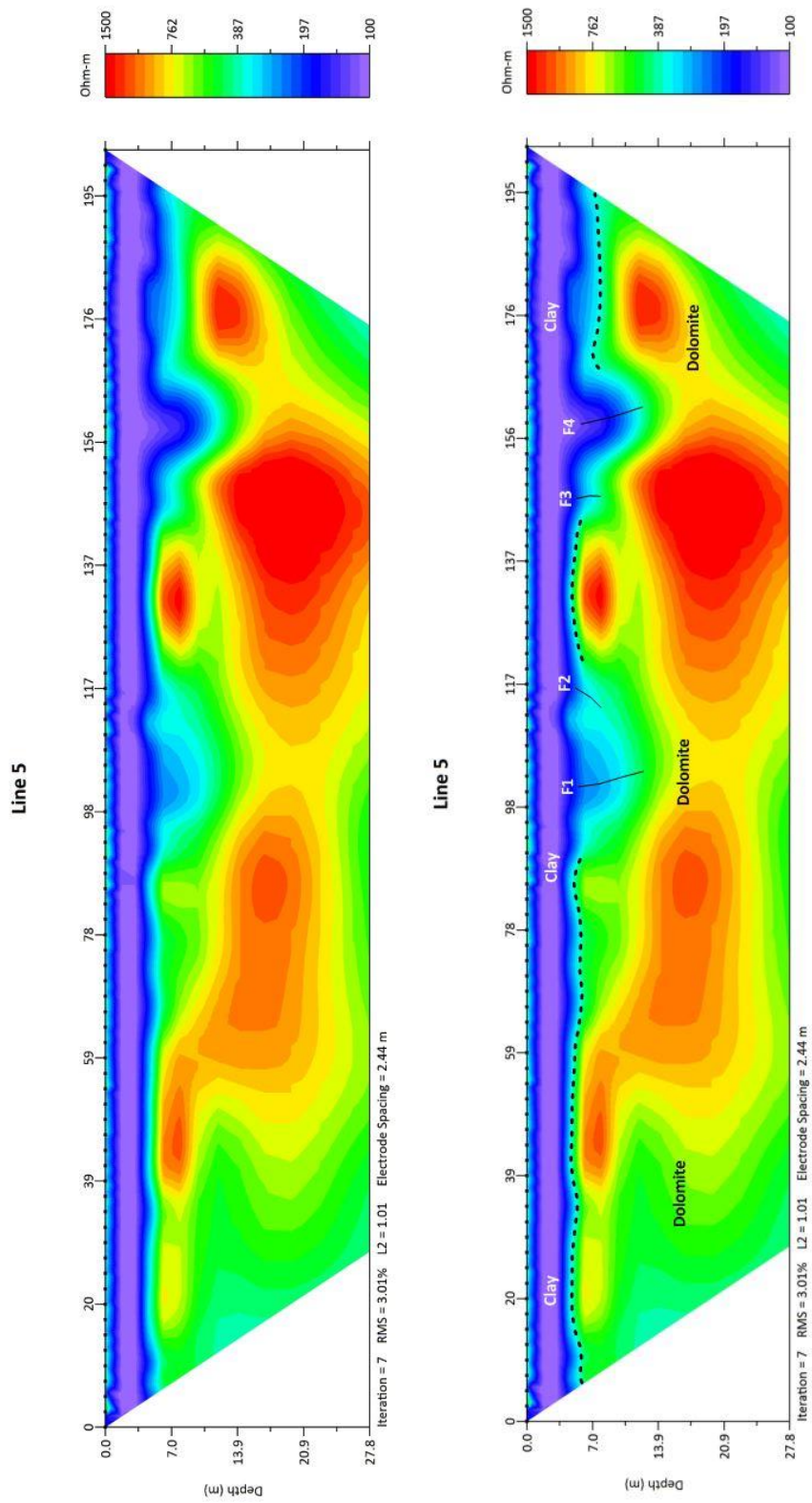


Figure 6.4 Line 5: Unannotated and annotated resistivity sections

Line 6

Line 6 dipole-dipole data were collected from southwest-to-northeast, or roughly perpendicular to Lines 1–4 near their southernmost positions, respectively (Figure 7.0). This line was intentionally oriented near the southern edge of the documented LNAPL plume to characterize bedrock topography with respect to the anticipated strike of the fault. Figure 6.5 shows that the resistivity values of the clay layer range from 100 Ω m to 150 Ω m. As observed in Lines 1 through Line 5, a clear resistivity boundary is presented between clay and bedrock. Clay thickness is relatively constant at approximately 7 m along Line 6 from 0 m to 117 m, where a dip in bedrock is present from 117 m to the end of the profile. Clay thickness is greatest near the easternmost edge of the profile and reaches depths of up to 14 m or almost double the average thickness observed on lines 1-5. Bedrock resistivity values observed on Line 6 are the most consistent of all the profiles, where the resistivity values range from 1500 Ω m near the top of bedrock to approximately 500 Ω m near the water table. Similarly, the highest resistivity values are typically nearer the overburden-bedrock interface and is likely a function of less saturation and more competent bedrock. The most notable feature on Line 6 is the significant dip in bedrock displayed at the northeastern end of the profile. This feature is located near the northeastern most extent of the documented LNAP plume and falls along the same point where the FZ-2 appears to change trajectory from northeast to a more easterly path near MW-20. The apparent dip in bedrock topography is to the northeast and has a very low angle. It should further be noted that a similar attribute was not observed in Line 5, which was located to the north and was oriented parallel to Line 6. This suggests a complex variation in structural features exists between Line 5 and Line 6.

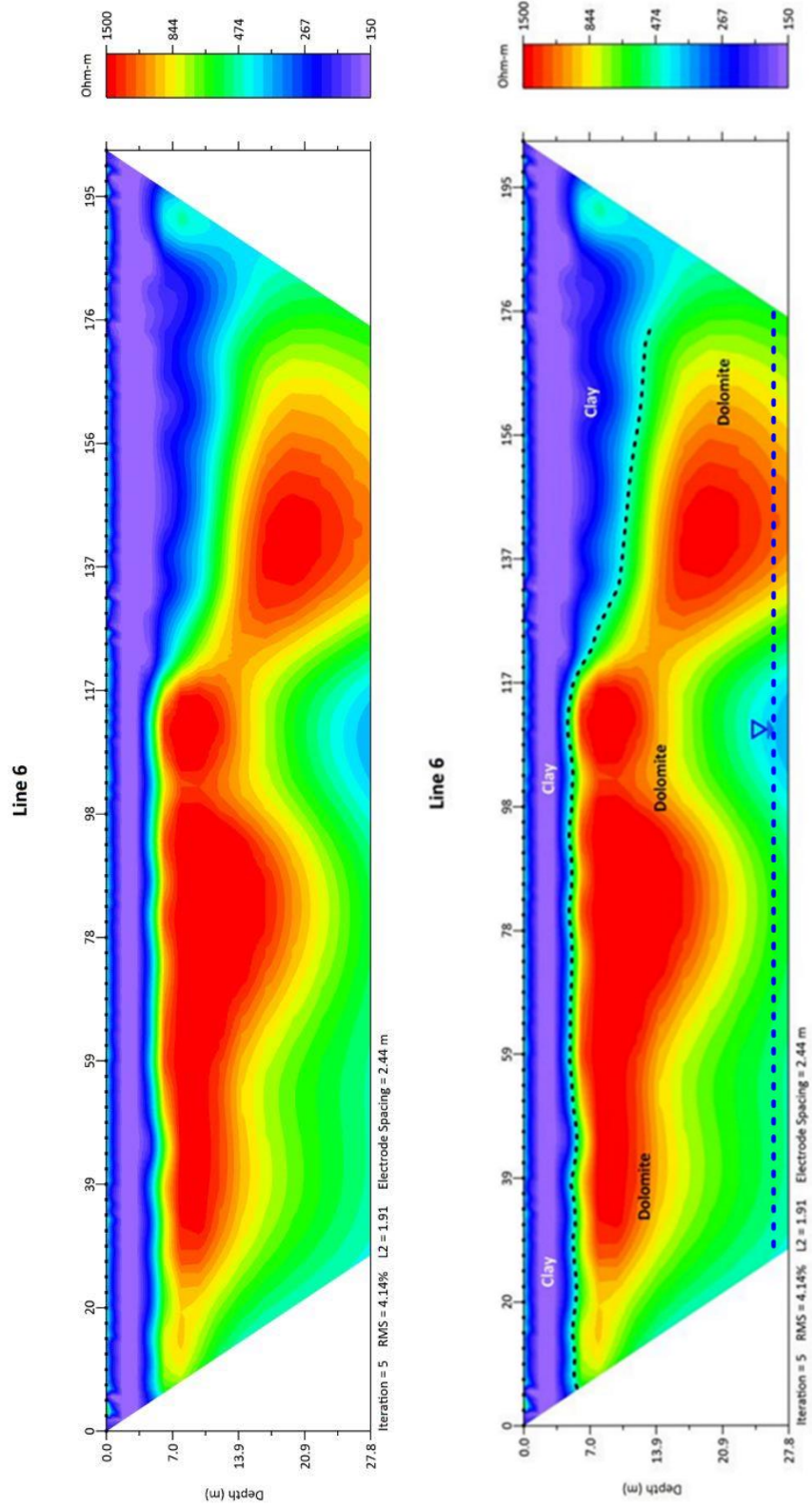


Figure 6.5 Line 6: Unannotated and annotated resistivity sections

6.2 Borehole Geophysical Survey

Note that log depth is shown and described in imperial units due to software limitations. The geophysical well logs collected in MW-17 and MW-19 have been processed, annotated, and are presented below in a standard well log format with a 1ft: 20ft scale. This scale was selected to best show borehole characteristics and variations in measurements. On each log, column one (left) shows the caliper and gamma ray data, column 2 shows the four resistivity curves and tad pole plot, column three shows the fluid resistivity, temperature, and heat pulse flow meter data. Column four shows the polar projection plot of the structural data of fractures and bedding plane (BP) features. Column five shows an oriented optical televiewer image of fracture locations with annotations showing dip direction and dip angles of all identified bedding and fracture features. Data tables showing measured structural geologic features are also shown in Table 3 and Table 4.

6.3 A General Comparison of Newly Obtained OPTV Data to Previous Logs

MW-17 is cased to 19.3 m below ground surface and has a total depth of 28.3 m, and MW-19 is cased to 18.3 m below the ground surface and has a total depth of 44.5 m. Therefore, the borehole data are limited from 19.3 m to 28.3 m, and 18.3 m to 44.5 m, respectively. This provided further insight into bedrock structure orientations and vertical flow conditions well below the measured depth of 27.8 m in the resistivity cross sections.

As anticipated, the observed structural responses from both MW-17 and MW-19 were, in general, highly similar in strike trends of both bedding features and fractures observed in the 46 bedrock wells discussed in chapter three. MW-17 and MW-19 both show both a general southeasterly trend in both bedding plane and fracture strike orientations. Dip angles of bedding planes and fractures were also similar and trend to the southeast between 30 degrees and 60 degrees, respectively. The well log results for each probe collected in MW-17 and MW-18 have been described in detail below.

6.4 Borehole Geophysical Survey Results for MW-17

Caliper

The caliper probe response in MW-17 was relatively consistent throughout the log, suggesting only minor deviations in borehole diameter are present throughout the well. The caliper response displayed little-to-no variation in response from the bottom of casing to a depth of approximately 93.6 feet. A very slight variation was observed at a depth range of 93.6 feet to 94.4 feet and displayed an increase in borehole diameter from 7.25 inches to a width of approximately 8.2 inches. From 94.4 feet to 135.6 feet again displayed straight-line characteristics, suggesting the borehole diameter remained constant. Although the magnitude of response is only slight, the most notable variation in borehole diameter occurs at a depth range of 135.6 feet to 137.8 feet, which show an increase in borehole diameter with a range of 7.25 inches to 8.5 inches or an increase of 1.25 inches. At a depth of 137.8 feet to the bottom of the log, the caliper response curve remained at a fixed position of 7.25 inches, indicating no variation in borehole diameter was present within that depth range.

Gamma Ray

Gamma responses in MW-17 ranged from approximately 10 counts per second (cps) to 95 cps. The greatest observed values occurred between the ground surface and a depth of 33.6 feet below top of casing (TOC) and is presumably caused by the greater potassium content in the clays versus the dolomitic bedrock below. Although the responses are greater within this depth range, it should be noted that these measurements were made while enclosed in steel casing and can cause up to a 20 percent decrease in cps responses. Gamma responses from a depth range of 33.6 to 80.2 feet remained relatively constant and showed responses between 5.0 cps to 35.0 cps. An increase in the gamma response occurs from a depth range of 81.4 feet to 88 feet, where values of 40 cps to 52 cps were measured. Constant gamma responses were measured from 88.0 feet to 113.4 feet, suggesting little variation in lithology exists within this zone.

Although minor, a wave-like peak-to-base response was measured between 113.4 feet to 125.2 feet, where peak values of 50 cps were observed at 116.0 feet, base responses were 10 cps at 119.0 feet, a secondary peak response of 60 cps at 122.3 was measured, and a base measurement of approximately 15 cps at 125.2 was recorded. Another notable increase occurs between 142.8 feet to 144.2 feet, where values of 50 cps were measured, followed by constant values of approximately 30 cps from 144.2 to 147.9 where the log terminates. It should be noted that these variations in response below the clay layer are minor and are not typically indicative of major variations in lithology.

Formation Resistivity (8, 16, 32, 64-inch normal)

The resistivity measurements begin at varying depths below the water table and is a function of electrode spacing within the instrument (for each resistivity measurement) and the need to transmit electrical signals through groundwater water (a conducting medium), into the formation, and transmitted back through the water column to be detected by receiving electrodes. Electrode spacing in this instrument is greatest for larger measurements (e.g. 64-inch) and lesser for smaller measurements (e.g. 8-inch); therefore, the 8-inch measurement can occur nearer the water table (shallower) than the 64-inch measurement which occurs deeper on the log.

Constant-to-near constant 8, 16, 32, and 64-inch normal resistivity values were recorded from 94.0 feet to 118.4 feet, where the values range from 5 Ω m to 1800 Ω m, respectively. This would suggest little-to-no variation in lithology is present within this depth range. A significant increase in resistivity values was recorded from 118.4 feet to 125.0 feet and appears to correlate with a high gamma response as zone discussed above. Resistivity measurement decrease from 125.0 feet to 134.4 feet and maintain a relatively constant range from 5 Ω m to 700 Ω m, respectively. A significant increase was again observed from 134.4 to 139.0, where a range of 700 Ω m to 1400 Ω m was measured, with a slight decrease in range values from 139.2 feet to 142.3 feet, where the range was approximately 20 Ω m to 700 Ω m. From a depth of 142.3 to 147.2 resistivity values again increased slightly from 700 Ω m to 1400 Ω m, respectively. This wave-like response may be related to variations in localized bedrock competency. Lastly, resistivity measurements remain constant from 147.2 to the bottom of the log.

Fluid Resistivity

A very fine scale of 15 Ω m to 18 Ω m was used to best define variations in fluid resistivity measurement. It is presumed that existing borehole fluids may have differing resistivity values than newly introduced formation fluids entering the borehole. Therefore, the introduction of formation fluids into the borehole may appear as abrupt, very slight increased or decreased responses on the curve. Additionally, the fluid resistivity measurement can only be taken below the water table. The most notable change on slope for the fluid resistivity measurement occurs just below the water table at a depth range of 74.0 feet to 74.8 feet, where the values decrease from 17.5 Ω m to 16.75 Ω m, respectively. Based on this variation, it suggests that a variation in borehole fluid resistivity is present and may be related to a water-producing zone. From a depth of 74.8 feet to 112.6, the values remain relatively constant at approximately 16.75 Ω m, where a second change in slope occurs at 112.6 showing a slight increase in fluid resistivity responses at approximately 17 Ω m. It appears that the fluid resistivity values remain consistent at approximately 17 Ω m from 112.6 feet to the bottom of the log, further indicating that the likely water-producing zone within MW-17 is located within the 74.0-foot to 74.8-foot zone.

Temperature

Constant temperature responses were observed from 68.0 feet to 91.8 feet and remained at approximately 14.9 Deg C. This constant response suggests that formation water is not likely entering the borehole within this range, especially when compared to

the caliper log which implies competent rock is also present throughout this zone. A slight decrease in temperature was observed at a depth of 91.8 feet, where fluid resistivity values decrease linearly from 14.8 Deg C at 91.9 feet to 14.5 Deg C at 112.0 feet. A notable change in slope for this measurement occurs at a depth of 112.2 feet to 112.8 feet where a decrease of approximately 0.4 Deg C occurs. Based on this response, it is possible that formation water is also entering the borehole at this depth. From 112.8 feet to 147.8 feet, near constant temperature values of approximately 14.5 Deg C were observed to the bottom of the log.

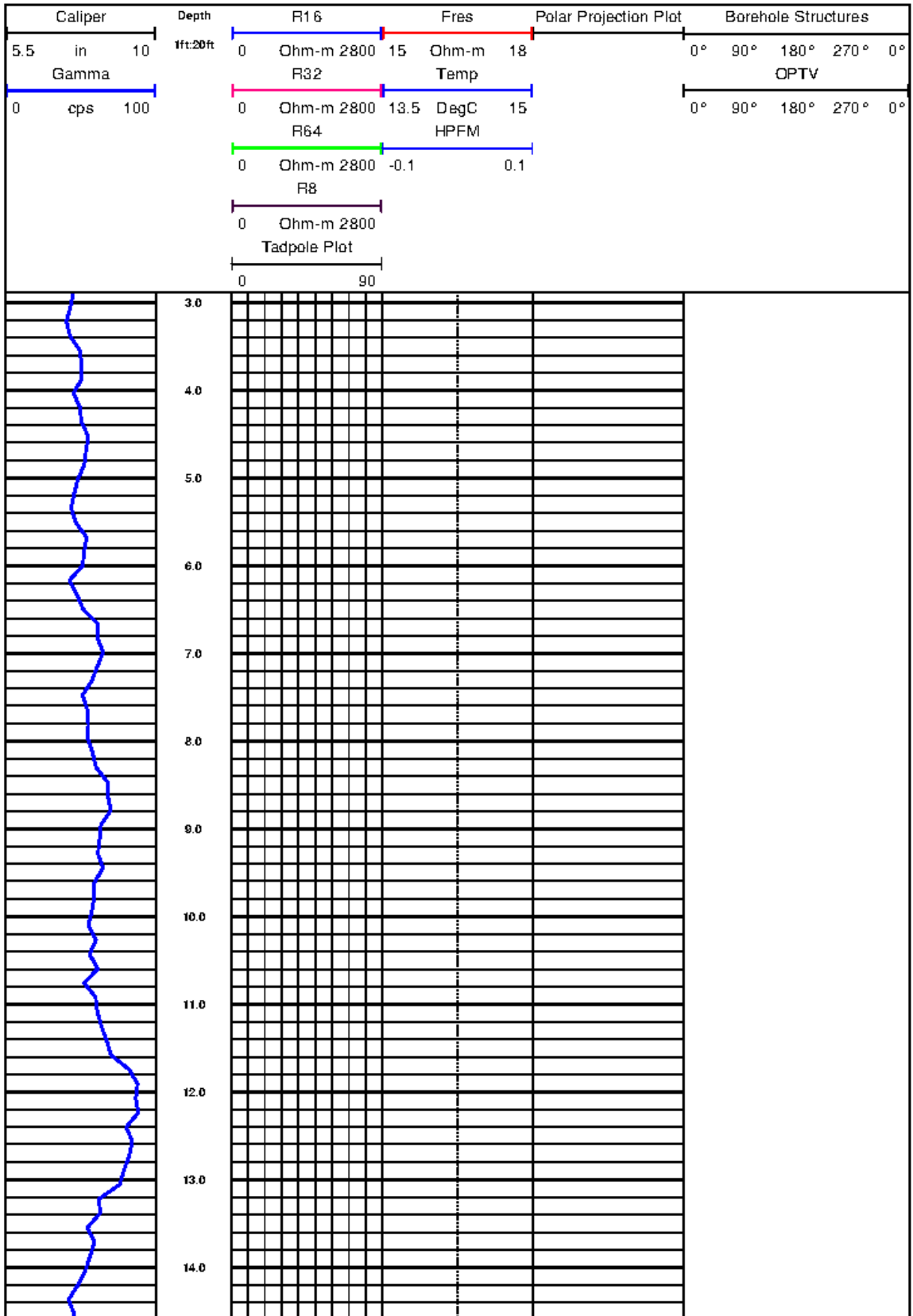
Heat Pulse Flow Meter

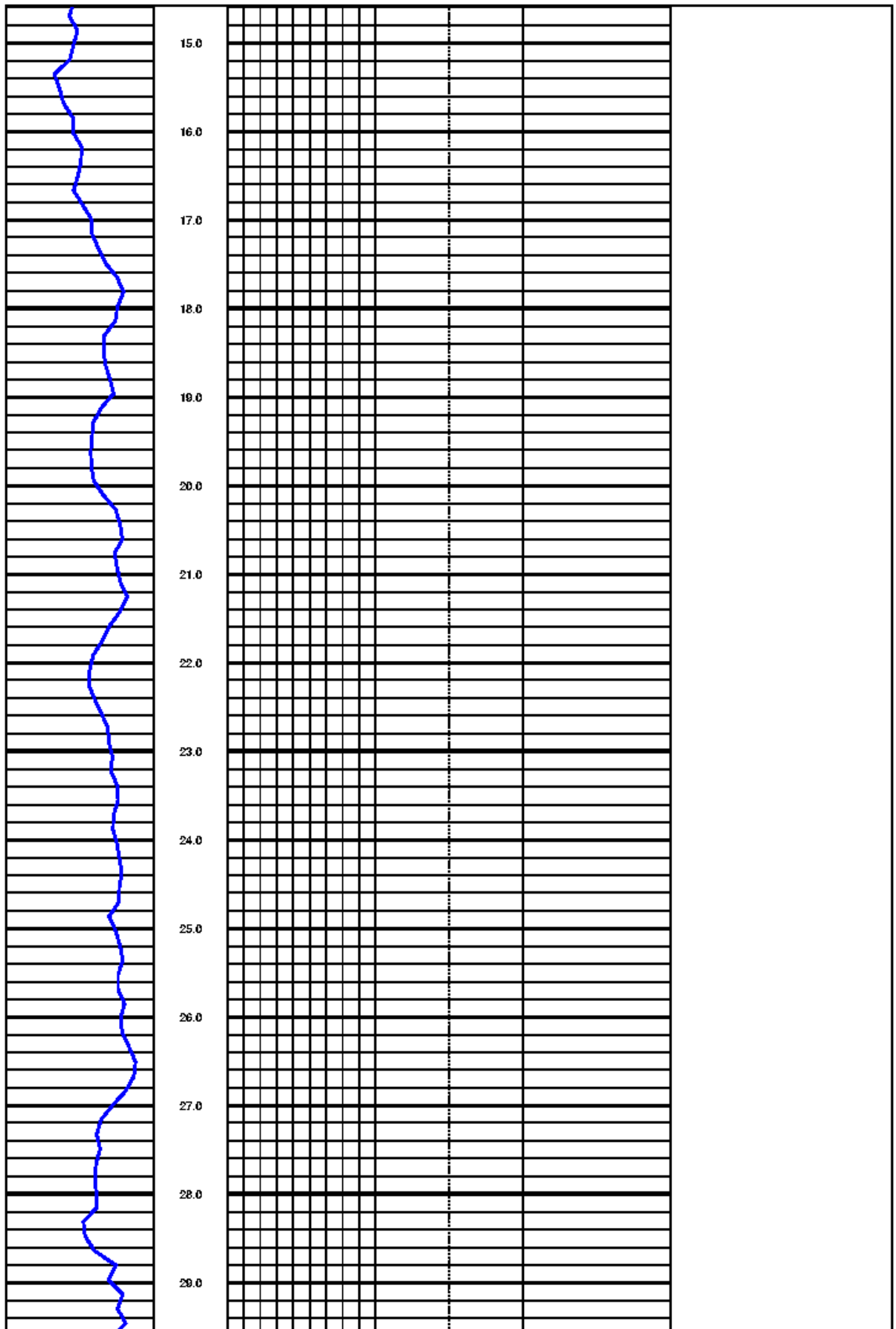
Five heat pulse flow meter (HPFM) measurements were taken at predetermined positions based on caliper and optical televiewer responses. The five zones were located at 75 feet, 80 feet, 113 feet, 134 feet, and 137.5 feet, respectively. Downward flow is indicated by negative values (left of center) and, conversely, upward flow is indicated by positive values (right of center). A very fine scale of -0.1 to 0.1 gallons per minute (gpm) was used to best show vertical flow within this well. This scale is used for wells with anticipated very low-to-low flow to no-flow conditions. Additionally, it should be noted that the values shown on the logs and described below were the mean average calculated from five samples collected at each of the five depth positions. The first HPFM measurement at a depth of 75.0 feet shows very fine downward flows of approximately -0.15 gpm. The second HPFM measurement taken at 113.0 feet displayed the same, with very fine downward flow measurements of -0.15 gpm. Conversely, very fine upward flow of 0.15 was observed at a depth of 113.0 feet, and the same values of 0.15 were measured at both

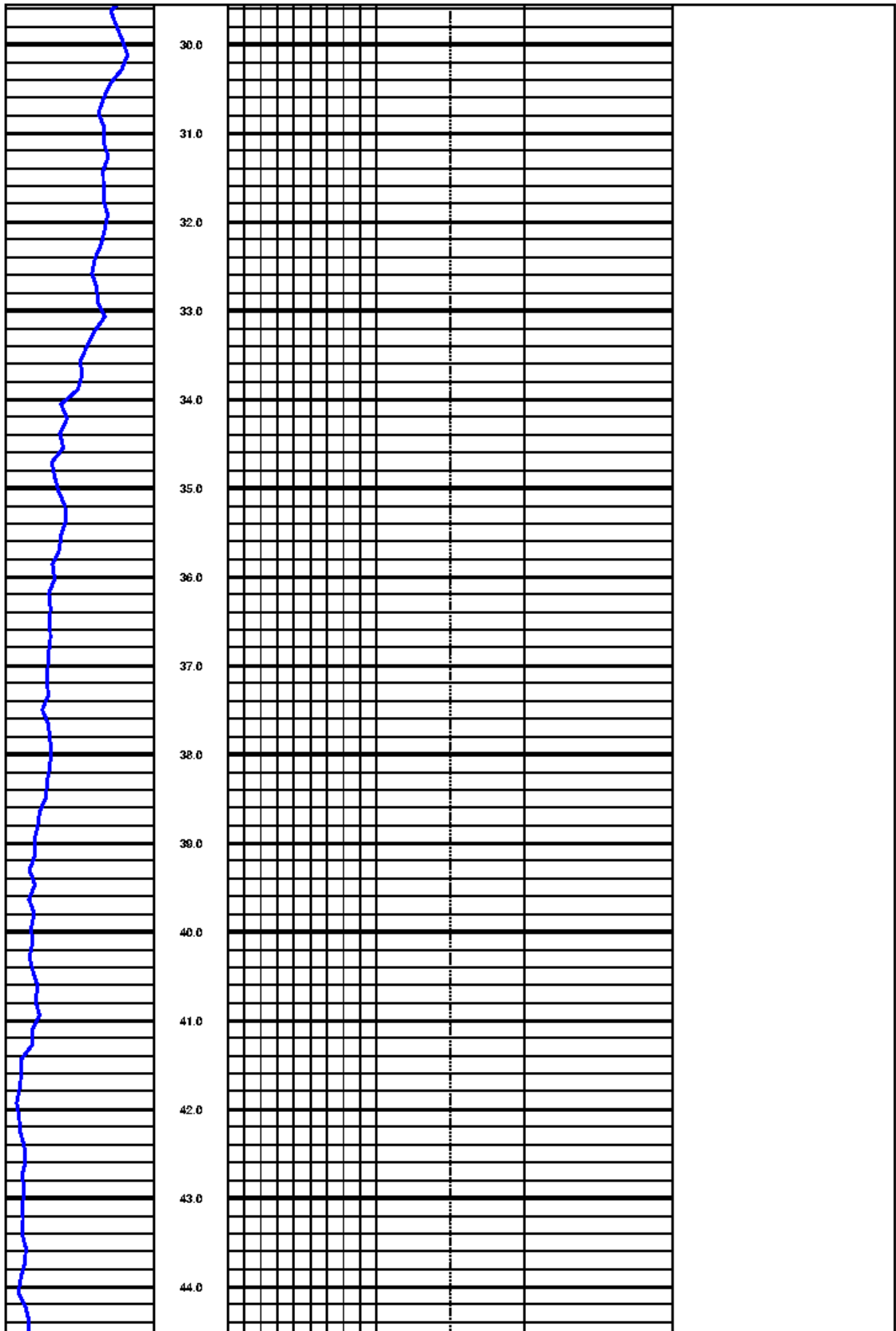
134.0 feet and 137.5 feet, respectively. These values suggest that this borehole has very low-to-no vertical flow characteristics.

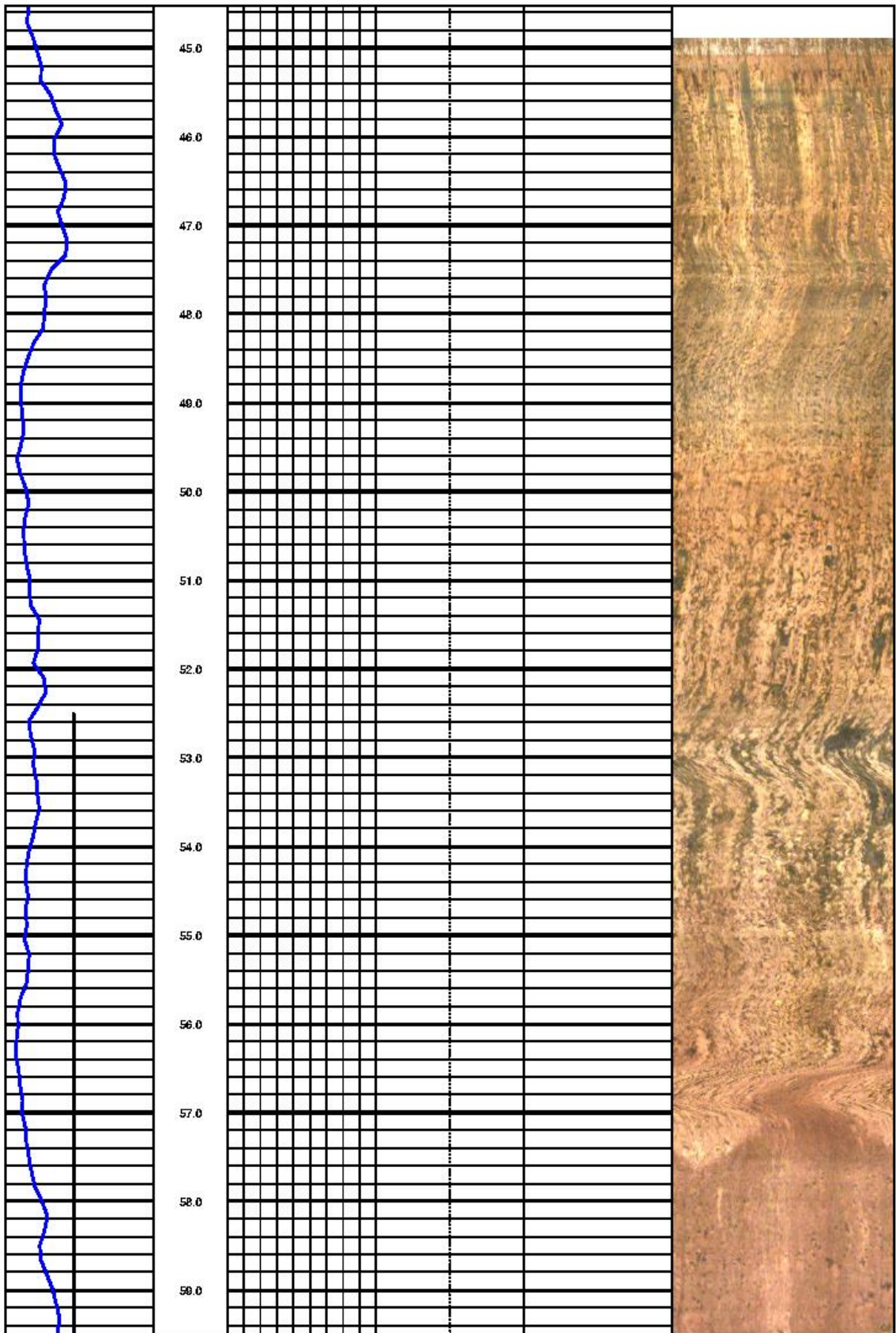
Optical Televiewer

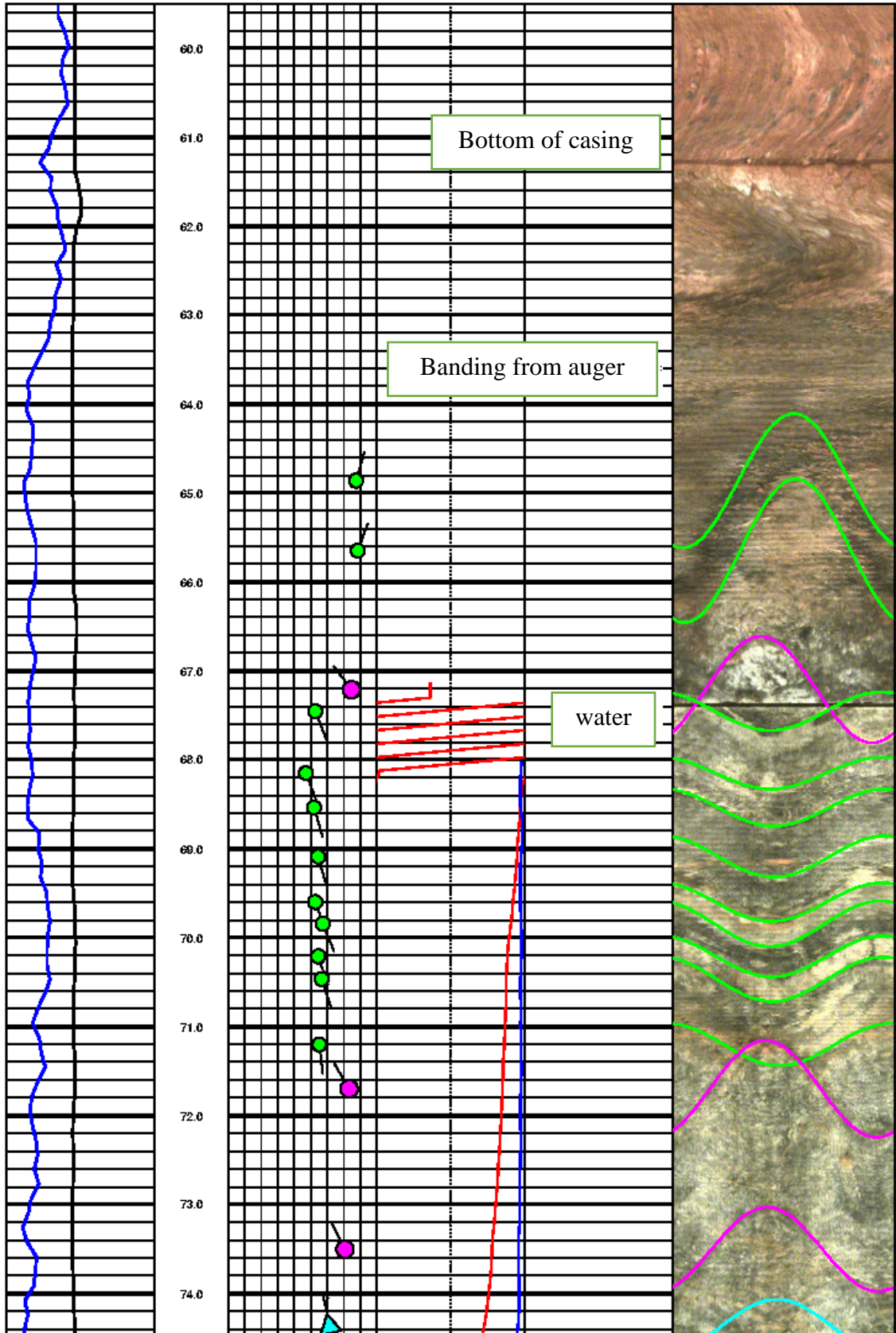
The optical televiewer (OPTV) responses of various structural features in MW-17 were used to generate the Wulff and tadpole plots displayed on the well log. The OPTV logs were analyzed to identify dip direction and dip angle information of bedding features (green), minor open fractures (purple) and in-filled fractures (cyan). Bedding features are present throughout the logs and predominantly have dip directions to the south-southeast, or roughly 162 degrees. Dip angles for bedding features ranged from 48 degrees to 64 degrees, with a mean of approximately 62 degrees. Measured strike for minor open fractures were also predominantly to the south east - except for several outliers with northerly strikes - and ranged from 55 degrees to 75 degrees, with a mean average of approximately 66 degrees. In contrast, the majority of the in-filled fractures had northwesterly trending strikes with dip angles between 51 degrees and 70 degrees, with a mean average of approximately 64 degrees. No notable major fractures or void spaces were observed on the logs.

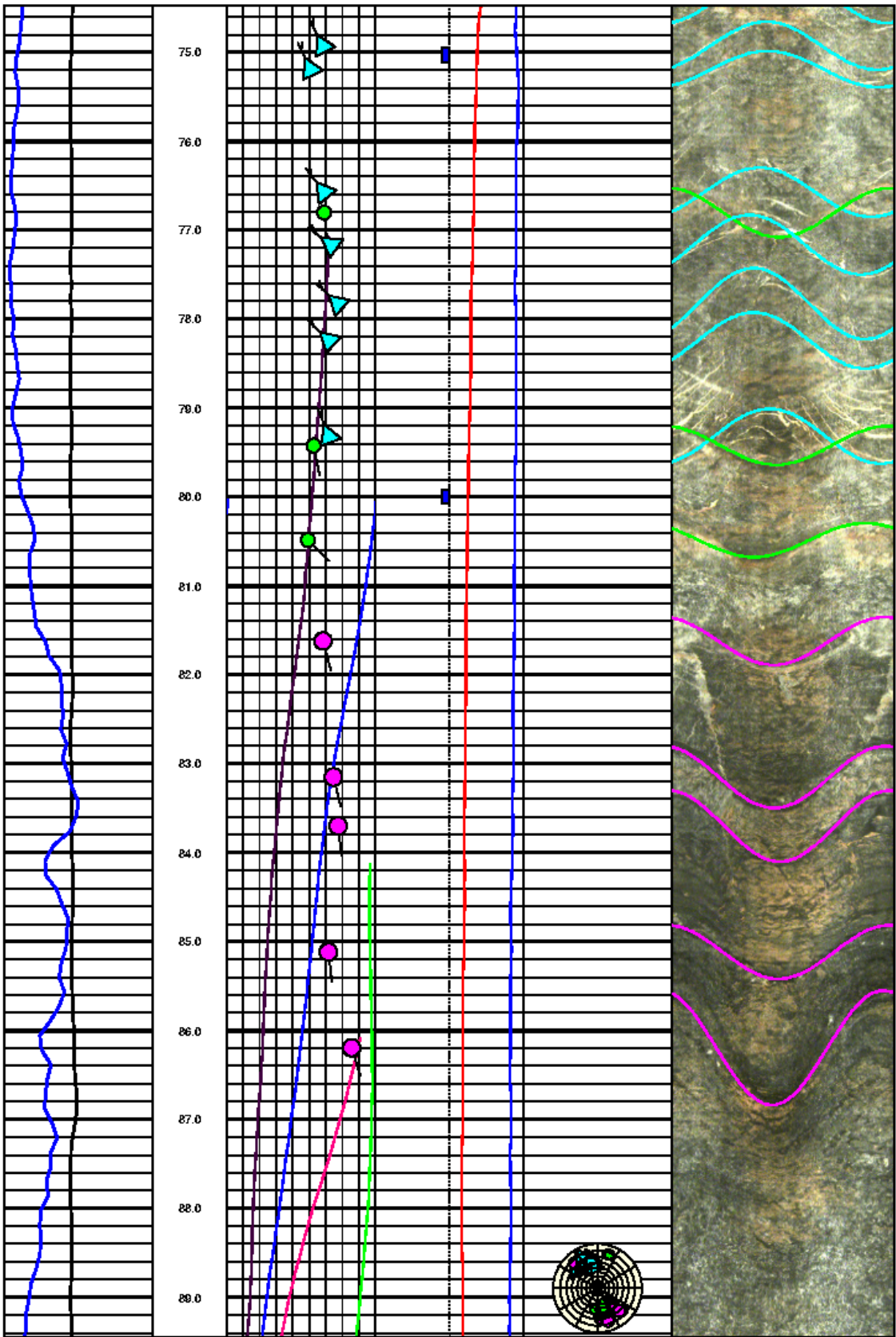


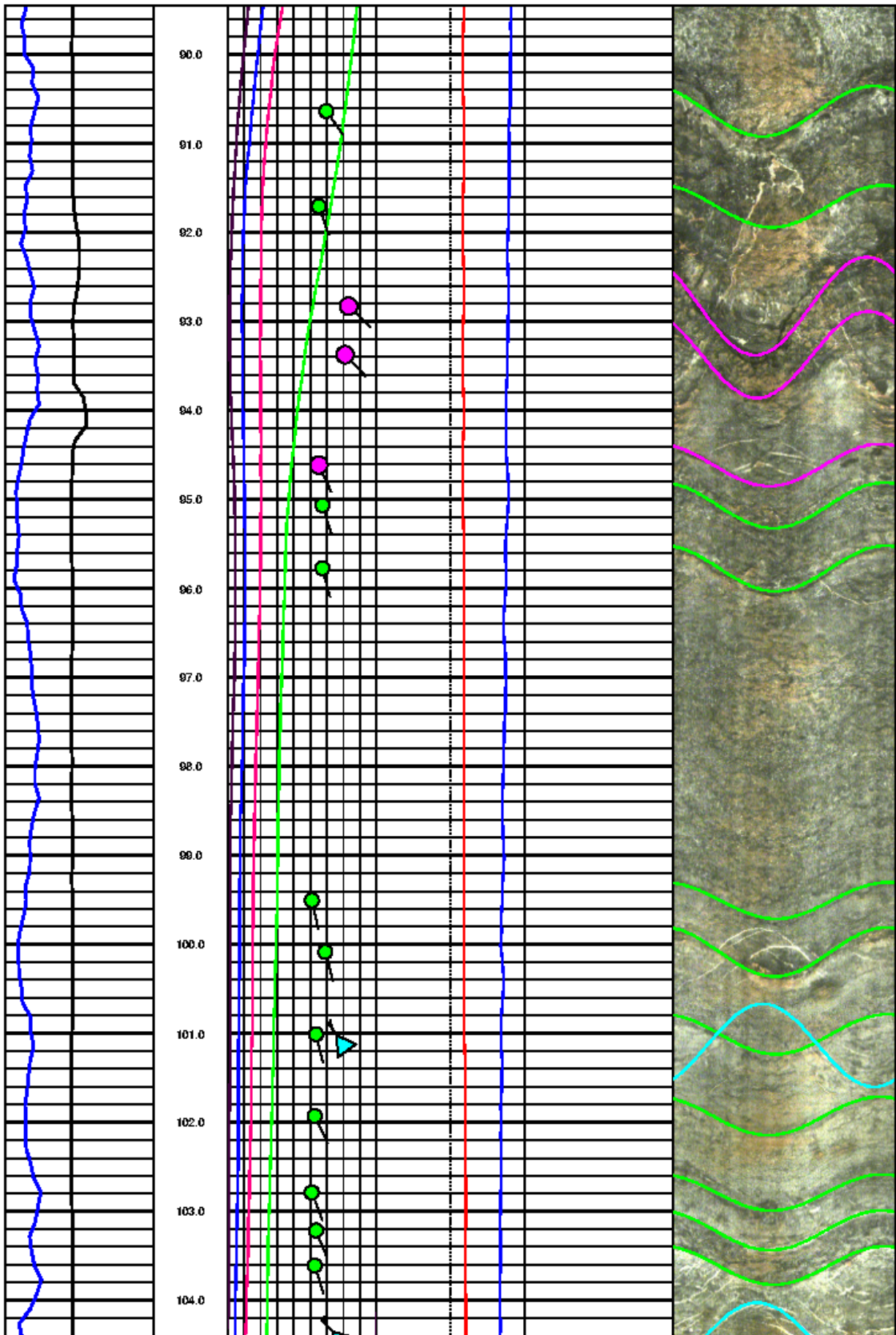


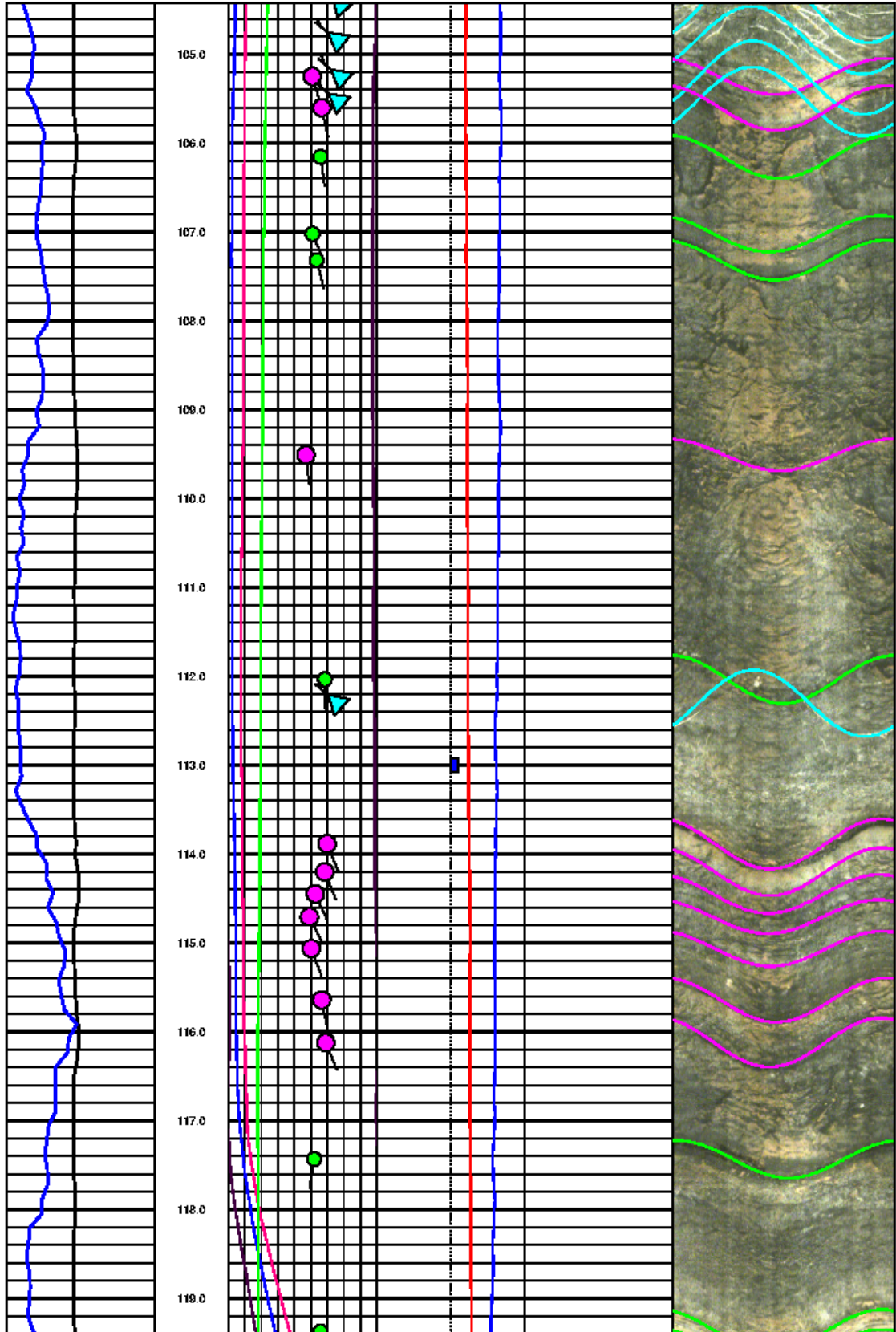


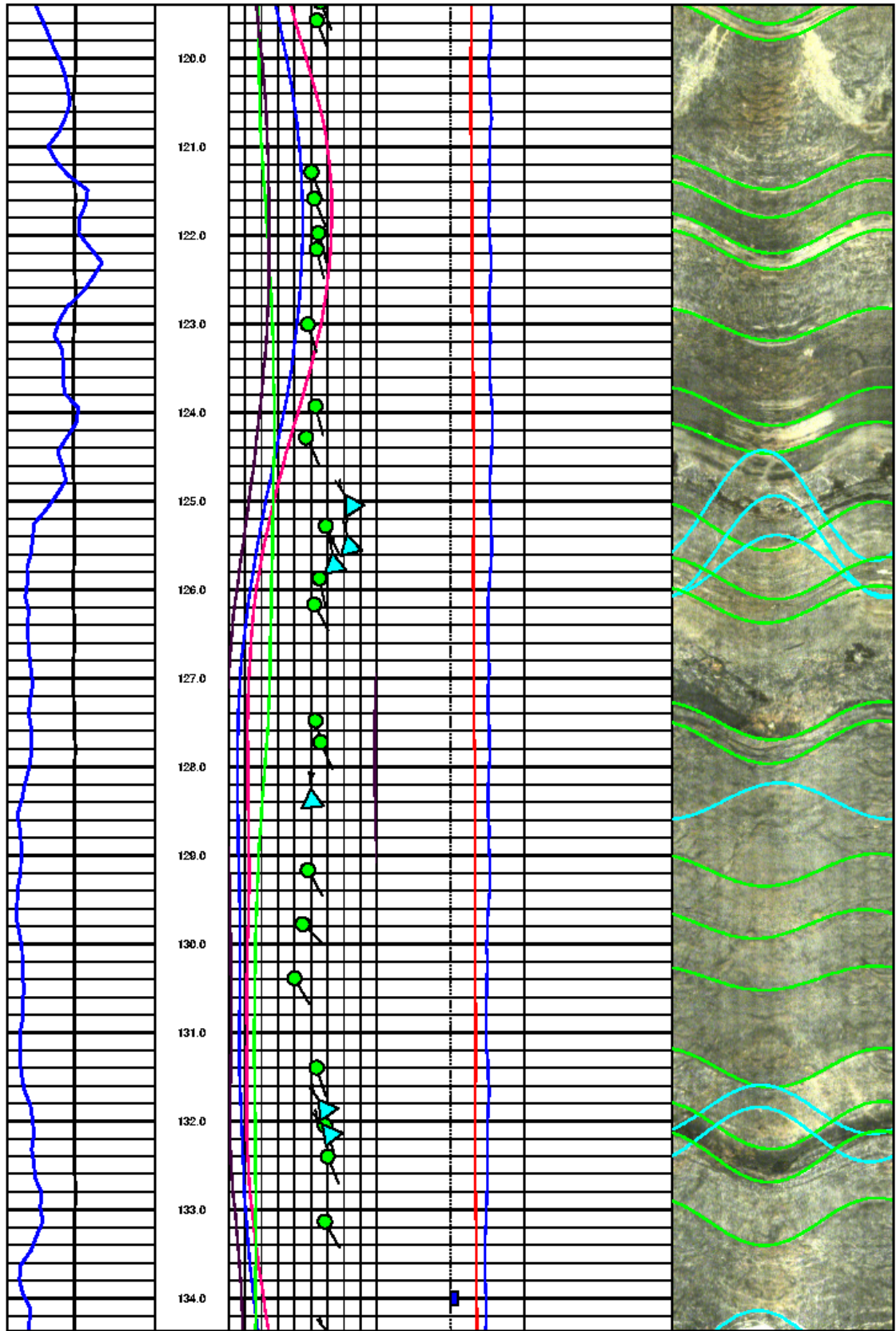


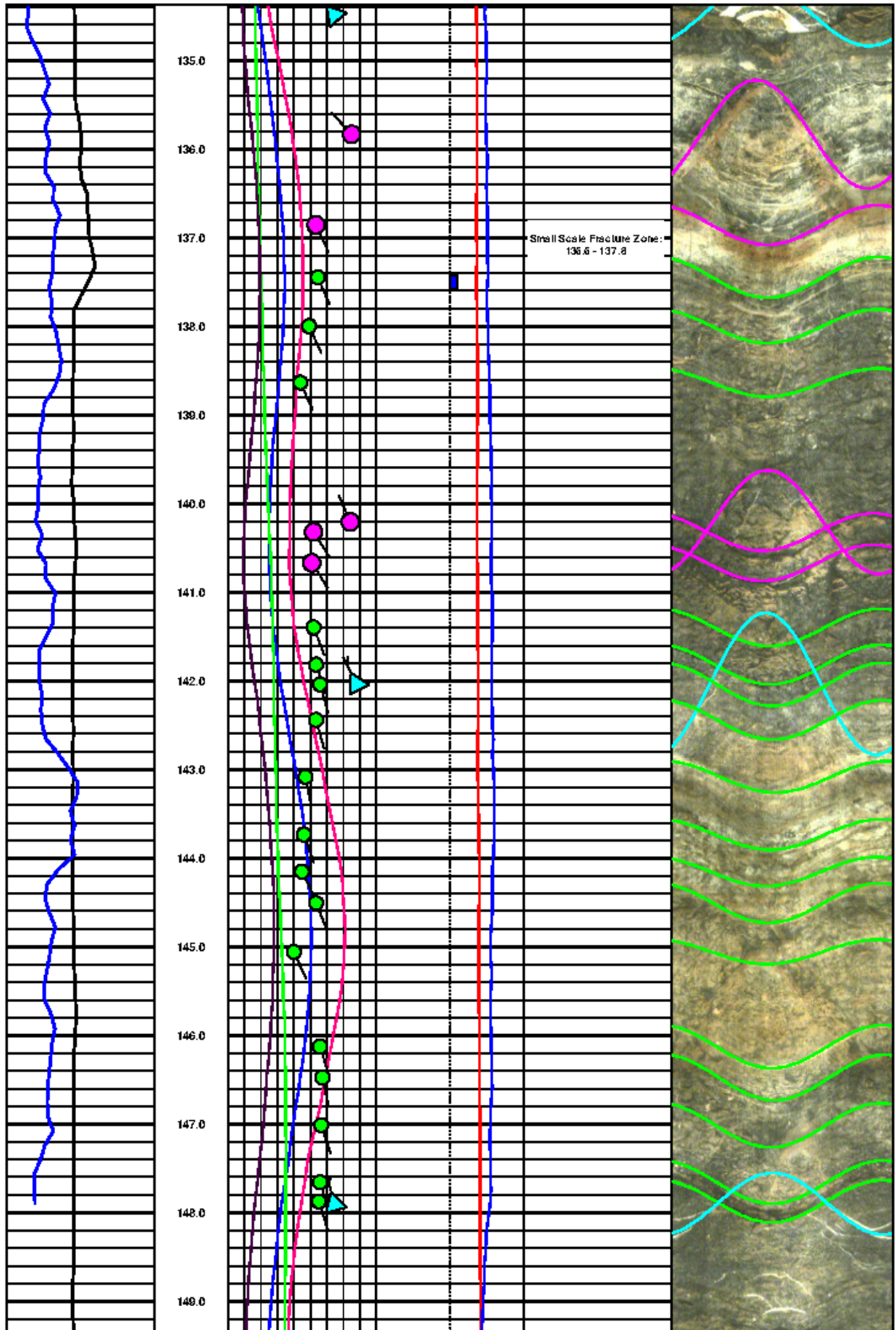












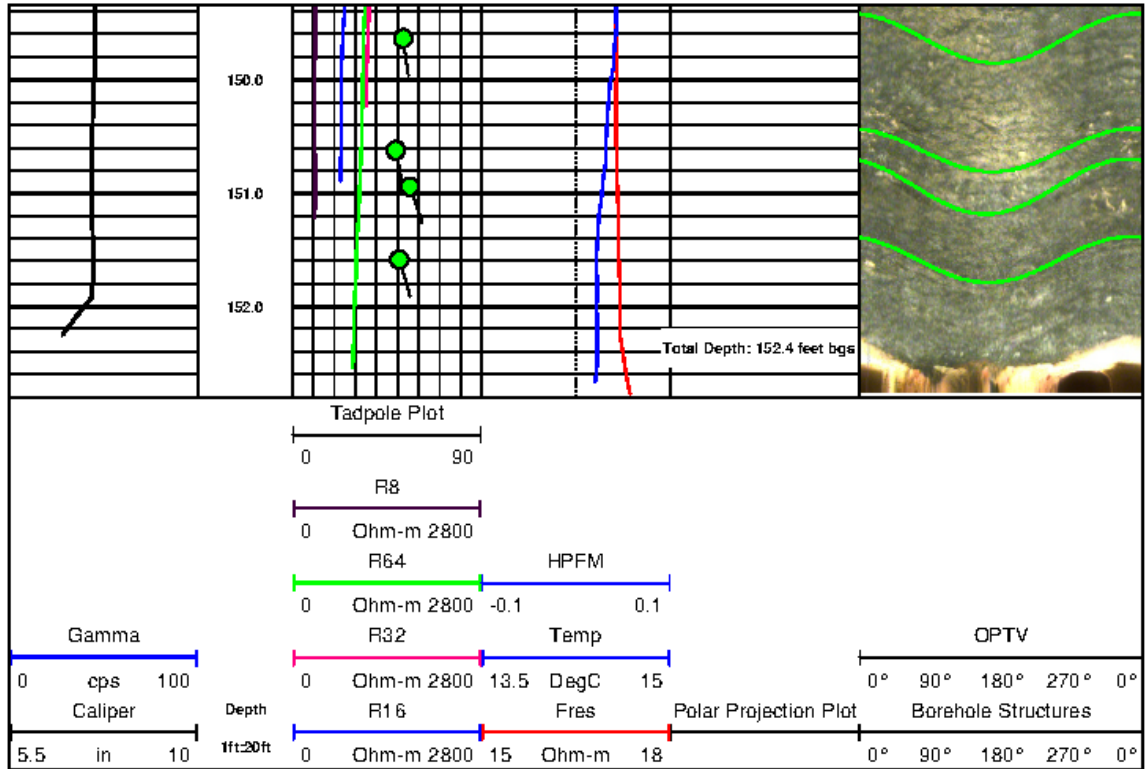


Figure 6.6 MW-17 well log results

Table 3: MW-17 Bedrock Structures

Depth (feet)	Dip Direction (degrees)	Dip Angle (degrees)	Comments
61.25			Bottom of Casing
64.8	16	77	Bedding Plane (BP)
65.6	19	78	BP
67.2	323	75	Minor Fracture (MF)
67.4			WATER
67.4	158	53	BP
68.2	159	47	BP
68.5	164	52	BP
69.0	164	54	BP
69.5	160	53	BP
69.8	157	57	BP
70.1	160	54	BP
70.4	161	56	BP
71.1	172	55	BP
71.6	330	73	MF
73.5	332	71	MF
74.3	348	61	In-filled Fracture (IFF)
74.9	333	59	IFF
75.1	335	51	IFF
76.5	322	59	IFF
76.7	173	59	IFF
77.0	305	63	IFF

Table 3 (continued): MW-17 Bedrock Structures

Depth (feet)	Dip Direction (degrees)	Dip Angle (degrees)	Comments
77.7	312	67	IFF
78.1	312	62	IFF
79.F2	338	62	IFF
79.4	168	52	BP
80.5	133	49	BP
81.6	165	58	MF
83.1	166	65	MF
83.6	175	67	MF
85.1	173	61	MF
86.2	162	76	MF
90.6	145	60	BP
91.7	160	55	BP
92.9	133	73	MF
93.4	136	71	MF
94.6	155	55	MF
95.0	162	57	BP
95.7	165	57	BP
99.5	167	51	BP
100.0	165	59	BP
100.9	166	54	BP
101.0	325	70	IFF
101.9	154	52	BP
102.8	159	51	BP
103.2	57	53	BP
103.6	163	53	BP

Table 3 (continued): MW-17 Bedrock Structures

Depth (feet)	Dip Direction (degrees)	Dip Angle (degrees)	Comments
104.0	316	68	IFF
104.7	307	67	IFF
105.1	309	68	IFF
105.2	164	51	IFF
105.2	309	68	IFF
105.2	164	51	MF
105.5	309	67	IFF
105.6	167	57	MF
106.1	171	56	BP
107.0	156	51	BP
107.3	165	53	BP
109.5	173	47	MF
112.0	178	59	BP
112.3	311	66	IFF
113.9	158	60	MF
114.2	158	59	MF
114.4	155	53	MF
114.6	154	49	MF
115.0	159	50	MF
115.6	167	57	MF
116.1	157	59	MF
117.4	188	52	BP
119.3	59	56	BP
119.5	159	53	BP

Table 3 (continued): MW-17 Bedrock Structures

Depth (feet)	Dip Direction (degrees)	Dip Angle (degrees)	Comments
121.3	157	50	BP
121.5	157	52	BP
121.9	167	54	BP
122.1	166	54	BP
123	163	48	BP
123.9	165	53	BP
124.2	154	47	BP
124.9	327	75	IFF
125.2	155	59	BP
125.5	345	74	IFF
125.6	350	64	IFF
125	167	55	BP
126.1	151	52	BP
127.5	162	53	BP
127.7	156	56	BP
128.3	354	51	IFF
129.1	150	48	BP
129.8	134	45	BP
130.4	150	48	BP
131.3	163	54	BP
131.8	325	59	IFF
131.9	161	58	BP
132.0	321	62	IFF
133.1	156	58	BP

Table 3 (continued): MW-17 Bedrock Structures

Depth (feet)	Dip Direction (degrees)	Dip Angle (degrees)	Comments
134.4	320	64	IFF
135.8	317	75	MF
136.8	155	53	MF
137.4	156	54	BP
137.9	155	49	BP
138.5	155	44	BP
140.1	337	74	MF
140.4	147	52	MF
140.7	147	51	MF
141.3	159	52	BP
141.7	160	54	BP
141.9	332	78	IFF
142.0	165	56	BP
142.3	164	54	BP
143.0	168	47	BP
144.1	153	45	BP
144.5	157	54	BP
145.0	155	40	BP
146.0	167	57	BP
146.1	163	45	BP
146.9	161	57	BP
147.8	345	65	IFF
149.6	171	53	BP
150.2	161	56	BP
150.6	169	49	BP

6.5 Borehole Geophysical Survey Results for MW-19

Caliper

Caliper responses in MW-19 from 60.5 feet to a depth of 72.2 feet were constant and displayed no variation in borehole diameter. At a depth range of 72.2 to 74.8 feet, very minor slope changes occur and are attributed to the presence of a cluster of minor open fractures. Borehole variations within this zone are on the order of $\frac{1}{4}$ inch and are very minor in nature. Although subtle, another notable zone within the caliper log is present at a depth range of 83.4 feet to 87.6 feet and are also attributed to the apparent series of minor open fractures. The most notable feature observed on the log is a significant void which is present at a depth range of 115.8 feet to 117.6 feet, where the caliper log shows a significant opening in the borehole wall. Below this point at a depth range of 120.0 feet to 124.5 feet, a major fracture was observed and shows a significant, roughly 3-inch, variation in borehole response. Another identified major fracture was observed at a depth of 129.0 feet, where the caliper log showed an abrupt deviation bracketed above and below by a consistent response. Towards the bottom of the log at a depth of 143.8 feet, another significant fracture was identified on the caliper log which displayed a characteristic peak response.

Gamma Ray

Gamma responses measure in MW-19 were greatest at shallower depths. From the ground surface to a depth of 24.0 feet, gamma values ranged from 55 cps to 99 cps and correlate well with interpreted clay thicknesses identified from the ERI data. As noted

above in the MW-17 *Gamma* descriptions, gamma measurements made within steel casing are reduced by approximately 20 percent. Therefore, the gamma responses in reality are significantly greater than displayed on the log.

Only minor variations in gamma responses were observed between 24.0 feet and 57.0 feet and is common in massive formations such as at this research site. Of note, undulating variation in slope occur at a depth range of 57.0 feet to a depth of 77.2 feet. This characteristic suggests that a greater variation in lithology is occurring in this zone and may be attributed to a greater presence of potassium in this localized zone. From 77.2 feet to 84.6 feet, gamma values remain relatively constant at approximately 40 cps. An abrupt variation in slope occurs from 84.6 feet to 86.6 feet, where gamma values range from approximately 55 cps to 75 cps. Gamma values of approximately 30 cps were observed from 86.6 feet to 99.2 feet, where a slight decrease of approximately 10 cps was measured between 99.2 feet to 102.0 feet. Gamma values from 102.0 feet to the log termination depth of 140.8 showed only minor variations and have a range of 20 cps to 50 cps. No other major features were observed on this log.

Formation Resistivity (8, 16, 32, 64-inch normal)

Resistivity responses in MW-19 begin at a depth of 107.2 feet and is a function of the depth to the water table. The water table was measured at 100.1 feet; therefore, electric logs could not be collected at shallower depths due to the lack of water in the borehole. The scale used for these measurements is 0 Ω m to 8,000 Ω m and was selected to best show variations in localized resistivity values. From a depth range of 107.2 feet to 131.2

feet, resistivity values for the 8, 16, 32, and 64 in normal measurements are constant and fall between 1,000 Ω m and 3,500 Ω m, respectively. No major fluctuations or changes in slope were observed within this depth range. A slight increase in all four resistivity measurements was observed between 131.2 feet to 141.6 feet fall between 1,500 Ω m to 5,600 Ω m, respectively. This zone appears as a broad increase in resistivity values bracketed above and below by relatively lower and constant resistivity values. This broad, higher resistivity zone may be associated with a localized section of more competent bedrock. Low, constant resistivity values were observed from a depth of 141.6 to the bottom of the log, where values of 1,000 Ω m to 3,500 Ω m were measured. No other significant variations in resistivity values were identified on the log.

Fluid Resistivity

The scale for the fluid resistivity measurement in MW-19 was set to a range of 15 Ω m to 18 Ω m as to best show minute variations within the measurement as described in the above subheading *MW-17 Fluid Resistivity*. Several prominent changes in slope were observed on the log and may indicate the presence of water-producing zones.

At a depth of 106.2 feet, a very increase was observed where the values increase from 15 Ω m to 18 Ω m, suggesting a significant difference in fluid resistivity values is occurring at this depth. Between 106.4 feet to a depth of 116.0 feet, a roughly linear decrease was measured and ranged from 18 Ω m to 16.4 Ω m. It should be noted that the significant fracture identified in the caliper log above is also present at a depth of 116.8 feet. From a depth range of 116.8 feet to 143.0 feet, little-to-no variation was observed,

and the fluid resistivity values remained roughly constant at approximately 16 Ω m. Lastly, another slight change in slope occurs between 143.0 feet and 144.0 feet, where the values decrease from 16 Ω m to 15.5 Ω m, respectively. It should be noted that this change in slope also aligns with a major fracture identified in the caliper log for MW-19.

Temperature

Temperature measurements in MW-19 were scaled from 13.5 degrees (Deg) centigrade (C) to 15 Deg C to best show minor variations in temperature that could relate to potential water-producing zones. Measured temperatures in MW-19 were relatively constant on a very fine scale throughout the log. From a depth of 100.1 (water table) to 110.0, temperatures were measured to be near constant at 14 Deg C with little-to-no variation. From 110.0 feet 117.0 feet, higher frequency, lower magnitude variation is present along the curve and is likely associated with the significant void space identified in the caliper log at a depth of 117.0 feet. High frequency variations such as observed in this section can occur with increased fluid movement. Although there is variation along the temperature curve within this zone, it is very moderate, and on the order of .15 Deg C. From a depth of 117.0 feet to 140.0 feet, constant values of 14 Ω m were measured and did not show any major fluctuations. Between 140.0 feet to the bottom of the log (145.7 feet), a linear decrease was measured from 14 Ω m to 13.8 Ω m. It should lastly be noted that this linear decrease between 140.0 feet and 145.7 feet falls near a point on the caliper log that suggests a major fracture is present at 143.9 feet. No other significant changes in slope were identified within the temperature log.

Heat Pulse Flow Meter

Nine depth locations were selected to collect HPFM samples: 107.0 feet, 108.9 feet, 111.1 feet, 113.9 feet, 118.0 feet, 126.0 feet, 131.0 feet, 140.0 feet, and 144.0 feet, respectively. All sample locations were selected based on major deflection points observed on the caliper log. A scale of -0.1 to 0.1 gpm was used for this log. HPFM sample collected at 107.0 feet displayed very low flow conditions, where the data indicate only minute upward flow of .015 gpm. The second sample location at a depth of 108.9 feet also indicated very low flow conditions, where a minute downward flow was detected at a rate of -0.15 gpm. Very strong downward flow was detected at the third sample location which was at a depth of 111.1 feet. Strong downward flow was detected and was measured at -0.1 gpm. Similarly, the sample collected at 113.9 feet further indicated strong downward flow of the same magnitude.

A critical measurement at 118.0 feet indicates that very strong upward flow exists and is occurring at a rate of 0.1 gpm. It should be noted that a significant deflection on the caliper log was recorded at a depth of 116.8, suggesting that strong downward flow is occurring above the caliper deflection, and strong upward flow is occurring below the caliper deflection. This combination of responses is typically indicative of a thieving zone—a point at which water is exiting a fracture or void space within the subsurface. Slight upward flow was measured at 126.0 feet and again at 131.0 feet, where both sample locations were measured at 0.05 gpm. Lastly, two more sample locations were sampled at depths of 140.0 feet and 144.0 feet, respectively. Both sample locations indicated very strong upward flow and with measurements of 0.1 gpm. It should be noted that this zone

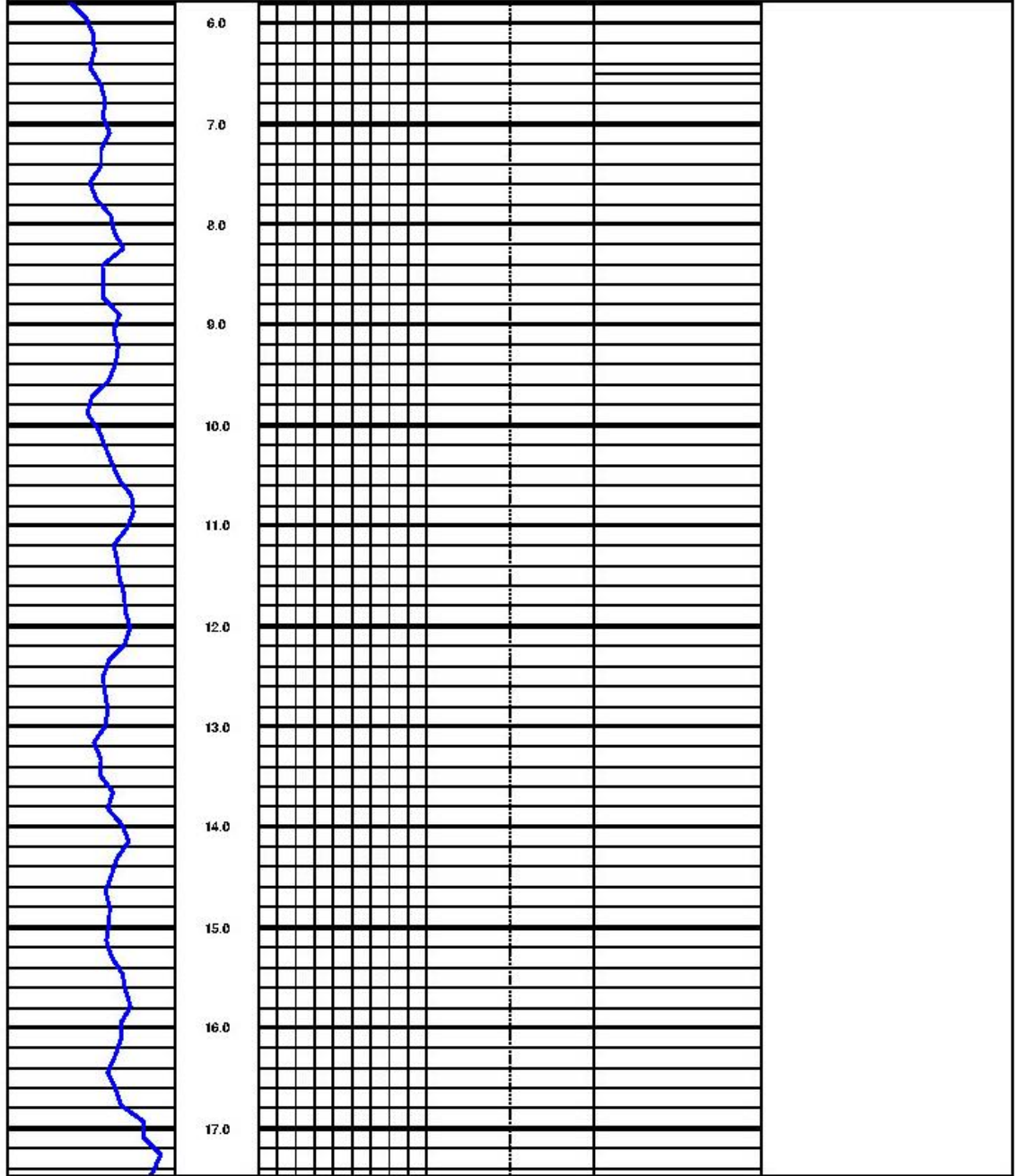
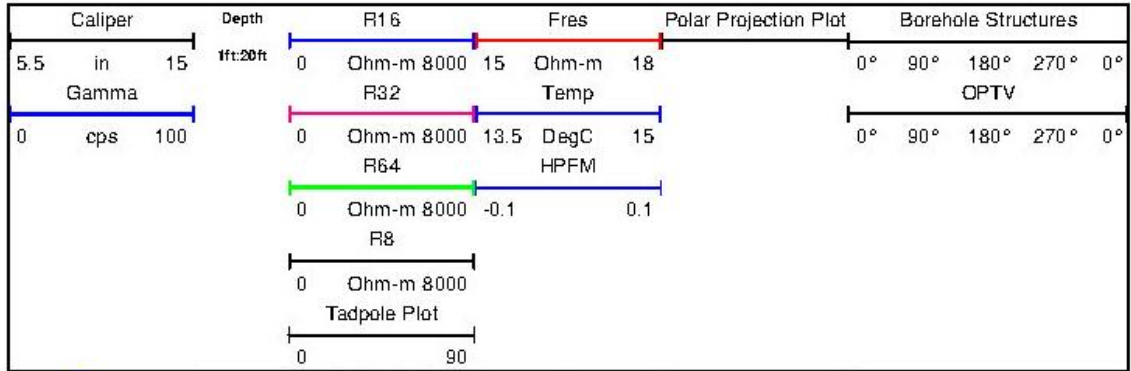
of upward flow is occurring near a notable major fracture observed on the caliper log. This may suggest that the water may be entering the borehole at a depth of 144.0 feet, moves vertically up the borehole, and exits at a depth of 116.8 where a major change in slope was observed on the caliper log.

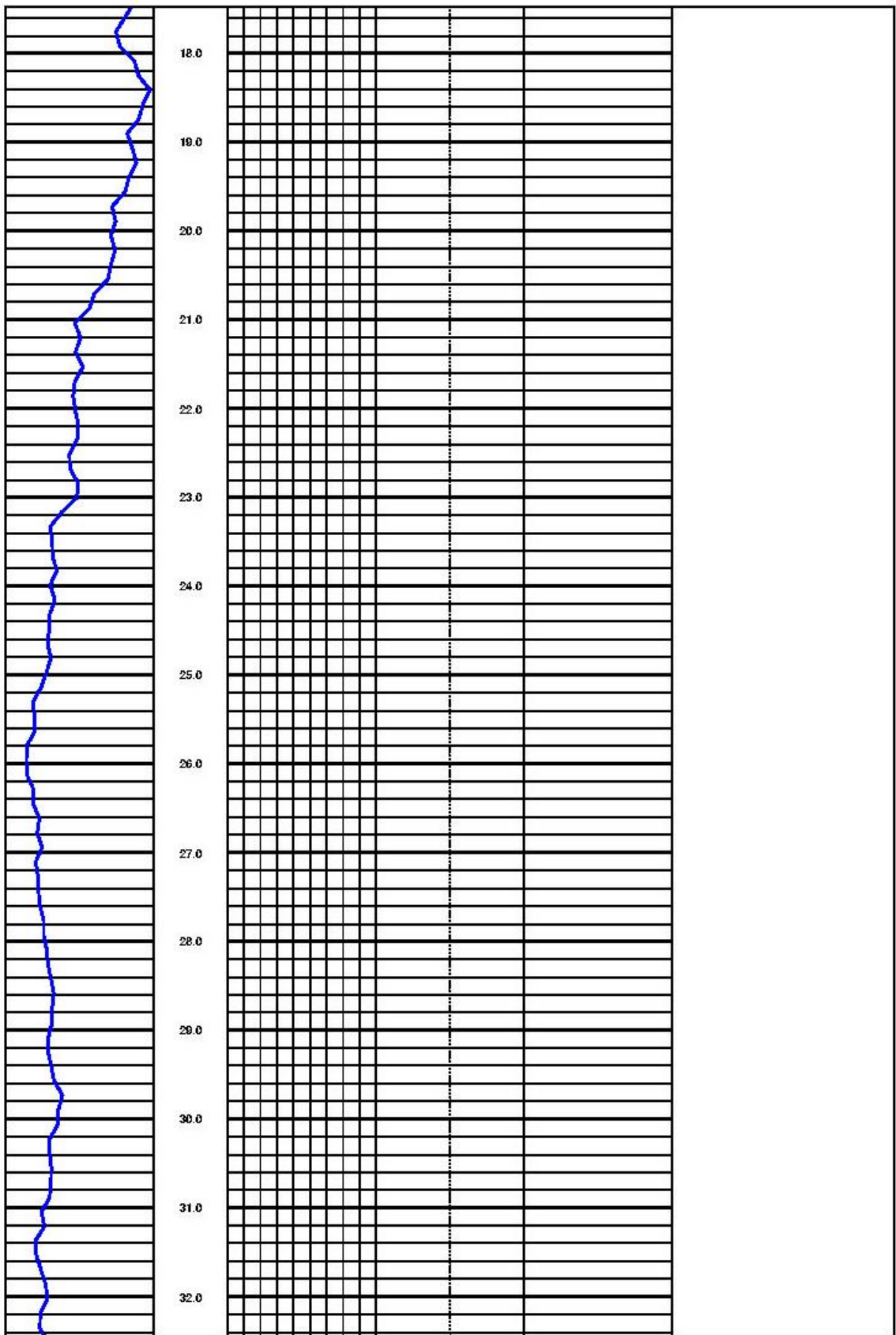
Optical Televiewer

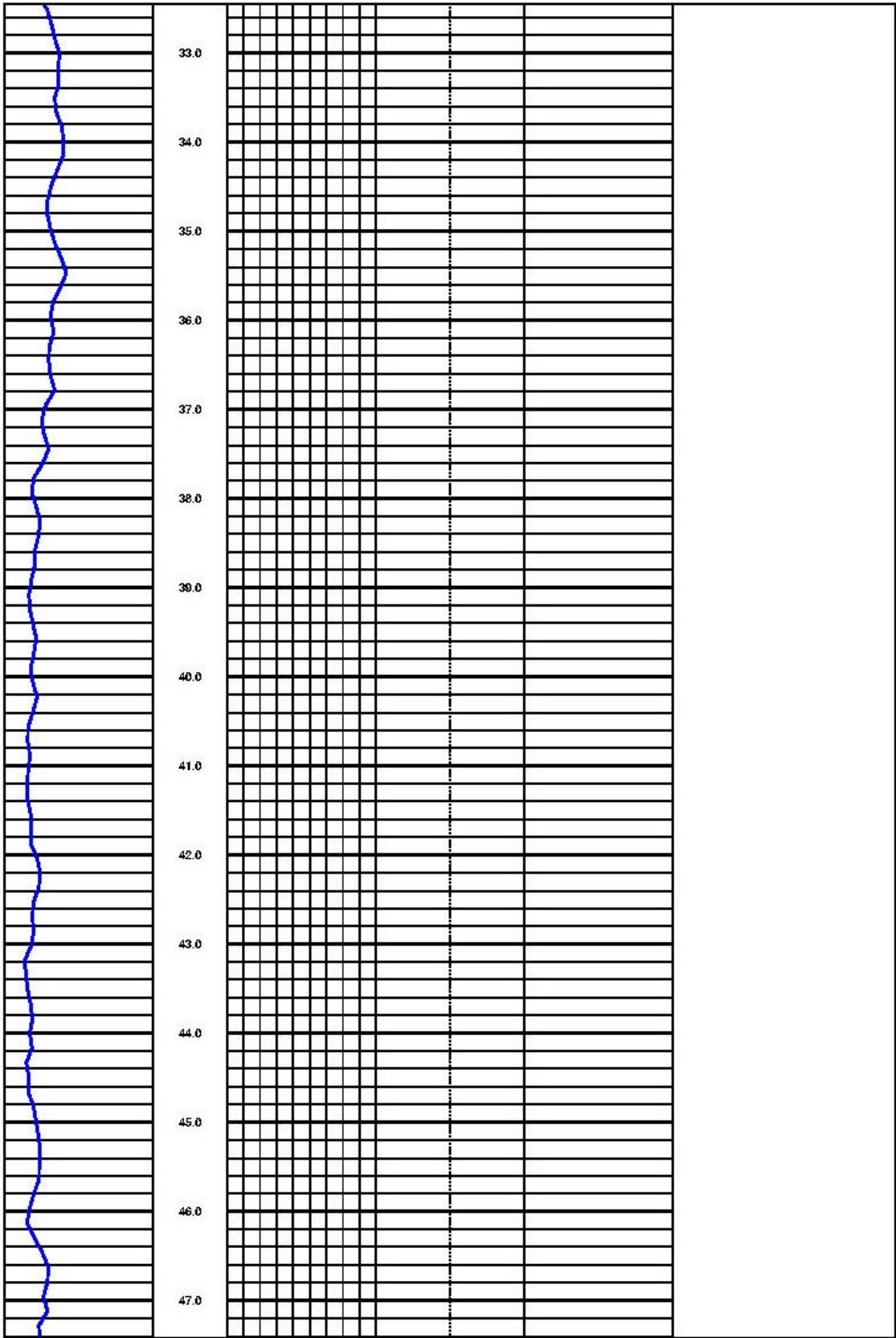
Identified features from the OPTV log include bedding features, minor fracture, major fractures, in-filled fractures, and the presence of a significant void space. In general, the bedding features had predominant dip directions to south-southeast and dip angles between 41 degrees and 70 degrees, with a mean average of 57 degrees. Similarly, minor fractures observed on the log also showed a predominate dip direction to the southeast with the exception of several outliers with dip directions to the northeast, or 180 degrees from common directions. Dip angles for minor fractures ranged from 44 degrees to 67 degrees, where higher angles are associated with those minor fracture with dip directions to the northwest. Similarly, in-filled fractures have a predominant dip direction to the northwest and occur at high angles which range from 63 degrees to 71 degrees.

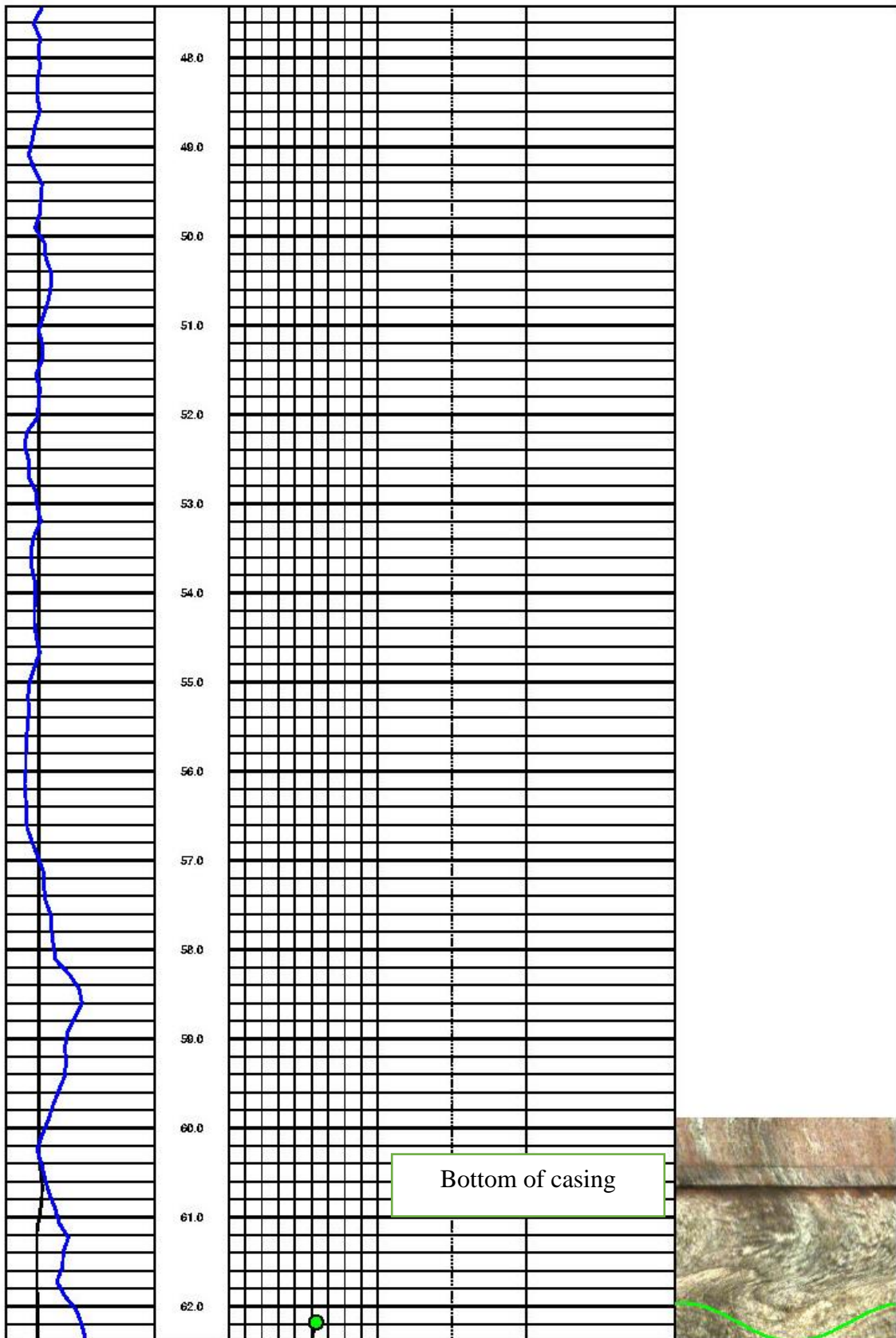
The most notable features are the presence of a significant void space at a depth range of 116.0 feet to 117.6 feet and correlates with a major deflection point on the caliper log. This void space is the likely exit point (or thieving zone) identified within the HPFM log. Another significant feature observed in the OPTV is a major fracture that occurs between 119.2 feet to 124.2 feet. This fracture dips to the north at a near vertical angle. Additionally, the broad, subtle nature of the caliper log occurs throughout the same zone

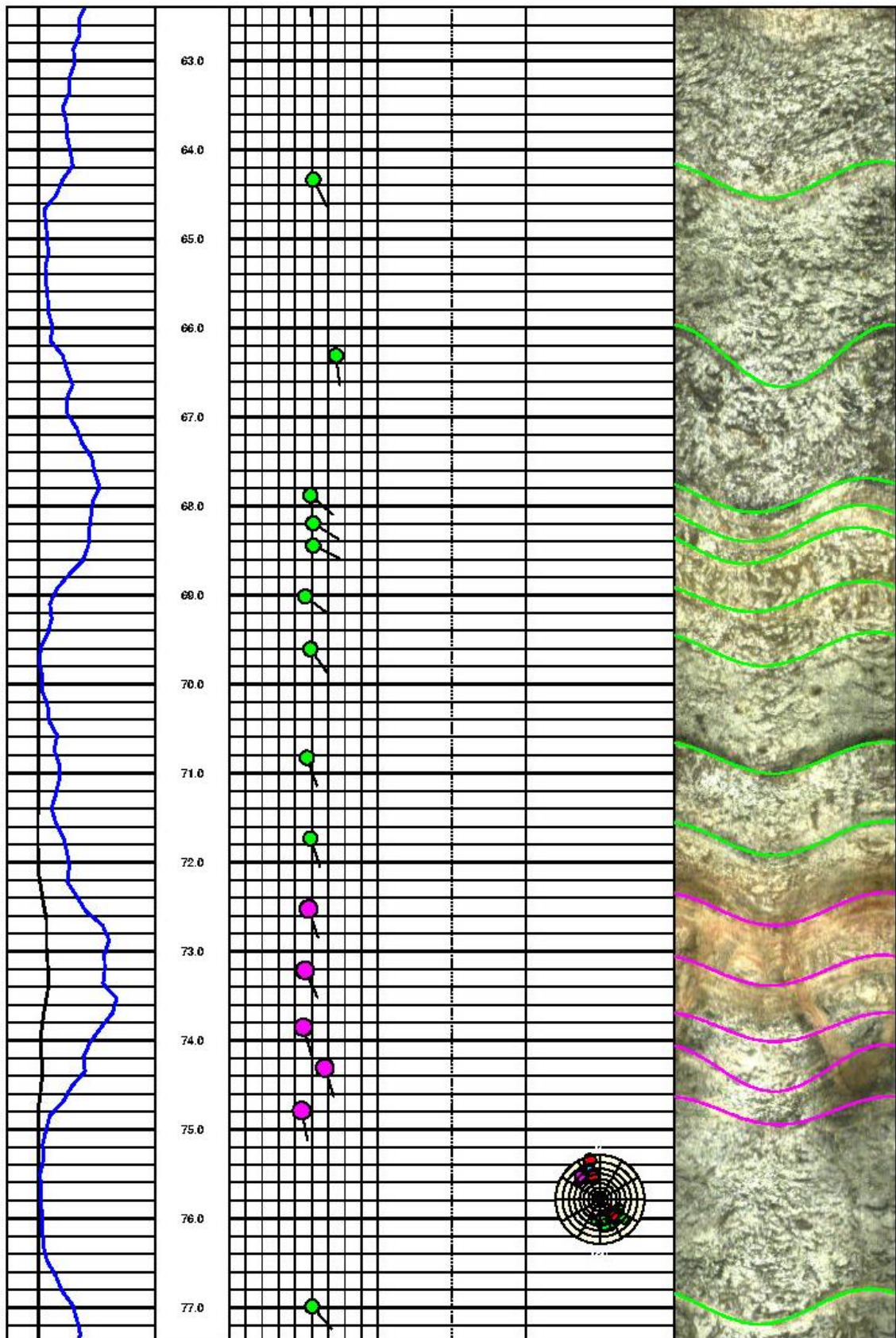
and is expressing the near vertical nature of the fracture dip angle as observed on the OPTV log. Another major fracture was observed at a depth of 129.0 feet and occurs at the same depth as a deflection on the caliper log. Lastly, a third and significant fracture was observed at a depth of 144.0 feet and further agrees with a deflection observed on the caliper log.

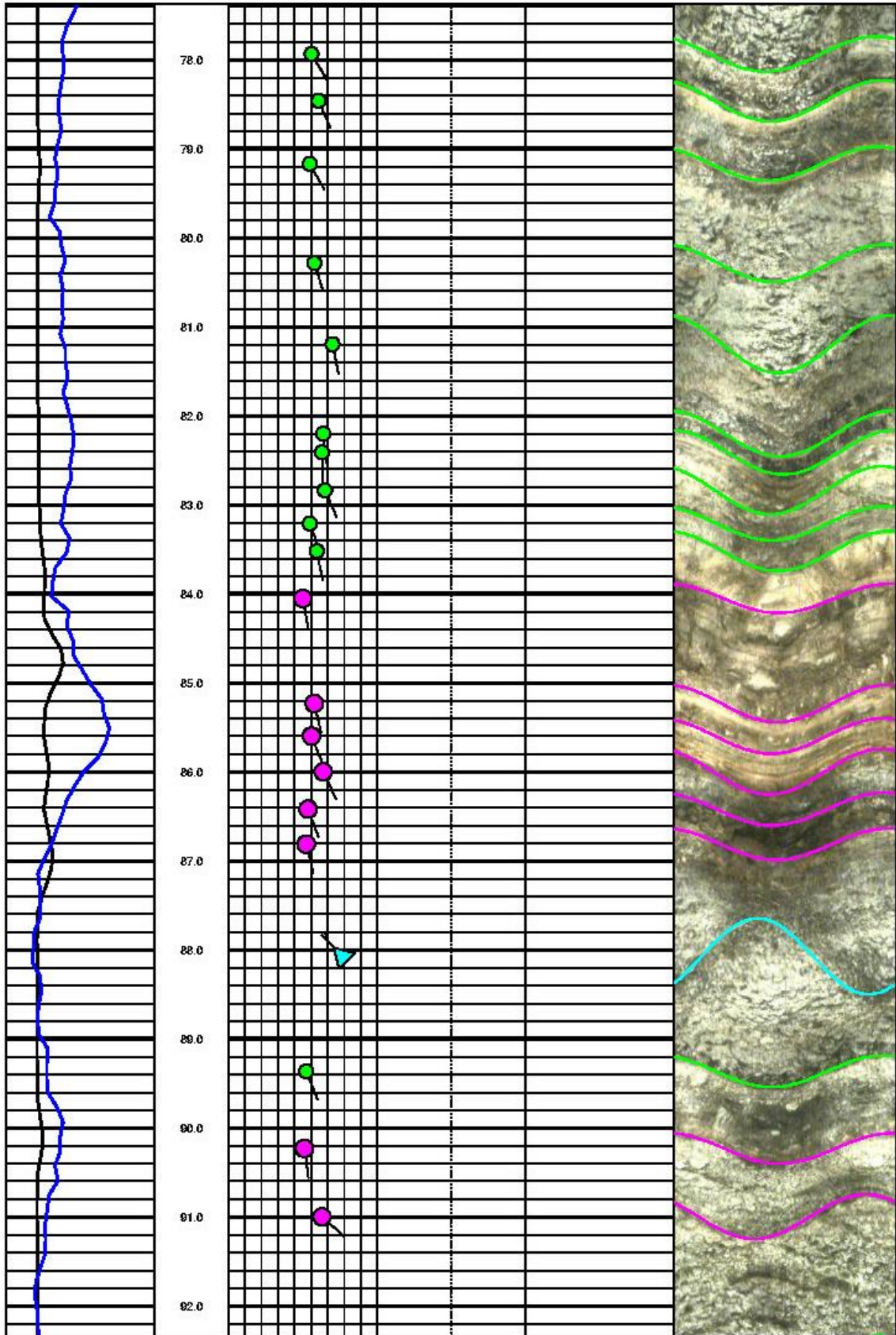


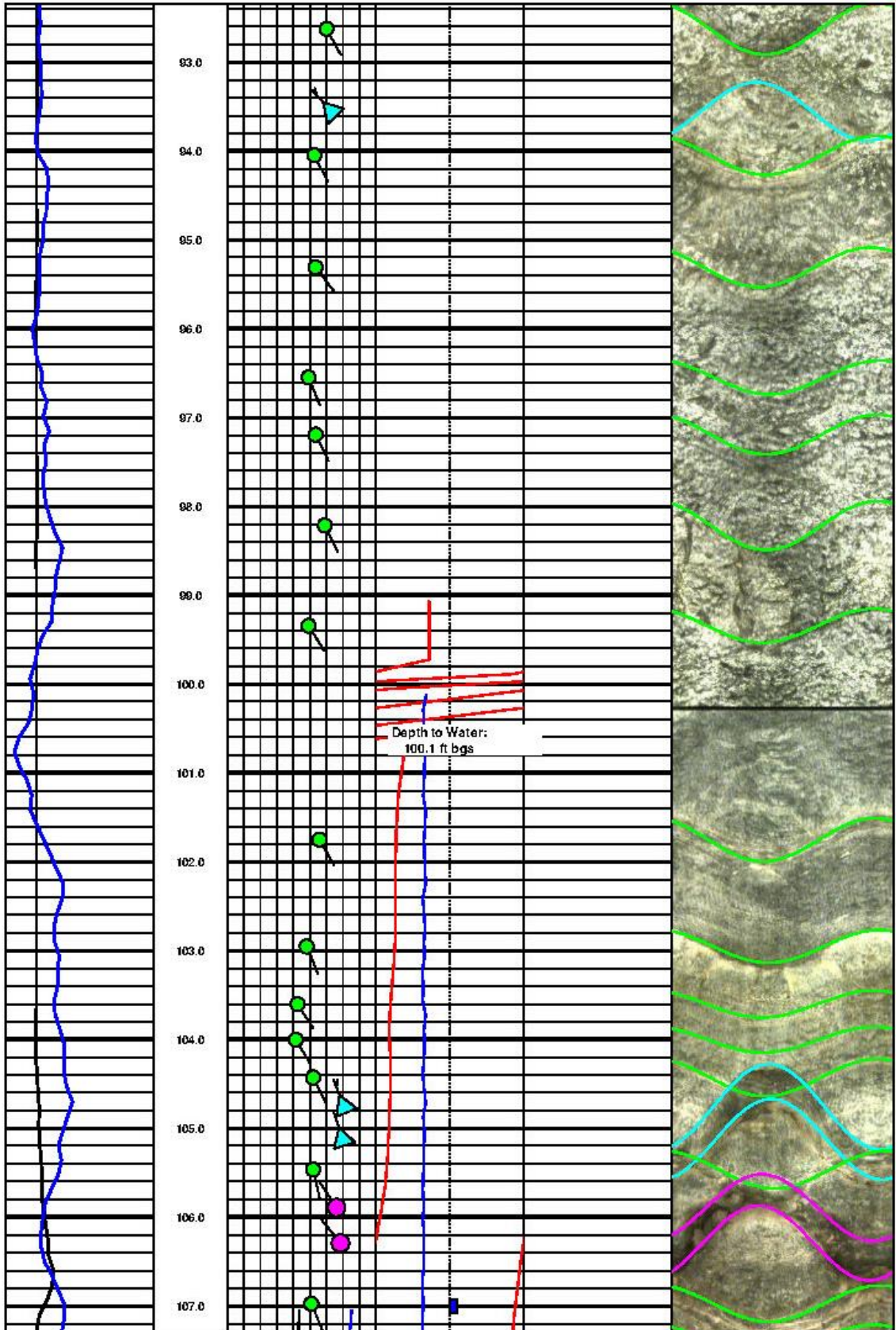


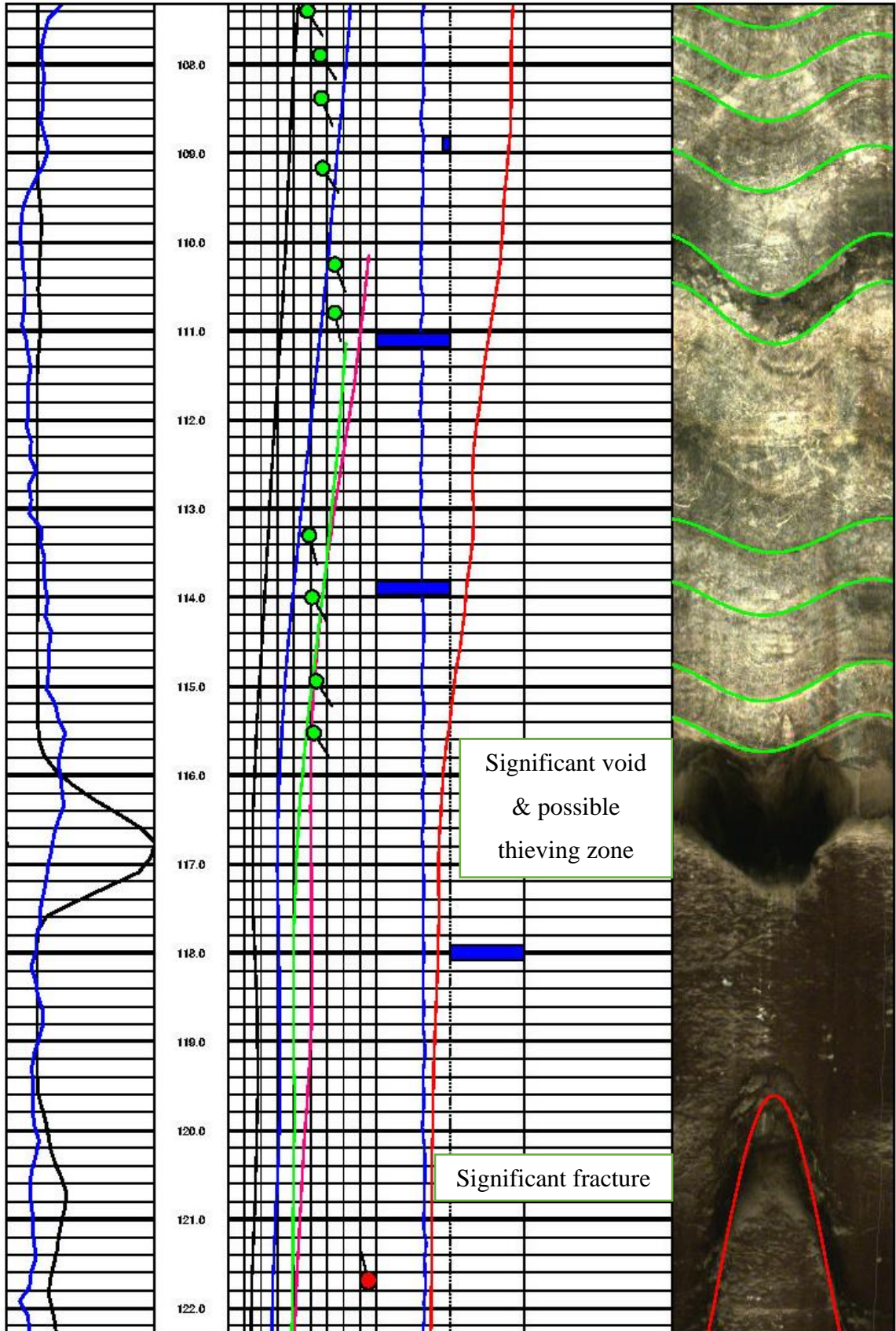


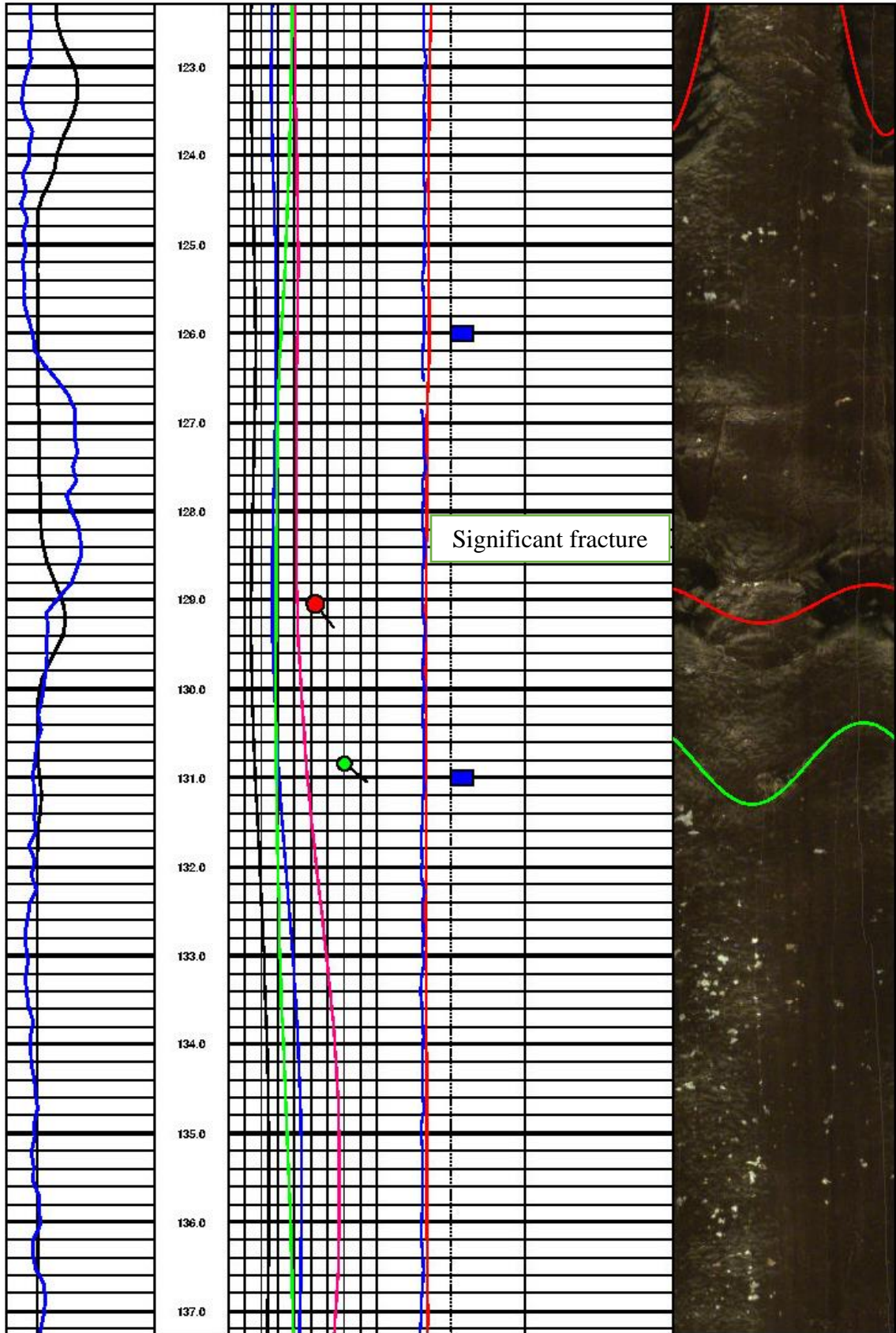












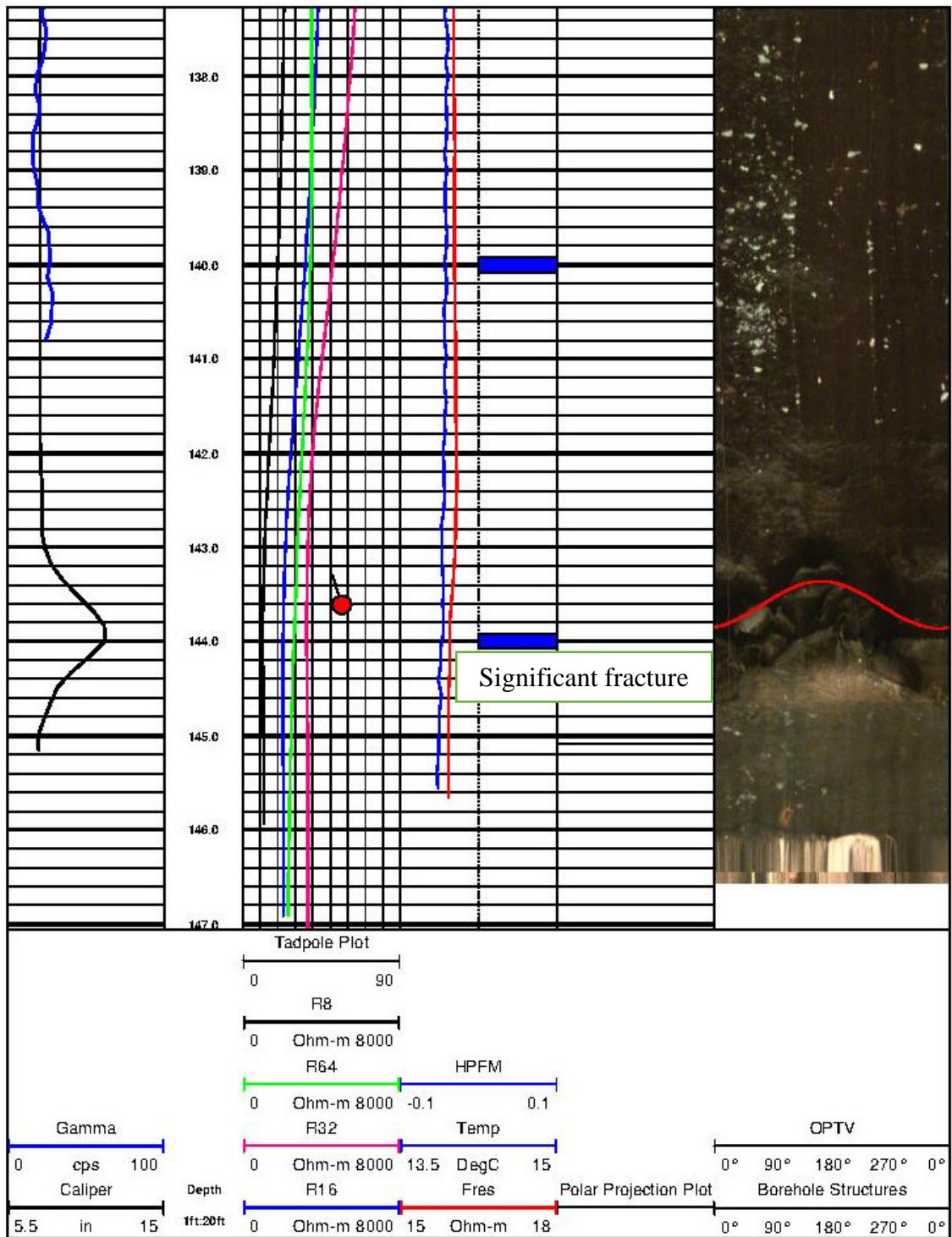


Figure 6.7 MW-19 well log results

Table 4: MW-19 Bedrock Structures

Depth (feet)	Dip Direction (degrees)	Dip Angle (degrees)	Comments
62.1	192	53	BP
64.3	152	51	BP
66.3	172	65	BP
67.9	130	49	BP
68.1	122	51	BP
68.5	114	51	BP
69.0	126	46	BP
69.6	145	49	BP
70.8	160	47	BP
71.7	161	49	BP
72.5	161	48	MF
73.2	155	46	MF
73.8	164	45	MF
74.2	162	58	MF
74.7	169	44	MF
77.0	138	50	BP
77.9	149	50	BP
78.4	156	54	BP
79.2	149	49	BP
80.3	162	52	BP
81.2	169	63	BP
82.1	173	57	BP
82.4	178	57	BP
82.8	156	59	BP
83.2	159	49	BP

Table 4 (continued.): MW-19 Bedrock Structures

Depth (feet)	Dip Direction (degrees)	Dip Angle (degrees)	Comments
83.5	169	54	BP
84.0	170	45	MF
85.2	165	52	MF
85.6	157	50	MF
85.9	154	57	MF
86.4	159	48	MF
86.8	166	47	MF
88.0	315	69	IFF
89.3	158	47	BP
90.2	172	46	MF
91.0	130	57	MF
92.6	152	60	BP
93.4	318	63	IFF
94.0	152	53	BP
95.3	142	54	BP
96.5	158	49	BP
97.2	153	54	BP
98.1	153	59	BP
99.4	148	49	BP
100.2			DEPTH TO WATER
101.7	150	56	BP
102.9	157	48	BP
103.6	147	53	BP
104.0	149	41	BP
104.4	152	52	BP

Table 4 (continued)

Depth (feet)	Dip Direction (degrees)	Dip Angle (degrees)	Comments
104.7	337	71	IFF
105.0	342	70	IFF
105.4	167	52	BP
105.9	326	66	MF
106.2	320	67	MF
106.9	157	51	BP
107.4	148	48	BP
107.9	146	56	BP
108.4	158	57	BP
109.2	147	57	BP
110.3	159	65	BP
110.8	168	65	BP
113.3	165	49	BP
114.0	149	51	BP
115.0	147	54	BP
115.5	148	52	BP
116.5			SIGNIFICANT VOID/THEIVING ZONE
121.7	346	85	SIGNIFICANT FRACTURE
129.1	141	53	SIGNIFICANT FRACTURE
130.9	128	70	BP
143.5	344	57	SIGNIFICANT FRACTURE

CHAPTER 7

DISCUSSION

7.0 ERI Interpretations

As Forward Model 3 predicted, the LNAPL plume itself was not measurable using the dipole-dipole resistivity measurement in-situ, and is a function of both loss of resolution in ERI responses with increasing depth and the large range in resistivity values which exist in geologic materials. The forward model was constructed with a slight bias on the LNAPL plume thickness within the rock matrix which favored for a greater chance of detection, where the modeled plume still was undetected even with favorable geometries. Likewise, there is no variation in geophysical responses that would suggest LNAPL contamination within the documented plume area. Although the LNAPL plume was not directly detected in the field, the data provided insight into likely pathways for LNAPL movement within the subsurface.

In general, the ERI lines showed two, roughly linear and repeating, very low resistivity zones (FZ-1 and FZ-2 above) that likely represent the upper, vertical to near vertical, expressions of a thrust fault. These two low resistivity zones bracket the documented USGS thrust fault and further provide much greater resolution which may perhaps indicate a significant, undocumented secondary fault zone. Although a well-pronounced and notable feature observed in several resistivity profiles, the northernmost low resistivity zone identified as FZ-1 has been mapped significantly outside of the documented LNAPL plume and was not likely a contributing factor to plume migration at

the site. FZ-2, however, is the other significant low resistivity zone that has been interpreted as a suspected primary preferential pathway for both vertical and horizontal groundwater movement and plume migration. This very broad, low resistivity zone indicates a likely preferential pathway from near surface to the bottom of the profiles on Line 1 through Line 3. Although the characteristic of FZ-2 varies from a high angle orientation in the southwest to more vertically oriented to the northeast, it is a continuous and predominant feature observed across the entirety of the survey area that correlates with the approximate center of the LNAPL plume migration map. This would suggest that FZ-2 is the most likely structural geologic feature that would influence the northeasterly plume migration away from the sources to the southwest.

Another interpretation made from this study is that the LNAPL plume boundary falls at a key point of high resistivity along the eastern half of Line 5 which may indicate more competent rock is present and would act as more resistive path for porewater fluid movement; this is coupled with the change in apparent dip in bedrock on the eastern half of Line 6. Additionally, Line 4 shows that FZ-2 becomes much narrower and slightly more resistive than Line 1 through Line 3, further indicating that groundwater and plume movement may be constrained by these more resistive zones. The general trend in bedding and fractures identified in bedrock wells further supports the likely movement to the east-northeast, suggesting plume migration is occurring along interpreted trends of the fault strike. The resistivity data show that a general and shared higher resistivity characteristic was measured on both Line 5 and Line 6 along the apparent fault strike which straddles

the approximate plume boundaries on its northern and southern extents. With observing the lower resistivity zones identified perpendicular to the anticipated strike along FZ-2, it is possible that that these zones of higher resistivity from Line 5 and Line 6 force both groundwater and plume movement along the anticipated strike of the interpreted FZ-2 to the northeast near MW-20, where the northeastern-most extent of contamination was documented. It should be restated at this point that the LNAPL plume map is based on the data obtained from nearby bedrock wells. This is important because of the combination of the apparent change in orientation of FZ-2 along Line 4 near MW-20 to the northeast and may explain why no LNAPL was recovered in either MW-17 or MW-20. Figure 7.1 below uses imperial units as SI units are unavailable from NJGIN.

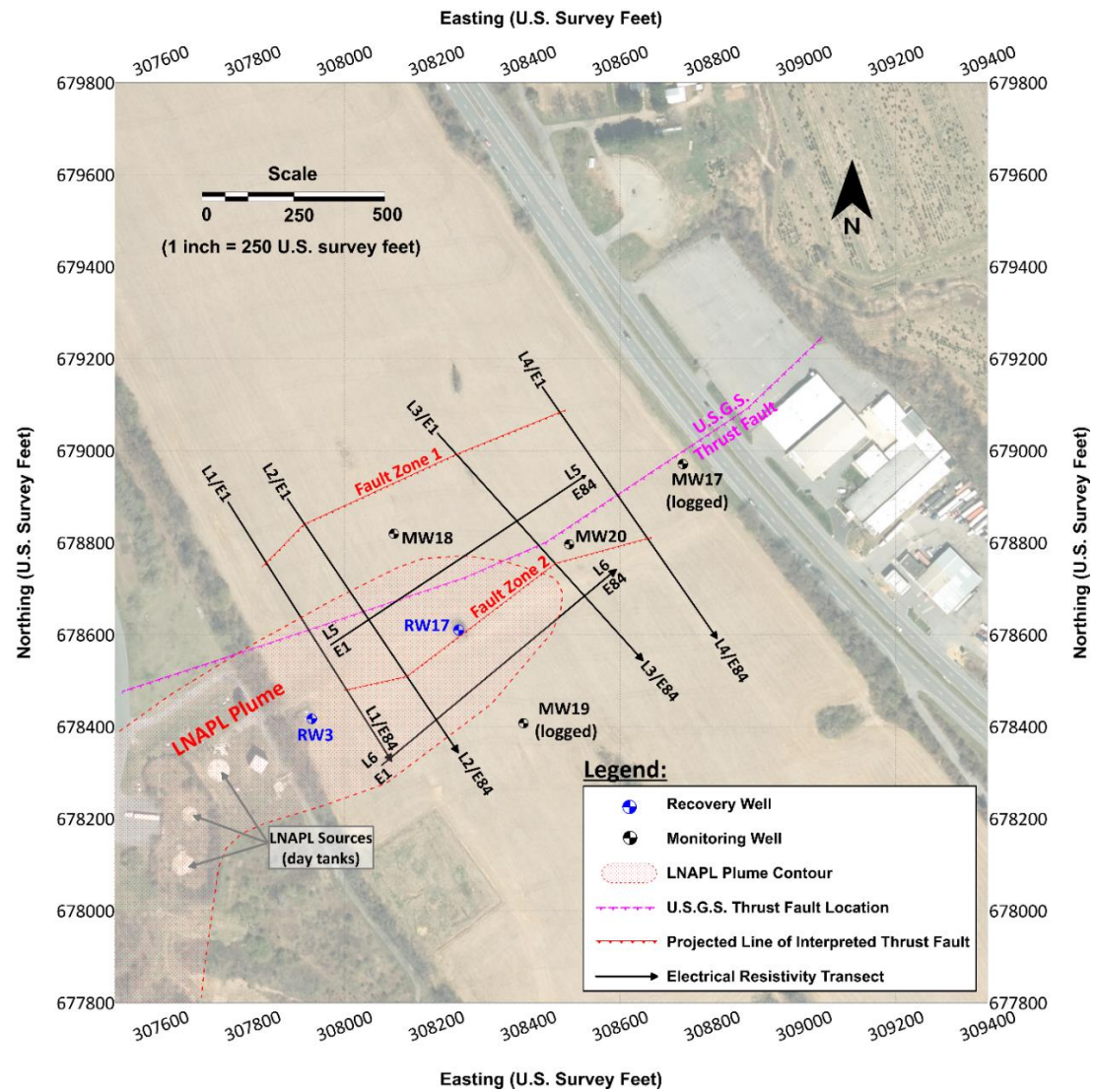


Figure 7.0 Projection of interpreted thrust faults relative to LNAPL plume (modified from NJGIN, 2012).

7.1 Borehole Geophysical Data Interpretations

In general, MW-17 (Figure 7.0) did not display major fracturing or any major variations in caliper responses throughout the log. The OPTV log further indicated the same result but provided additional finer detail in terms of bedding features and in-filled fracturing for which structural data have been described in further detail below. As predicted from previous log data, bedding features and minor open fractures predominantly dip to the southeast at steep angles, while in-filled fractures roughly have strikes which are almost 180 degrees (or northwesterly trending) from bedding and minor open fracture features. In-filled fractures typically had greater dip angles, suggesting they are steeper in nature.

In terms of lithology, no major variation was observed in the electric logs, which would suggest a cohesive unit throughout the log (e.g. a massive, bedded dolomite). The HPFM meter indicated a low-to-no flow environment at the sampled locations within the borehole. As described previously in section 3.8, the HPFM sample locations were based on a pre-determined interval and noted fractured sections during the optical televiewer investigation. Based on the results of the logs, MW-17 appears to show that the surrounding rock is relatively competent and contains very low flow conditions at the sampled locations. Lastly, the logs agreed with depth-to-bedrock interpretations made from the ERI profiles and showed similar values in terms of resistivity responses from the 8, 16, 32, and 64-inch resistivity measurements when compared to the surface ERI responses.

The measured features from MW-19 are relatively similar to both the predicted results of previous well log data and to those characteristics identified in OPTV data from MW-17. Bedding features and minor fracturing was observed on the caliper and OPTV logs throughout the depth of the well; however, several significant additional features were identified such as a significant void and associated thieving zone at 116.8 feet, and a series of major fractures that are present at depths of 121.6 feet, 129.2 feet, and 144.0 feet, respectively. The caliper response in the vicinity of the void space is well off-scale, suggesting that the void space is significantly wider than the surrounding borehole. A significant variation in the HPFM response both above and below this void was measured. HPFM measurements were taken directly above and below the void space to determine localized vertical flow movement. As the results indicate, significant downward flow is present above the void, and significant upward flow is present below the void. This response suggests that this void has an associated thieving zone, where groundwater is exiting the borehole at this specific location. Additionally, an upward trending flow was observed from two measured fractures below this void, suggesting that groundwater below the void is moving up to, and out of, the identified void. MW-19 contains a greater abundance of major fractures and presence of a void space, but generally agrees with the overall southeasterly trending dip directions with moderate dip angles. The difference in structural features identified in MW-19, when compared to MW-17, indicate the complex nature of a dolomitic environment and show how complex groundwater movement can be in this type of geologic setting.

CHAPTER 8

CONCLUSIONS

8.0 Summary of Work

The primary objective of this research was to test the hypothesis that the USGS documented thrust fault has influenced LNAPL migration by using electrical resistivity imaging (ERI) and suite of downhole geophysical measurements. This research also tests the hypothesis that direct detection of LNAPL contamination through the use of ERI measurements alone is not likely, but can aid in planning conventional drilling and sampling events. To test these hypotheses, direct current (DC) resistivity data were collected using the dipole-dipole electrode configuration and were complemented with a suite of downhole geophysical probes including an optical televiewer, three arm caliper, multi-parameter resistivity probe, and heat pulse flow meter. Geophysical responses were then compared to geologic logs, geologic maps, and LNAPL plume maps obtained from the prior work associated with ongoing remediation efforts. Interpretations of the combined datasets were then made to determine the most plausible route of which the documented LNAPL plume has migrated from its source based subsurface structural characteristics identified in the geophysical datasets. Structural geologic features such as faults, fractures, variations in bedrock topography, and general orientation of bedrock structures may have influenced the way in which a documented LNAPL plume were observed using both surface and downhole geophysical approaches. Four of the ERT lines indicated very low resistivity values in a roughly linear orientation across the study area that are coincident with both an anticipated and previously unknown fault zones. Additionally, the northern and southern boundaries of the LNAPL plume appear to be constrained by more competent

rock observed on ERI line 5 and line 6. The optical televiewer provided evidence of apparent (southwest-to-northeast trending) strike and dip orientation of the major fractures, which were corroborated by caliper data. The heat-pulse flow meter data revealed a wide variation in vertical flow rates that are typical of karst environments. To test the direct detection hypothesis, a forward model was generated in the lab using the same parameters as the field investigation. The end results show that neither the forward model nor field models predicted direct detection was possible and is a function of loss of resolution or dipole-dipole measurements with depth and the large range of resistivity values that exist in common geologic material.

Based on the results of this study, a combination of dipole-dipole ERI, optical televiewer, caliper, and heat pulse flow meter methods provided the most valuable measurements as they relate to the fault-transport hypothesis. ERI cross-sections were generated from dipole-dipole ERI data which displayed a linear, significantly low resistivity zone that has been interpreted as a shallow, near vertical expression of a thrust fault which had an apparent influence on LNAPL migration. Borehole geophysical data from the optical televiewer, caliper, and heat pulse flow meter provided substantial information in terms of strike and dip of fractures and bedding features. The heat pulse flow meter showed how drastically vertical flow can change across this site, as indicated by the potential thieving zone identified in MW-19 and lack of features observed in MW-17. Of the borehole instrumentation, the least helpful data for this investigation was the formation resistivity measurements, as no major variations in lithology were encountered.

8.1 Future Work

To further refine subsurface structural characteristics at this site, additional ERI lines spaced in closer proximity to existing datasets would allow for even greater spatial resolution of identified fault zones and more subtle features such as fractures. Additional ERI data would also allow for the generation of three-dimensional models. The three-dimensional ERI models could be used to further define bedrock characteristics and fault geometries and in particular how the fault geometries relate to plume migration. The collection of ERI data over repeat transects of either two or three-dimensional models could be applied to generation of four-dimensional models, where variations of subsurface characteristics could be observed over time.

The shallow, near surface expressions of the faults observed in this research shows that the Ingersoll Rand Site is an ideal facility for examining the ability of other geophysical approaches to analyze fault influence on contaminant transport and fate. Additional methods that could be used to corroborate or enhance the results of this research include the multichannel analysis of surface wave (MASW) seismic method or microgravity (MG) method. The MASW and MG measurements could be collected along the identical ERI transects as used in this research to identify variations in respective measurements that correspond to the interpreted fault locations. For example, the MASW method should indicate a significant low velocity zone where FZ-1 and FZ-2 are present as a result of the attenuation of surface wave velocities through a less dense medium. Additionally, the MG method should indicate a gravitational low in FZ-1 and FZ-2 as a result of mass deficiency, or lack of rock, where openings are present in bedrock as a result of faulting.

As with any geophysical method, it is critical to relate the results of a geophysical investigation to tangible subsurface features, as was demonstrated in this research through observations made in bedrock wells, specifically in wells MW-17 and MW-19. To further support geophysical data collection efforts, additional bedrock wells could be installed and sampled to obtain more information on lateral extents of LNAPL plumes. This research shows how valuable dipole-dipole ERI and borehole geophysical data are for imaging subsurface structural characteristic at LNAPL contaminated sites; it has also shown that direct detection of LNAPL contamination is not likely under similar conditions at other sites. Most importantly, the ERI and borehole geophysical data collected at this site shows how valuable it can be for remediation efforts, specifically in terms of extraction and bedrock recovery well siting. Additional recovery wells placed in strategic locations based on this research may provide for a more effective remediation of the LNAPL contamination. It is hoped that this research can be used as a resource in future remediation projects at LNAPL contaminated, fractured rock sites.

REFERENCES

- Abdullah, W., Neyamadpour, A., Neyamadpour, B., and Taib, S., 2010, Comparison of Wenner and Dipole-Dipole Arrays in the Study of an Underground Three-Dimensional Cavity: *Journal of Geophysics and Engineering*, v.7, no.1. doi: 10.1088/1742-2132/7/1/003.
- Acree, S.D., Huling, S.G., Newell, C.J., and Ross, R.R., 1995, Ground Water Issue, Light Nonaqueous Phase Liquids; United States Environmental Protection Agency, EPA/540/S-95/500.
- Adams, A., Beck, B., and Zhou, W., 2002, Effective Electrode Array in Mapping Karst Hazards in Electrical Resistivity Tomography: *International Journal of Geosciences*, v. 42, p. 922-928. doi: 10.1007/s00254-002-0594-z.
- Advanced Geosciences, Inc. (AGI), 2018, SuperSting User Manual, AGI, Austin, TX.
- Advanced Logic Technology, n.d., Optical Televiewer, Tool Design and Philosophy: www.alt.lu/optical_televiewer.htm (accessed October 2017).
- Apel, D., Hall, R., and Khorzoughi, M., 2017, Rock Fracture Density Characterization Using Measurement While Drilling (MWD) Techniques: *International Journal of Mining Science and Technology*, p. 2-9. doi: 10.1016/j.ijmst.2018.01.001.
- Atekwana, E., Sauck, W., and Werkema, D., 2000, Investigations of Geoelectrical Signatures at a Hydrocarbon Contaminated Site: *Journal of Applied Geophysics*, v. 44, p.167-180. doi: 10.1016/S0926-9851(98)00033-0.
- Beck, B., Stephenson, J., and Zhou, W., 1999, Reliability of Dipole-Dipole Electrical Resistivity Tomography for Defining Depth to Bedrock in Covered Karst Terranes: *International Journal of Geosciences*, v. 39, p. 760-766.
- Bradbury, S., and Muldoon, M., 2001, Correlation of hydraulic conductivity with stratigraphy in a fractured-dolomite aquifer, northeastern Wisconsin, USA: *Official Journal of the International Association of Hydrogeologists*, v. 9, p. 570-583. doi: 10.1007/s10040-001-0165-5.
- Cabrera, J., Cushing, M., De Hoyos, A., Gelis, C., Jougnot, D., Lemeille, F., Rocher, M., 2010, Potential of Electrical Resistivity Tomography to Detect Fault Zones in Limestone and Argillaceous Formations in the Experimental Platform of Tournemire, France: *Pure and Applied Geophysics*, v. 167, p. 1405-1418.
- Chu, A., Monti, J., and Stumm, F. 2004, Delineation of faults, fractures, foliation, and ground-water-flow zones in fractured-rock, on the southern part of Manhattan, New

York, through use of advanced borehole-geophysical techniques, USGS Open-File Report - 1232, 10: <https://pubs.USGS.gov/of/2004/1232/ofr20041232.pdf> (accessed October 2017).

Craig, H.R., 1996, Karst Topography – A General Overview. In Karst Geology of New Jersey and Vicinity, *in* Thirteenth annual meeting of the Geological Association of New Jersey, Whippany, NJ, R.F. Dalton and J.O. Brown, eds., p. 1-19.

Crowner, R., Hess, A., and Paillet, F., 1996, High-Resolution Flowmeter Logging Applications with the Heat-Pulse Flowmeter.: Society of Exploration Geophysicists, v. 1 p. 1-11. doi: 10.4133/JEEG1.1.1.

Dalton, R., 2003, Physiographic Provinces of New Jersey: <http://www.nj.gov/dep/njgs/enviroed/infocirc/provinces.pdf> (accessed October 2017).

Drake, A. A., 1967, Geologic Quadrangle Map, Easton Quadrangle, NJ – PA, United States Geological Survey: <https://digital.libraries.psu.edu/digital/collection/pageol/id/52134> (accessed October 2017).

ENSR, 2005. Groundwater Remedial Investigation Report. PI# 03710-162A.

ENSR, 2004. Site History Report. PI# 03710-162B.

Geosyntec Consultants, Inc., 2015. Remedial Investigation Report / Remedial Action Workplan. PI# 012833.

Google Maps, 2017, <https://www.google.com/maps/place/Alpha,+NJ+08865/@40.6577473,-75.1892535,13z/data=!3m1!4b1!4m5!3m4!1s0x89c46d60f87558b9:0xede2231b17ba6194!8m2!3d40.6670439!4d-75.1573972> (accessed October 2017).

Haeni, F., Johnson, C., Lane, J., and White, E., 2002, Borehole-Geophysical and Hydraulic Investigation of the Fractured Rock Aquifer near the University of Connecticut Landfill, Storrs, Connecticut: USGS Water Resources Investigation Report, 2000 to 2001: <https://pubs.USGS.gov/wri/2003/4125/report.pdf> (accessed October 2017).

Harvard University School of Engineering and Applied Sciences, Ohm's Law, 1998: http://people.seas.harvard.edu/~jones/es154/lectures/lecture_2/Ohm%27sLaw/Ohm%27sLaw.html (accessed March 2018).

Herman, R., 2001, An Introduction to Electrical Resistivity in Geophysics: Department of Chemistry and Physics and Department of Geology, Radford University: American Journal of Physics, v.69, i.9, pp. 943-952, doi: 10.1119/1.1378013.

INCHEM, 2004. Diesel Fuel No. 2. Retrieved September 28, 2019, from <http://www.inchem.org/documents/icsc/icsc/eics1561.htm>.

Johnson, C. D., and Williams, J.H., 2004, Acoustic and Optical Borehole-Wall Imaging for Fractured-Rock Aquifer Studies: *Journal of Applied Geophysics*, v. 55, pp. 151–159. doi: 10.1016/j.jappgeo.2003.06.009.

Keys, W.S., 1997, *Borehole Geophysics Applied to Ground-Water Investigations*: Dublin, Ohio, National Groundwater Association.

Lehigh University Earth and Environmental Science, (2012). The Allentown Formation. Retrieved October 27, 2019, from https://www.lehigh.edu/~fjp3/srt/srt_geology.html.

Loke, M., 2000, *Electrical Imaging Surveys for Environmental and Engineering Studies: A Practical Guide to 2D and 3D Surveys*, <http://pages.mtu.edu/~ctyoung/LOKENOTE.PDF> (accessed October 2017).

Monahan, S.A., 2013, *Investigating Fault Structure Using Electrical Resistivity Tomography*: <http://digitalcommons.calpoly.edu/cgi/viewcontent.cgi?article=1093&context=physsp> (accessed March 2018).

Mount Sopris Instruments, 2017, QL40-CAL – 3-Arm Caliper: <http://mountsopris.com/items/ql40-cal-3-arm-caliper/> (accessed October 2017).

Mount Sopris Instruments, 2018, QL40-OBI-2G – Optical Televiewer: <http://mountsopris.com/items/ql40-obi-2g-optical-televiewer/> (accessed October 2017).

Muchaidze, I., 2008, *Imaging in Karst Terrain Using Electrical Resistivity Tomography [M.S. thesis]*: Missouri University of Science and Technology.

New Jersey Department of Environmental Protection (NJDEP), 1996: <https://www.state.nj.us/dep/njgs/geodata/dgs02-7.htm> (accessed September 2019).

New Jersey Department of Environmental Protection (NJDEP), 2016: <https://www.state.nj.us/dep/njgs/enviroed/freedwn/psnjmap.pdf> (accessed October 2018).

New Jersey Department of Environmental Protection, 2017, *Bedrock and Surficial Geology, Gravity, Magnetic, Aquifers, Landslides, Mines, Quarries, Earthquakes and Physiographic Provinces Maps of New Jersey*, <https://www.nj.gov/dep/njgs/NJMaps.pdf>. (accessed October 2019).

New Jersey Geographic Information Network (NJGIN), 2012, *NJGIN Information Warehouse*: https://njgin.state.nj.us/NJ_NJGINExplorer/IW.jsp (accessed May 2018).

New Jersey Geological Survey, Department of Environmental Protections, 1998, Aquifers of New Jersey: <https://www.state.nj.us/dep/njgs/pricelst/ofmap/ofm24.pdf> (accessed October 2019).

Pezard, A.P., and Yeh, E.C., 2007, Borehole Imaging Tools - Principles and Applications: Scientific Drilling, p.2, doi: 10.2204/iodp.s.d.5.07S1.2007.

Reynolds, J., 2011, An Introduction to Applied and Environmental Geophysics (2nd ed.): Chichester, West Sussex, UK, John Wiley and Sons, Ltd, p.292-293.

Robinson, E.S., 1988, Basic Exploration Geophysics, p. 445-478.

Stone, B. D., Stanford, S. D., and Witte, R. W., 2002, Surficial Geologic Map of Northern New Jersey, United States Geological Survey: <https://pubs.er.USGS.gov/publication/i2540C> (accessed October 2017).

United States Environmental Protection Agency (U.S. EPA) Robert S. Kerr Environmental Research Laboratory, 1991, Dense Nonaqueous Phase Liquids – A Workshop summary, Dallas, Texas, April 16-18, p.81.

United States Environmental Protection Agency, Resistivity Methods, 2006: https://archive.epa.gov/esd/archive-geophysics/web/html/resistivity_methods.html (accessed March 2018).

United State Environmental Protection Agency, Hazardous Waste Cleanup: Former Ingersoll Rand in Phillipsburg, New Jersey, 2018. <https://www.epa.gov/hwcorrectiveactionsites/hazardous-waste-cleanup-former-ingersoll-rand-phillipsburg-new-jersey> (accessed September 2019).

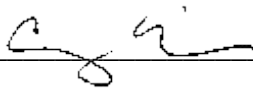
Van Schoor, M., 2002, Detection of Sinkholes Using 2D Electrical Resistivity Imaging: Journal of Applied Geophysics, v. 50, p. 393-399. doi: 10.1016/S0926-9851(02)00166-0.

WellCadd, 2019, WellCAD Software 5.3: <alt.lu/pdf/WellCADD.pdf> (accessed October 2019).

Wightman, W. E., Jalinoos, F., Sirles, P., and Hanna, K., 2003, Application of Geophysical Methods to Highway Related Problems., Federal Highway Administration, Central Federal Lands Highway Division, Lakewood, CO, Publication No. FHWA-IF-04-021, September 2003: <https://archive.epa.gov/esd/archive-geophysics/web/html/index-12.html>.

Williams, J., 1999, United States Geological Survey, Introduction to Borehole Geophysics: https://www.usgs.gov/centers/ny-water/science/borehole-geophysics?qt-science_center_objects=0#qt-science_center_objects (accessed October 2017).

I, Corey Thompson Miller, hereby submit this thesis to Emporia State University as partial fulfillment of the requirements for an advanced degree. I agree that the Library of the University may make it available to use in accordance with its regulations governing materials of this type. I further agree that quoting, photocopying, digitizing or other reproduction of this document is allowed for private study, scholarship (including teaching) and research purposes of a nonprofit nature. No copying which involves potential financial gain will be allowed without written permission of the author. I also agree to permit the Graduate School at Emporia State University to digitize and place this thesis in the ESU institutional repository, and ProQuest Dissertations and Thesis database and in ProQuest's Dissertation Abstracts International.



Signature of Author

Date

Title of Thesis

Signature of Graduate School Staff

Date Received